Title
A Reproducing Kernel Particle Hydrodynamic Formulation for Modeling Strong Shock Effects in Nonlinear Solids

Author
Roth, Michael Jason

Publication Date
2013

Peer reviewed|Thesis/dissertation

UNIVERSITY OF CALIFORNIA

Los Angeles

A Reproducing Kernel Particle Hydrodynamic Formulation for Modeling Strong Shock Effects in Nonlinear Solids

A dissertation submitted in partial satisfaction of the

requirements for the degree Doctor of Philosophy

in Civil Engineering

by

Michael Jason Roth

2014

ABSTRACT OF THE DISSERTATION

A Reproducing Kernel Particle Hydrodynamic Formulation for Modeling Strong Shock Effects in Nonlinear Solids

by

Michael Jason Roth

Doctor of Philosophy in Civil Engineering

University of California, Los Angeles, 2014

Professor Jiun-Shyan Chen, Chair

Many of today's challenging engineering and scientific problems involve the response of nonlinear solid materials to high-rate dynamic loading. Accompanying hydrodynamic effects are crucial, where the shock-driven pressure dominates material response. In this work a hydrodynamic meshfree formulation is developed under the Lagrangian reproducing kernel particle method (RKPM) framework. The volumetric stress divergence is enhanced to

capture the high-pressure shock response, and the deviatoric portion is retained to describe strength effects of the solid material. A shock modeling formulation for scalar conservation laws is first constructed. In the scalar formulation the reproducing kernel particle method is formulated to address two key shock modeling issues, that is, accurate representation of the essential shock physics and control of the numerical oscillations due to Gibbs phenomenon at the jump. This is achieved by forming a smoothed flux divergence under the meshfree stabilized conforming nodal integration (SCNI) framework, and then enriching the flux divergence with a Riemann solution. The Riemann-enriched flux divergence is embedded into a velocity corrector adaptively applied at the shock front. As a consequence the shock solution is locally corrected while the smooth solution away from the shock is unaffected. For shocks in solids, developments from the scalar formulation were extended to the Cauchy's equation of motion. Shock effects in solids are pressure dominated, so that the shock solution is enhanced through the volumetric stress divergence. The volumetric stress divergence correction is formulated using a Rankine-Hugoniot enriched Riemann solution that introduces the essential shock physics to the formulation. Oscillation control is introduced through the state and field variable approximations that utilize the Riemann problem initial conditions, and therefore non-physical numerical parameters and length scales required in the traditional artificial viscosity technique are avoided. Further, because the proposed method for oscillation control is linked to the essential physics, the two key issues for accurate shock modeling are addressed in a unified and consistent way. For the nonlinear solids formulation, several benchmark problems are solved and the numerical

results are verified by comparison to experimental data or analytical solutions. A range of shock conditions are studied to show the versatility of the proposed method for modeling conditions ranging from weak elastic-plastic shocks to strong shocks generated by hypervelocity impact.

The dissertation of Michael Jason Roth is approved.

Stanley Osher

Stanley Dong

Gaurav Sant

Jiun-Shyan Chen, Committee Chair

University of California, Los Angeles

2014

For Angie, Jonah and Savannah

TABLE OF CONTENTS

LIST OF FIGURES

LIST OF TABLES

ACKNOWLEDGEMENTS

I would like to first express my sincere thanks to my advisor, Professor J. S. Chen, for his patient guidance and teaching throughout this education process. It has been an honor to study under his direction; I am forever proud to have had the opportunity. I would also like to thank my committee members: Professor Stanley Osher, Professor Stanley Dong, Professor Gaurav Sant, Dr. Thomas Slawson and Dr. Kent Danielson, for their participation on my committee and their helpful ideas and suggestions for my research.

I would also like to express my sincere gratitude to the U.S. Army Corps of Engineers, Engineer Research and Development Center, and particularly James Davis, for their support of this endeavor. I would like to thank Dr. Jesse Sherburn as well for the countless conversations and time spent in discussion on my research ideas.

Lastly, I would like to thank my wife, Angie, and children, Jonah and Savannah, for sacrificing so much so that I could succeed in this endeavor. Their support and faith in me, from the beginning to the end, made this possible. Most importantly I thank God, from whom all strength comes.

VITA

1993-1998	B.S., Civil Engineering, Summa Cum Laude
	Mississippi State University, Starkville, MS
2003-2007	M.S., Civil Engineering
	Mississippi State University, Starkville, MS
1998-2002	Project Engineer
	Waggoner Engineering, Inc., Jackson, MS
2002-present	Research Structural Engineer
	U.S. Army Engineer Research & Development Center
	Vicksburg, MS
Select Awards	2013 USNCCM Student Travel Award
	2012 ERDC Award for Excellence in Operational Support
	2009 Army Research and Development Award
	2008 SAME – Toulmin Medal
	2008 Army R&D Achievement Award, Technical Excellence
	2005 Army R&D Achievement Award, Technical Excellence
Professional Registration	
	Licensed professional engineer, MS, 2002

Professional Societies

U.S. Association for Computational Mechanics; Member
Special Committee on Meshfree Methods (2009-present)

Society of American Military Engineers (2005-present)

Patents

3 U.S. patents for concrete armoring materials

Select Publications

Roth, M.J., Chen, J. S., Slawson, T., and Danielson, K. 2012. A reproducing kernel formulation for modeling shocks. *Proceedings of 10th World Congress on Computational Mechanics*, Sao Paulo, Brazil, July 9-13.

Roth, M.J., Chen, J. S., Slawson, T.R., Boone, R.N., Ren, X., Shi, S.W., Lee, C.H., and Guan, P.C. 2011. Multiscale RKPM formulation for modeling penetration of an ultra high-strength concrete material. *Proceedings of Third International Conference on Computational Methods in Structural Dynamics and Earthquake Engineering*, Corfu, Greece, May 26-28.

Guan, P.C., Chi, S.W., Chen, J. S., Slawson, T.R., and **Roth, M.J**., 2011. Semi-Lagrangian reproducing kernel particle method for fragment-impact problems, *Int. J. Impact Eng.*, **38**, 1033-1047.

X. Ren, Chen, J. S., Li, J., Slawson, T.R., and **Roth, M.J**., 2011. Micro-cracks informed damage model for brittle solids. *Int. J. Solids Struct.*, **48**, 1560-1571.

Roth, M.J., Eamon, C.D., Slawson, T.R., Tonyan, T.D., and Dubey, A., 2010. Ultra-high-strength, glass fiber-reinforced concrete: mechanical behavior and numerical modeling. *ACI Materials Journal*, **107**(2), 185-194.

CHAPTER 1 INTRODUCTION

1.1 Motivation

Material and structure response to impulsive dynamic loads is important in many commercial and defense applications. Examples include explosive cutting and welding [1, 2], vehicle and aircraft component design for impact and collision [3, 4], mining and earth cratering applications [5, 6], design and analysis of containment structures [7, 8], armor development [9, 10, 11], and the design and analysis of protective structures exposed to impact and blast [12, 13]. Large strain gradients, high strain rates, large deformation, and material fracture are commonly encountered, and are often accompanied by strong hydrodynamic effects. In many cases pressure-dominated material response leads to fluid-like behavior in the solid; shock wave formation is a particularly important aspect of this hydrodynamic behavior. Large velocity and/or pressure gradients cause transient discontinuities in pressure, material velocity, density and internal energy that propagate as shock waves through the material. Interface wave reflections according to the change in material impedance can lead to large tensile stresses and consequent dynamic tensile failure. Analytical methods are insufficient to model the complex conditions that are present in strong dynamic problems of practical interest. Empirical approaches are limited to experimental constraints and do not address the governing physics. Consequently, robust numerical methods that accurately represent the essential physics and are constructed in a

framework equipped to model the complex response phenomena of the solid continuum are required.

Lagrangian structured-mesh methods, like the finite element (FE) method, are generally well suited to model solid dynamics problems. Their construction in the material coordinate system provides a distinct advantage for the description of complex solid geometry, material interfaces, and contact surfaces. The key issues for FE application in fields like impact and blast are largely associated with mesh instability, sensitivity, and subjectivity in the presence of severe material deformation and weak or strong discontinuities. Techniques such as element erosion [14, 15] and extrinsic enrichment of the approximation functions [16, 17] have been developed to help alleviate these artificial mesh dependencies. However, issues such as phenomenological failure criteria, mass conservation in the presence of numerical erosion, contact surface erosion, and efficient means to model high-density crack growth remain. In contrast, Eulerian finite difference (FD) and finite volume (FV) methods are typically well-suited to model large deformation and material flow. However, the fixed grid characteristic of these methods generally limits their ability to sharply resolve complicated material interfaces, contact surfaces, and evolving free surfaces, which are common in high-rate solid dynamics problems. Regardless of the numerical framework, stability in the presence of shock-induced discontinuities is a critical issue. Field and state variable discontinuities give rise to oscillatory instabilities in the form of Gibbs phenomenon at the jump. Techniques such as artificial viscosity [18, 19], streamline upwinding [20, 21], and

adaptive stencil definitions [22, 23] are used as mechanisms to limit oscillation in these traditional numerical methods.

Meshfree methods are emerging as a new class of numerical methods that are well suited to model high-rate solid dynamics phenomena such as large deformation, material fragmentation, and evolving contact conditions. In the meshfree framework, the solution of the governing equation or equations is approximated using a non-conforming discretization, where discrete points or nodes interact through non-conforming kernels of compact support. Relaxation of the conforming constraint on the discretization yields strong reduction of mesh dependency in the solution, while a Lagrangian approximation maintains sharp resolution of material boundaries and interfaces. Flexibility in selection of the approximation continuity and locality afford further advantage for problems in the field of high-rate solid dynamics. With these benefits acknowledged, techniques to accurately model the hydrodynamic effects of shocks in solids have yet to be addressed in the meshfree framework. The artificial viscosity technique is most commonly used by traditional methods to aid in shock modeling. However, the approach relies on subjective length scales and numerical parameters, and lacks a rigorous tie to the fundamental shock physics. Therefore, new techniques are required for meshfree methods to ensure that the essential shock physics are correctly represented and the fine-scale shock front is accurately resolved without oscillatory instability at the jump. This need for an enhanced meshfree formulation that is adequately equipped to accurately model strong shock effects in solids provides the motivation for this research.

1.2 Objectives and Outline

The purpose of this research is to develop a multi-dimensional, hydrodynamic reproducing kernel particle method (RKPM) [24, 25] formulation to accurately model strong shock effects in nonlinear solid materials. The formulation will be constructed to ensure satisfaction of the essential shock physics and accurately resolve the shock front motion while avoiding the formation of oscillatory instabilities at the jump. The shock-capturing enrichment is introduced through the volumetric stress divergence while the deviatoric portion is retained to describe shear response; consequently, the formulation is considered to be a type of hydrocode [26]. Specific research objectives include:

1. Develop a technique to automatically detect and track shock waves in a multi-dimensional domain. With this automatic detection capability, local enrichments can be applied at the shock front to enforce the shock physics and provide oscillation control. To construct the detection algorithm, the intrinsic spectral decomposition property of the reproducing kernel approximation will be used to isolate high-frequency spectra at jump locations. Consistency and locality of the decomposed approximation is investigated to construct effective pass limits for the frequency filtering. The localized high-frequency spectrum from the decomposition is viewed as a high-pass solution error, so that automatic shock detection follows from analysis of the high-pass error density.

2. Develop an oscillation limiting RKPM formulation to model shock-forming scalar conservation laws. Development of the formulation for shock-forming scalar laws is used as a foundational development that will be extended to Cauchy's equation of motion for nonlinear solids. For the scalar law formulation, a Riemann-embedded flux divergence operator is constructed under the framework of stabilized conforming nodal integration [27, 28] to satisfy the second law of thermodynamics and ensure that the entropy-correct shock solution is obtained. The flux divergence operator is embedded into a flux-corrected velocity to adaptively limit oscillation at the shock front and control formation of Gibbs phenomenon. Several numerical examples are used to assess accuracy of the proposed formulation.

3. Develop a new RKPM hydrodynamic formulation to model shock effects in nonlinear solids. Core concepts developed in the scalar law formulation are extended to model shock effects in nonlinear solids. To construct the hydrodynamic formulation, the volumetric stress divergence is corrected to enforce the essential physics and provide oscillation control. The correction is formed using a Rankine-Hugoniot enriched Riemann solution that is constructed under the framework of stabilized conforming nodal integration; oscillation control is provided through the field and state variable approximations used for the Riemann problem initial conditions. Artificial viscosity is avoided as a consequence. A technique is also developed for update of the nodal pressures in accordance with a

Rankine-Hugoniot enriched volumetric strain. The enriched strain is also derived from the Riemann solution and therefore provides consistency between the corrected volumetric stress divergence and the updated nodal pressures during temporal integration.

4. Verify accuracy of proposed formulation for conditions ranging from strong shocks to elastic discontinuities. The RKPM hydrodynamic formulation developed in Objective 3 is applied to several benchmark shock propagation problems for verification of the formulation accuracy. Numerical results are compared to analytical solutions and experimental data to assess the accuracy. A broad range of shock conditions are considered, ranging from transient elastic discontinuities to strong shocks resulting from hypervelocity impact.

The outline of this dissertation is as follows. In Chapter 2 a review is provided of the background literature on meshfree methods and the primary techniques that have been used by traditional numerical methods for modeling shocks. Various meshfree techniques for improved discontinuity modeling are also reviewed. An overview of important concepts for shock phenomena in solids is provided in Chapter 3, where the Rankine-Hugoniot jump equations, the Hugoniot thermodynamic response curves, and the effects of impedance mismatch at material interfaces are reviewed. Some of the important numerical issues that arise in shock modeling are also reviewed, along with numerical approaches that have been used to address them. In Chapter 4 the development of a proposed RKPM formulation to

model shock-forming scalar conservation laws is presented. The formulation is corrected through a Riemann-enriched smoothed flux divergence that embeds the essential physics related to entropy production into the formulation. A flux-corrected velocity is also formulated that adaptively controls oscillation at the shock jump and is linked to the Riemann enrichment. The adaptivity is achieved through a shock detection algorithm that is also presented. Numerical examples are given to assess formulation accuracy. In Chapter 5 the concepts developed for the scalar law formulation are extended to the equation of motion for nonlinear solids. In this chapter the variational equation is operated on to isolate the pressure gradient and construct a shock modeling correction that follows a Rankine-Hugoniot shock solution to a Riemann problem. In this way the high-pressure shock physics for solids is enforced, and oscillation control is provided through approximation of the Riemann problem initial conditions. Several other key issues such as a methodology to compute consistent nodal pressures and algorithm implementation are also discussed. In Chapter 6 several benchmark problems are provided to assess accuracy of the hydrodynamic RKPM formulation. In these problems a broad range of shock conditions are modeled that include elastic discontinuities, weak elastic-plastic shocks, and strong shocks resulting from hypervelocity impact. Results from the proposed formulation are compared to experimental data and uncorrected results to show the improvements provided through this work. Conclusions and closing remarks are provided in Chapter 7, along with recommendations for future work.

CHAPTER 2 LITERATURE REVIEW

Computational shock modeling is a topic of strong research interest and has been widely investigated based on traditional finite difference and finite element methods. In comparison, much less research has been conducted in the field of meshfree shock modeling due to the relatively short history of development in this class of methods. The purpose of this chapter is to first discuss the seminal developments in the field of meshfree methods, leading to the introduction of RKPM in 1995. Key developments in the areas of FD and FE shock modeling are then reviewed, with emphasis on the source of numerical error in shock solutions and improvements that were developed to address these errors. Earlier work on RKPM-based shock modeling in the direction of adaptive meshfree refinement for enhanced accuracy in sharp gradient solutions is also reviewed.

2.1 Meshfree methods

The first generation of modern meshfree methods was smooth particle hydrodynamics (SPH), introduced by Gingold and Monaghan [29] in 1977. In SPH the numerical solution is obtained on a point-wise basis by transforming the governing equation with a kernel function that is defined on a compact smoothing domain. The method is fast and computationally efficient, but suffers from low order accuracy, lack of consistency, tension instability, and rank instability. This was not a significant issue in the early applications of SPH to large-

scale astrophysics problems, but creates significant issues for applications such as solid dynamics. SPH was followed by development of the moving least squares (MLS) approximation by Lancaster and Salkauskas [30] in 1981. The MLS approximation locally corrects the SPH kernel using a minimization of weighted residuals so that accuracy of the approximation is improved. An important result is correction of the kernel at the domain boundary, where the kernel weighting must be adjusted due to the lack of nodes or particles beyond the boundary. In 1992 Nayroles et. al [31] introduced the diffuse element method (DEM), where they first used the MLS approximation in the solution of partial differential equations. As an improvement of DEM, Belytschko et al. [32] introduced EFG in 1994. The major improvements of EFG included modification of the so-called DEM diffuse derivatives, introduction of Lagrange multipliers for the imposition of boundary conditions, and use of higher-order quadrature rules for integration of the weak form. EFG was followed by the introduction of RKPM by Liu et al. [24] and Chen et al. [25]. In RKPM the key issue of approximation consistency or reproducibility was addressed through the construction of the corrected reproducing kernel (RK). Using Taylor series expansion the RK correction was derived to enforce n^{th} order polynomial completeness in the RK approximation by solving for a set of correction coefficients. The result is the ability to exactly reproduce any complete polynomial basis that is used in the RK approximation construction. Chen and Wang [33] showed that the RK correction can also be formed without use of the Taylor series expansion, making it possible to impose reproducing conditions for any set of non-polynomial basis functions. The discrete form of the RK approximation and construction of the RK shape

functions is given in Chen et al. [25]. A key characteristic of the RK shape functions (and meshfree shape functions in general) is lack of kronecker delta properties, which is an important difference from the traditional FE method. To address the imposition of boundary conditions without the presence of kronecker delta properties, the transformation method [25], mixed transformation method [33], and boundary singular kernel method [33] were introduced. Domain integration is also an issue that has required special attention for meshfree methods. Gauss integration, although widely used in other methods, is not particularly attractive for numerical integration in the meshfree framework. The lack of a background mesh and the fact that the meshfree shape functions are generally rational functions lead to significant integration error when Gauss integration is used. As a method for improved numerical integration in the meshfree framework, Chen et al. [27, 28] introduced stabilized conforming nodal integration (SCNI). In SCNI nodal derivatives are transformed using a smoothed gradient operator that is constructed on a conforming integration cell structure. As a consequence direct nodal integration (DNI) can be used without the introduction of significant errors that typically accompany DNI. SCNI has been shown to be optimally convergent [27] and computationally efficient for numerical integration of the weak form. An alternative stabilized non-conforming nodal integration (SNNI) technique [34] was developed for problems involving material fragmentation and separation, where it is inefficient to reconstruct the conforming integration cell structure as fragmentation surfaces evolve. A semi-Lagrangian form of the RK approximation and new treatments for evolving contact conditions were presented by Guan et al. [35].

2.2 FD shock modeling

Finite difference methods are widely used to model shocks in fluids, and the numerical solution generally exhibits dissipation (smoothing) or dispersion (oscillation) errors depending on the formulation accuracy. Dissipation error is typically dominant in first-order accurate methods, where order of accuracy is expressed in terms of error resulting from a truncated Taylor series expansion [36]. Similarly, oscillation error generally coincides with second-order accurate (and higher) methods [36]. An example of a first-order accurate, dissipation-dominated FD method is the Lax method [36, 37], while the Lax-Wendroff method [36, 38] is an example of a second-order accurate, dispersion-dominated scheme. Tannehill, Anderson and Pletcher [36] showed through Taylor series expansion that when truncation error is $O(\Delta t, \Delta x)$, i.e., first order, the dominant error term is a function of grid spacing, Δx, and the second derivative of the solution, $u_{,xx}$. This is analogous to the introduction of a viscosity term into the governing equation and explains why first-order accurate schemes tend to exhibit smoothed shock fronts. Similar analysis showed that second-order truncation error produces dominant error as a function of Δx^2 and $u_{,xxx}$, which introduces wave dispersion and solution oscillation at the jump [36]. The presence of oscillation error in second-order and higher schemes is supported by Godunov's theorem, which states that monotonicity preserving (i.e., non-oscillatory) linear numerical schemes can be at most first-order accurate [39]. In terms of solution admissibility, Lax showed that physically permissible solutions to scalar conservation laws must satisfy a total variation

diminishing (TVD) condition [36, 37]. The TVD condition states that the integral of the solution gradient over a problem domain should not grow in time; or otherwise stated, a numerical method should not generate new solution extrema in time [36].

Given the tendency of higher-order FD schemes to exhibit oscillation error and violate the TVD condition, a widely-used technique for error minimization is the inclusion of slope or flux limiters. Slope and flux limiters are introduced to a numerical technique as limits on the change in the solution or solution gradient, respectively, so as to prevent the extrapolation of new solution extrema [36]. Limiters can be explicitly designed so that the TVD condition is enforced in the presence of shock-induced discontinuities [36]; they also tend to reduce solution accuracy at smooth local extrema. Examples of limiters include the van Leer limiter [40], the van Aldaba limiter [41], the minmod limiter [36], and the "Superbee" limiter [42]. These various limiter formulations provide different amounts of higher-order term suppression as a function of the magnitude of solution or flux differences [43].

As an advancement beyond limiter techniques, a class of uniformly high-order accurate, nonoscillatory (UNO) and essentially non-oscillatory (ENO) schemes were developed by Harten and Osher [44] and Harten et al. [45]. The objective of the UNO and ENO schemes was to achieve a uniformly high-order accurate solution to shock-forming conservation laws, while minimizing or eliminating solution oscillation at the jump. In other words, the UNO and ENO schemes were developed to achieve a non-oscillatory solution to shock problems without the loss of accuracy at smooth extrema that generally occurs with techniques such as slope or flux limiting. In development of the UNO scheme a relaxed TVD definition was

adopted [44], where the method was required to prevent an increase in the number of solution extrema but not necessarily their magnitude. Using this, Harten and Osher [44] presented a second-order accurate UNO scheme that guaranteed uniform second-order accuracy over the problem domain while achieving essentially non-oscillatory conditions at a shock. The second-order accurate UNO scheme was later extended to achieve an arbitrarily high order of solution accuracy [45], which was labeled the ENO scheme. To achieve the arbitrary order of accuracy, the TVD definition was further relaxed to allow for the presence of spurious oscillations in the solution, but with their magnitude limited to the order of the truncation error (i.e., $O(\Delta x^r)$ where r is the order of solution accuracy).

In the UNO and ENO schemes, the solution to an initial boundary value problem (IBVP) is formulated as an approximation to the cell-averaged solution of the problem [44, 45]. As such, the technique assumes that at each time, t_n, a set of cell-averaged solutions, $\bar{u} = \{\bar{u}_i\}_{i=1}^{ncells}$, exists over the problem domain ($ncells =$ number of computational cells). Using the cell-averages, a reconstructed solution is formed to the desired order of accuracy. The reconstructed solution is used to define a set of initial conditions for a "new" IBVP, which is integrated forward in time to t_{n+1}. The cell-averaged solution is then recomputed at time t_{n+1}, which provides a new approximation of the cell-averaged solution. By the virtue of cell averaging, the cell-averaged solution at t_{n+1} is non-oscillatory with respect to the solution of the so-called new IBVP. Harten and Osher [44] further showed that the new IBVP solution itself is non-oscillatory. Therefore, the critical component in achieving a non-oscillatory ENO solution is development of a non-oscillatory reconstruction of $\bar{u}$. The non-

oscillatory reconstruction is based on the development of a non-oscillatory interpolant for use in interpolating the cell-averaged solutions. To construct the non-oscillatory interpolant, an adaptive stencil selection algorithm is introduced. In Harten and Osher [44] the minmod function was utilized to form an interpolation stencil over the region of smoothest solution. In the vicinity of a shock, the minmod function forces the interpolant stencil to be winded away from the jump, so that interpolation across the discontinuity is avoided. This avoidance of cross-jump interpolation correspondingly avoids generation of Gibb's phenomenon oscillation. Due to the adaptive stencil selection algorithm, ENO is a non-linear solution method in that the solution interpolants evolve with the solution itself. Since Godunov's theorem is stated in terms of linear solution techniques, this partly explains how higher-order accurate, non-oscillatory solutions are achieved without violation of the theorem.

The ENO scheme was extended by Liu, Osher and Chan [46] so that the interpolants were adaptively defined from a convex combination of all possible interpolants covering a calculation cell. This was known as the weighted essentially non-oscillatory (WENO) scheme. The key idea of the WENO scheme is to form the nonlinear interpolant as a weighted combination of all possible interpolants, where interpolants that contribute to cross-jump interpolation are assigned a weight of zero [46]. An advantage of the WENO scheme over the standard ENO formulation is that through proper construction of the convex combination, not only is the non-oscillatory condition achieved, but a one-order increase in accuracy can also be obtained. This increase in order of accuracy is achieved by combining the weighted interpolants so that the leading term in the truncation error is cancelled, forcing

the error to be one-order higher. The ENO scheme was further developed by Shu and Osher [47, 48] and Osher and Shu [49] to enhance simplicity in implementation, particularly for application to problems in multiple dimensions. In Shu and Osher [48] and Osher and Shu [49], the ENO formulation was modified so that adaptive interpolants were applied to numerical fluxes rather than the cell-averaged solution. This avoided the requirement to reconstruct a point-wise solution from cell-averages, which simplified the solution of multi-dimensional problems [47]. A Runge-Kutta TVD temporal integration scheme was also introduced in lieu of the Lax-Wendroff-type integration, simplifying implementation [47].

2.3 FE shock modeling

Under the finite element framework, a major contribution towards accurate shock modeling was development of the upwind Petrov-Galerkin and streamline upwind/Petrov-Galerkin (SUPG) methods [50, 51, 52]. Christie et al. [53] provided one of the earliest investigations towards an upwind FE scheme, where they introduced a Petrov-Galerkin formulation using biased weight functions in conjunction with linear and quadratic, C^0 continuous basis functions. They showed that an oscillation free solution to a one dimensional shock problem could be obtained with the proper selection of biasing. Kelly et al. [54] discussed the correspondence between Petrov-Galerkin upwinding and the introduction of additive or balanced dissipation to the system. Kelly et al. [54] stated that the effects of Petrov-Galerkin upwinding were analogous to inclusion of an additional dissipation term in the governing equation. However, their approach was claimed to be more

efficient to implement in multiple dimensions. Brooks and Hughes [50] also presented the analogy between Petrov-Galerkin upwinding and additive dissipation, showing that the techniques were equivalent. Brooks and Hughes [50] further stated that a FE scheme using a central differenced approximation in space[1] is under-diffuse; therefore, the inclusion of additive dissipation was considered corrective in nature. In the context of solution accuracy, Hughes and Brooks [51] pointed out that a central difference FE method exhibits second-order accuracy, while upwinding reduces accuracy to first order. Notably, oscillation-free FE solutions by first-order upwind schemes and the generation of solution oscillation with higher-order schemes are in agreement with Godunov's theorem for monotone solutions.

Although the upwinding techniques reduced solution oscillation, a major shortcoming was found to be the introduction of excessive cross-wind diffusion for problems in multiple dimensions [50]. The SUPG formulation was introduced to correct this cross-wind diffusion effect [50, 51, 52]. The essential idea behind the SUPG formulation was that additive diffusion (introduced to the variational equation either by a modified test function or an additional diffusivity term) is introduced so that it is only active in the direction of the streamline, i.e., in the direction of flow. Introduction of streamline diffusion through a Petrov-Galerkin formulation was first studied for an advection dominated advection-diffusion problem [50]. A modified weight function, $\widetilde{w}$, was introduced to the variational equation, where the weight function, w, was enriched with an additional term, p, so that $\widetilde{w} = w + p$. The enrichment term, p, was a function of 1) a diffusion constant, τ,

[1] The standard Galerkin FE formulation using linear, C^0 continuous elements is a central difference method.

2) normalized velocity vector, and 3) the gradient of w. When w is piecewise, C^0 continuous, $\widetilde{w}$ is C^{-1} continuous. Accordingly, the enrichment, p, is only active over the element interiors [50]. Hughes and Tezduyar [55] extended the SUPG formulation to hyperbolic systems of equations and compressible flow problems. An alternative matrix form of the enrichment term, p (given as $\boldsymbol{P}$ in Hughes and Tezduyar [55]), was also presented. Here $\boldsymbol{P}$ was a function of 1) a diffusion constant, τ, 2) the flux gradient taken with respect to the solution, and 3) the weight function spatial gradient. Neither Brookes and Hughes [50] nor Hughes and Tezduyar [55] provided a definitive theoretical basis for definition of the diffusion constant, τ; selection was made to optimize the solution accuracy [50, 51]. Two definitions of τ based on temporal or spatial criteria were given in Hughes and Tezduyar [55].

Further enhancement of the SUPG formulation was developed by Hughes, Mallet and Mizukami [56]. Although the SUPG formulation was effective in mitigating the problems of solution oscillation and cross-wind diffusion, it was noted that solution jumps at thin transition layers were not always captured with sharp resolution [56]. To improve resolution at these sharp jumps, an additional "discontinuity capturing term" was introduced to the weight function enrichment [56]. The weight function retained a form similar to that originally proposed in Brookes and Hughes [50], but was modified so that $\widetilde{w} = w + p_1 + p_2$. The term p_1 retained the function of providing additive dissipation in the direction of the streamline, while the term p_2 acted only in the direction of the solution gradient to enhance resolution at strong gradients and shocks. A definition for p_2 was provided in similar form to

p_1 (or p in the original SUPG formulation); however, for the new discontinuity capturing term only the velocity component acting in the direction of the solution gradient was considered. This engenders a nonlinearity into the SUPG formulation, in that the weight function evolves with the solution gradient. Although this nonlinearity leads to additional computational expense, its inclusion results in improved shock capturing capability [56]. The two-term weight function enrichment has been further investigated, e.g., [57, 58], with focus on improved definition of the streamline diffusion, τ, and discontinuity capturing terms.

2.4 Artificial viscosity

Under nearly all computational frameworks, artificial viscosity has been used as a mechanism to improve shock modeling results. Artificial viscosity was first introduced by VonNeumann and Richtmyer [59] as a means to address the oscillatory error observed in the discontinuous solution of partial differential equations. The technique was intended to transform a perfect discontinuity into a thin continuous transition layer so that numerical oscillation would be minimized. To provide this transition layer, VonNeumann and Richtmyer [59] introduced an additional (artificial) pressure term, q, to the conservation equations, with the requirement that the magnitude of q be on the order of the true pressure at the shock but negligible elsewhere. Because the technique mimicked the dissipative effect of viscosity or heat loss, the technique came to be known as inclusion of artificial viscosity. VonNeumann and Richtmyer [59] further required that 1) the Rankine-Hugoniot jump

equations be satisfied across the shock, 2) thickness of the shock layer be on the order of the numerical cell size regardless of the shock strength, and 3) the artificial viscosity only be applied under compression states since shocks do not exist as rarefactions. With these constraints, an expression for artificial pressure was defined as a function of 1) specific volume, 2) square of the grid spacing, 3) square of the velocity gradient, and 4) a dimensionless viscosity coefficient that is on the order of unity[2]. Dependence on square of the velocity gradient ensured that the artificial pressure was active near shocks but negligible in smooth regions of the solution. The viscosity coefficient was used to introduce a length scale to the artificial pressure term and govern the width of the shock transition layer [60]. Inclusion of the viscosity coefficient (or length scale) introduced subjectivity to the approach, which remains an issue for the technique. VonNeumann and Richtmyer [59] and Richtmyer and Morton [61] also presented a stability analysis for a set of second-order difference equations that included the artificial viscosity term. Analyses showed that the inclusion of artificial viscosity reduced the critical time step to approximately $1/3$ of the typical Courant, Friedrichs, Lewy (CFL) stability condition.

The technique of VonNeumann and Richtmyer [59] essentially consisted of adding a quadratic pressure term into the conservation equations that was activated only in regions of strong velocity gradient. Landshoff [62] suggested the inclusion of an additional linear term to the artificial pressure definition. Landshoff [62] showed that for a given discretization, the quadratic term damped the initial overshoot at a shock jump but did not effectively damp

[2] Landshoff [62]and Wilkins [60] later indicated that a better value of the viscosity coefficient is ~2

residual oscillations behind the shock. On the other hand, the linear term damped the residual oscillations but did not strongly affect the initial overshoot. Therefore, Landshoff [62] proposed a combination of the linear and quadratic terms in order to combine the advantages of each. A similar two-term form was proposed by Noh [63, 64]. Wilkins [60] extended the two-term artificial pressure formulation to multiple dimensions under a FE framework, where the velocity gradient term was replaced by volumetric strain rate. To address the characteristic length in multiple dimensions, Wilkins [60] stated that the square root of mesh area or cube root of mesh volume (in two and three dimensions, respectively) was commonly used. However, Wilkins [60] noted that these characteristic length definitions may lead to error in elements that were largely distorted or exhibited large aspect ratios. To address this, Wilkins [60] introduced an alternative characteristic length defined in the direction of particle acceleration. According to Hallquist [65], most modern codes used for hydrodynamic calculations continue to use a two-term artificial viscosity formulation similar to that of Landshoff [62] and Wilkins [60]. Characteristic lengths are typically defined using the simpler definitions of area square root or volumetric cube root instead of Wilkins' acceleration-based approach, and volumetric strain rate is used in lieu of velocity gradient [65].

2.5 Meshfree adaptive refinement and discontinuity modeling

Under the framework of RKPM and other meshfree methods, adaptive *h*-refinement techniques have been developed to improve solution accuracy with respect to the

discretization error. Examples where adaptive *h*-refinement has been applied include problems with sharp geometric changes that induce stress concentrations [66, 67, 68, 69], problems involving point loads [66], calculation of crack tip stresses [70, 71], shear band formation [72], impact/penetration problems [73], and material extrusion [74]. The purpose of applying adaptive refinement in these types of problems is to reduce the discretization error in regions where the dependent variable is sharply changing. This same approach can be used to improve accuracy in the RKPM solution of the fine-scale shock structure, by adaptively refining at the shock and then coarsening in the smooth region behind the jump. The reason that adaptive refinement is particularly attractive for meshfree methods is that due to the reduced mesh dependency, nodes can be inserted and removed with relative ease [67, 75]. This is not the case for methods that utilize conforming meshes such as FE.

Two fundamental requirements exist for adaptive refinement techniques. First, an indicator is required to automatically determine what portion of the domain requires discretization refinement (or coarsening in the case of the smooth region behind a shock). In multi-level (i.e., iterative) adaptive refinement procedures, the indicator also determines at what point refinement is no longer required. The indicator is generally provided in the form of global and local error estimates, defined as the difference between the approximate solution and a reference solution. As long as the error measure is appropriately formulated to measure discretization error (instead of integration error, for instance), regions of high local error indicate where additional refinement is required. Because exact solutions do not exist for most problems of practical interest, the reference solution is commonly in the form of a

so-called recovered solution (error estimates in this form are typically referred to as recovery-based error estimates). Recovery-based error estimators form the recovered solution *a posteriori* using the numerical approximation, and were first introduced by Zienkiewicz and Zhu[3] [76]. The unique multiscale resolution feature intrinsic to RKPM provides an alternate method to perform error or strong gradient detection [66, 68]. In the multiscale resolution approach, the RKPM approximate solution is decomposed into low and high-scale components. The high-scale component serves as an indicator of solution error at strong gradients [68].

The second requirement of an adaptive refinement algorithm is a technique for nodal insertion. The addition of nodes in meshfree methods is relatively simple, and techniques such as cell splitting (based on a background integration mesh) [66, 71, 72], Delaunay triangulation [70], and Voronoi cell tessellation [67, 68] have been used. Other key issues that must be addressed in an adaptive refinement formulation are appropriate modification of integration points for numerical integration, support size adjustment, avoidance of sharp changes in nodal spacing and support size (to avoid artificial wave reflections), and field/state variable interpolation for transient analysis.

A variety of meshfree adaptive refinement approaches have been reported in the literature, most of which focus on the solution of elasto-static problems. Haussler-Combe and Korn [71] applied an adaptive refinement technique to the EFG method, where discretization error was estimated using the strain gradient. Using Taylor series expansion

[3] Typically referred to as the Z-Z error estimation

and the EFG consistency conditions, Haussler-Combe and Korn [71] showed that the solution error could be related to the gradient in strain and correspondingly to the H_2 error norm. The error norm was locally computed over integration cell domains, where Gauss integration on a background mesh was used for numerical integration. This was used as an *a posteriori* error estimator that provided an indicator for regions to be adaptively refined. A cell division strategy was employed for node insertion, where cells with excessive local error were subdivided so that nodes were inserted at new subcell vertices.

Liu and Tu [70], presented a different refinement method formulated around a background mesh. The MLS approximation [30] was used, and numerical integration was performed over a triangular background mesh with nodes located at the triangle vertices. Liu and Tu [70] used an *a posteriori* error indicator formulated from local strain energy calculated over each triangular integration cell. The approximate strain energy solution was computed directly from the approximated stress/strain fields. The reference solution was computed using the same stress/strain fields; however, a different number of Gauss points were used[4]. The authors acknowledged that this technique is actually an evaluation of the integration error, not a direct measure of discretization error. However, numerical experiments showed the method to be effective. The claimed advantage of this approach is that it does not require the calculation of a second stress field as other recovery methods do, which reduces computational cost. For discretization refinement, nodes were added either at the center of the triangular cells or at the midpoint of facets. The background mesh was

[4] Liu and Tu recommend that the reference solution be computed with a lower number of Gauss points (as compared to the approximate solution) for computational efficiency.

locally re-triangulated using the Delaunay triangulation algorithm, and support size was adjusted in the refinement regions to complete the adaptive refinement step.

Lu and Chen [67] developed an adaptive refinement technique within the RKPM framework. Numerical integration of the variational equation was performed using SCNI [27, 28] over a background Voronoi cell tessellation of the domain. The *a posteriori* stress recovery error estimator of Chung and Belytschko [77] was used to provide a measure of the relative energy error and the nodal energy error density. Lu and Chen [67] pointed out that for node insertion in RKPM, re-evaluation of shape function weights are only required at points, $\boldsymbol{x}$, contained within the new nodes' supports. Further, the re-evaluation is easily performed by re-calculating the moment matrix, $\boldsymbol{M}(\boldsymbol{x})$, at those locations. Node insertion was accomplished using the Voronoi cell topology, where nodes were inserted at cell vertices in locally refined regions [67]. The Voronoi cell tessellation was reconstructed in these areas to define the integration zones, and support size adjustment was performed.

Using wavelet analysis and Fourier transformation Liu et al. [78, 79, 80] and Li and Liu [81] described the multiresolution feature of RKPM, where the kernel function engendered the RK approximation with a frequency band decomposition property. The RK approximation was shown to behave as a low-pass filter, where the filter limits were controlled by the kernel function dilation. Increases in kernel size corresponded with reductions in the filter pass limit. Using a family of kernels (differentiated by their size) a multi-band frequency decomposition of the total solution was obtained, where each band corresponded to a wavelet. The high-scale wavelets were used as error indicators for

adaptive refinement in many applications including image analysis [79, 80], steady state advection-diffusion (with strong gradients) [78, 82], flow field jumps over an aerofoil [78, 79, 80, 82], and large deformation solid mechanics [79, 80]. You and Chen et al. [68] further investigated adaptive refinement using the multiresolution feature of RKPM. In their work the convolution of two kernels provided a filter of the RK approximation itself. The approximation was defined by a so-called approximation kernel and the filtered approximation was defined by a so-called filter kernel. The basis order and kernel dilation of the filter kernel were shown to control the filter limits. Using the filter kernel concept, You and Chen et al. [68] investigated the solution to a differential equation with strong gradient using a two-scale decomposition. The high-scale component of the filtered approximation was used to identify regions requiring further *h*-refinement. You and Chen et al. [68] utilized SCNI for the weak form integration, and therefore followed the adaptive node insertion procedure of Lu and Chen [67] (based on Voronoi cell tessellation). Jun and Im [72] and Lee et al. [66] also investigated multiresolution-based adaptive refinement, where two-scale decomposition was used for error indication. Lee et al. [66] and Jun and Im [72] used Gauss quadrature to integrate the weak form. Therefore, adaptive node insertion was performed using a cell division (or cell splitting) strategy based on the regularly structured Gaussian integration zones. Jun and Im [72] used the procedure to study adiabatic shear band formation while stress concentration problems were studied by Lee et al [66].

Lee and Shuai [83, 84] proposed another technique for adaptive refinement within an RKPM framework. They presented an *a posteriori* error indicator using so-called extraction

functions that provided an extracted (or recovered) stress field with a convergence rate higher than the RKPM approximation[5] [83]. The essential idea behind this technique is that a stress field at any point can be expressed as the sum of two operators, $\boldsymbol{\Psi}$ and $\boldsymbol{\Phi}$, that are functions of displacement-induced stress and body forces, respectively. If the stress field input to the extraction operator $\boldsymbol{\Psi}$ is the RKPM-computed stress, then the extracted stress is essentially an *a posteriori* recovered stress field. Lee and Shuai [83, 84] defined $\boldsymbol{\Psi}$ and $\boldsymbol{\Phi}$ as boundary and domain integral operators, respectively, which were evaluated over simple circular regions centered on the nodes. The recovered and RKPM stresses were then used in the Z-Z estimator to determine an energy error estimate. The energy error norm was used to drive automatic nodal insertion and support size adjustment [84]. The partition of unity property of the RKPM approximation was used to relate global and local energy error, and the *a priori* estimate of error in the RKPM solution (namely $\|e\|_{L_2} = Ch^{\min(p,\lambda)}$ where p is the basis order and λ is related to solution roughness) was used to derive an expression for modified nodal spacing [84]. Automatic support size adjustment was performed using a background grid and a multi-step procedure was used to ensure all points in the problem domain were adequately covered by nodal supports.

Beyond the more conventional adaptive refinement methods previously described, other techniques for improvement of strong gradient solutions have been proposed. For example, Ma et al. [85] proposed a moving point technique where the number of nodes within a

[5] Since convergence rate of the extracted solution was higher than the approximation, it provided an acceptable reference solution.

meshless domain remained constant, but nodal coordinates were automatically adjusted to provide greater refinement at strong gradients. Their intent was to improve solution accuracy at the jump without increasing computational cost in terms of nodal degrees of freedom. A so-called weighted reference radius was used to adjust the nodal coordinates [85]. The reference radius essentially defined a domain 1) centered on a parent node, and 2) which contained a set of satellite (or adjacent) nodes. The weighted reference radius was defined as a product of the reference radius and a weight function, where the weight function was inversely proportional to the solution gradient. As the solution gradient increased the weighted reference radius decreased. Assuming all satellite nodes remained within the reference radius of the parent, the technique naturally caused nodal densification in large gradient regions. After adjustment of all nodes in the domain, Ma et al. [85] applied a smoothing technique to avoid ill-conditioning in their system of linear equations. Another approach was investigated by Chen and Hu [73], where interface enrichment functions were used to capture transient interface discontinuities in microstructure grain evolution. For the evolution of grain structure in polycrystalline materials, the approximation of material velocity requires a discontinuity in the velocity derivative normal to the grain boundary. To capture this discontinuity, Chen and Hu [73] introduced a set of enrichment functions along the grain boundary interface that were used to enrich the RK approximation of velocity at these locations. The interface enrichment functions were formulated to be continuous across the grain boundary but discontinuous in their first derivative across the interface.

CHAPTER 3 BACKGROUND, SHOCK PHENOMENA AND NUMERICAL ISSUES FOR SHOCK MODELING

A strong shock is defined as a transient discontinuity with velocity greater than the elastic wave speed of the material [86]. In solid materials the strong shock is formed by creating a pressure or velocity gradient that is sufficient to accelerate the plastic wave to a speed greater than the material's elastic wave speed so that a shock front is formed. In the case of plastic waves that are slower than the elastic wave speed a "two-step" shock is formed, where there is an initial discontinuity traveling at the elastic wave speed that is followed by a slower plastic discontinuity traveling at the plastic wave speed. Because the plastic wave speed is slower than the elastic these two waves will tend to separate in time. These two-step shocks are referred to as weak or elastic-plastic shocks. Finally, it is also possible to create a transient discontinuity where the pressure jump remains in the material's elastic range so that the wave propagates at the elastic wave speed. This is not a true shock wave; however, it does create the numerical problem of oscillation at the jump, just as with strong shocks. In this study these elastic discontinuities are referred to as elastic shocks. To effectively model the response of solid materials to strong dynamic events, strong shocks, weak shocks, and elastic shocks must be addressed.

In the general case, shock wave propagation is characterized by a continuous displacement field, with discontinuities in specific volume, specific internal energy, particle velocity, and stress at the front. When tensile failure occurs, discontinuities in the displacement field are also introduced. Due to the presence of these discontinuities, the basic conservation laws of mass, momentum and energy must be supplemented to define constraint conditions at the shock front. These constraints are provided in the form of additional mathematical expressions defining the state and field variable discontinuities (or jump conditions) and are referred to as the Rankine-Hugoniot jump equations [86, 87]. In addition to the jump equations, a description of the material state behind the shock is required. For solid materials under normal loading, constitutive laws that relate stress and strain and define failure in terms of the material's shear strength are typically sufficient. However, extremely high pressures are commonly present with shocks (35 GPa (5,076 ksi) and greater [88, 89]) so that material behavior is pressure governed, similar to fluids. Therefore, an equation of state describing the relationship between pressure, volume, and specific internal energy is also required. Alternatively, a Hugoniot thermodynamic response curve can be used to describe the pressure-volume relationship [86, 87].

The purpose of this chapter is to first review key aspects of the analytical description of a propagating shock. The Rankine-Hugoniot jump equations are presented, which mathematically define the jump constraints at the shock front. The so-called Rayleigh line equations are also presented, which are derived from the jump equations. To define the shock-induced material state, the Hugoniot thermodynamic response curves are discussed,

and equations describing three common forms are given. The concept of impedance mismatch and generation of interface wave reflections is also reviewed. Some of the key numerical issues related shock modeling are also reviewed, which include the numerical source of dissipation and dispersion errors, monotonicity, and numerical techniques that have been proposed to control oscillation error at the shock.

3.1 Rankine-Hugoniot jump equations

The Rankine-Hugoniot jump equations are most commonly derived and expressed in terms of the uniaxial propagation of a planar shock wave [86]. Consider a plane wave traveling in the positive x-direction through a one dimensional domain, as shown in Figure 1. Pressure, p, particle velocity, $\dot{x}$, specific volume, v, and specific internal energy, ε, are discontinuous across the front. Velocity of the shock front is denoted as u_s. Downstream conditions, or conditions ahead of the front, are denoted as $(\cdot)^-$. Upstream conditions, or conditions behind the front, are denoted as $(\cdot)^+$. Assuming downstream conditions are known from the initial state, five unknowns remain; namely u_s, p^+, $\dot{x}^+$, ε^+, and v^+. The jump equations provide three equations to be applied to these five unknowns, and one of the unknown field variables is assumed to be defined by the boundary condition that is driving the shock [87]. This leaves one independent unknown to be determined by an equation describing the high-pressure material response, such as an equation of state or Hugoniot thermodynamic response curve.

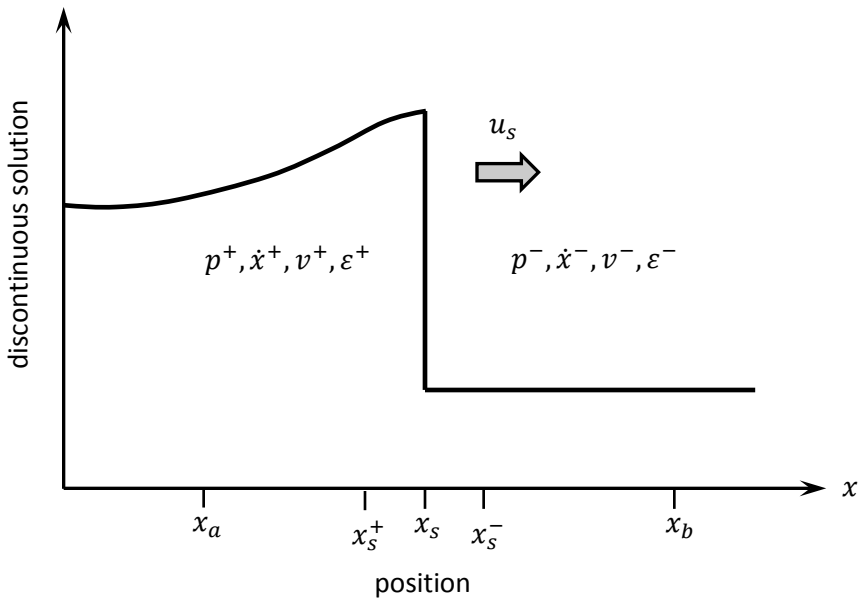

Figure 1. One dimensional planar shock wave (discontinuities in pressure, particle velocity, specific volume and specific internal energy)

3.1.1 Jump equation in mass conservation

Derivation of the first jump equation stems from the global form of the law of mass conservation,

$$\frac{d}{dt}\int_{\Omega_x} \rho \, d\Omega = 0 \qquad \text{eq. 1}$$

where ρ is mass density ($1/v$) and Ω_x is the problem domain. With reference to Figure 1 and taking Ω_x to be an arbitrary one dimensional domain in x, $x_a \leq x \leq x_b$, eq. 1 can be written as

$$\frac{d}{dt}\int_{x_a(t)}^{x_{b(t)}} \rho(x,t)dx = 0 \qquad \text{eq. 2}$$

where the time dependence of $x_a(t)$ and $x_b(t)$ imply use of the Eulerian form. Dividing the problem domain into smooth regions ahead and behind the shock and a region which contains the shock discontinuity, eq. 2 can be rewritten as

$$\frac{d}{dt}\left[\int_{x_a(t)}^{x_s^+(t)} \rho(x,t)dx + \int_{x_s^+(t)}^{x_s^-(t)} \rho(x,t)dx + \int_{x_s^-(t)}^{x_b(t)} \rho(x,t)dx\right] = 0 \qquad \text{eq. 3}$$

where the limits of the second integral, x_s^+ to x_s^- , represent a small region containing the shock. Considering the condition of an infinitesimally small shock transition region where $x_s^+(t) \to x_s^-(t)$, the second integral in eq. 3 goes to zero. Applying the Leibniz rule for differentiation under an integral, eq. 3 is transformed as

$$\rho(x_s^+(t),t)\frac{dx_s^+(t)}{dt} - \rho(x_a(t),t)\frac{dx_a(t)}{dt} + \int_{x_a(t)}^{x_s^+(t)} \frac{\partial}{\partial t}\rho(x,t)\,dx + \rho(x_b(t),t)\frac{dx_b(t)}{dt} - \rho(x_s^-(t),t)\frac{dx_s^-(t)}{dt} + \int_{x_s^-(t)}^{x_b(t)} \frac{\partial}{\partial t}\rho(x,t)\,dx = 0 \qquad \text{eq. 4}$$

In eq. 4, consider

$$\frac{dx_s^+(t)}{dt} = \frac{dx_s^-(t)}{dt} = u_s \qquad \text{eq. 5}$$

$$\frac{dx_a(t)}{dt} = \dot{x}_a\,, \qquad \frac{dx_b(t)}{dt} = \dot{x}_b \qquad \text{eq. 6}$$

where u_s is the Eulerian shock velocity and $\dot{x}_a$ and $\dot{x}_b$ are particle velocities at points upstream and downstream of the shock front, respectively. Utilizing eq. 5 and eq. 6 into eq. 4 the following is obtained

$$\rho(x_s^+(t),t)u_s - \rho(x_a(t),t)\dot{x}_a + \int_{x_a(t)}^{x_s^+(t)} \frac{\partial}{\partial t}\rho(x,t)\,dx + \rho(x_b(t),t)\dot{x}_b - \rho(x_s^-(t),t)u_s + \int_{x_s^-(t)}^{x_b(t)} \frac{\partial}{\partial t}\rho(x,t)\,dx = 0 \quad \text{eq. 7}$$

which can be rewritten as

$$\int_{x_a(t)}^{x_s^+(t)} \frac{\partial}{\partial t}\rho(x,t)\,dx + \int_{x_s^-(t)}^{x_b(t)} \frac{\partial}{\partial t}\rho(x,t)\,dx = \rho(x_a(t),t)\dot{x}_a - \rho(x_b(t),t)\dot{x}_b - u_s[\rho(x_s^+(t),t) - \rho(x_s^-(t),t)] \quad \text{eq. 8}$$

From the local form of the conservation of mass, a relationship between the time rate of change of density and the momentum gradient is found to be [86]

$$\frac{\partial}{\partial t}\rho(x,t) = -\frac{\partial}{\partial x}(\rho(x,t)\dot{x}) \quad \text{eq. 9}$$

Substituting eq. 9 into eq. 8 gives

$$\int_{x_a(t)}^{x_s^+(t)} \frac{\partial}{\partial x}(\rho(x,t)\dot{x})\,dx + \int_{x_s^-(t)}^{x_b(t)} \frac{\partial}{\partial x}(\rho(x,t)\dot{x})\,dx = -\rho(x_a(t),t)\dot{x}_a + \rho(x_b(t),t)\dot{x}_b + u_s[\rho(x_s^+(t),t) - \rho(x_s^-(t),t)] \quad \text{eq. 10}$$

Finally, evaluating the integrals of eq. 10 and simplifying gives

$$\left[(\rho\dot{x})|_{x_s^+} - (\rho\dot{x})|_{x_s^-}\right] = u_s\left[\rho|_{x_s^+} - \rho|_{x_s^-}\right] \quad or \quad [\![\rho\dot{x}]\!] = u_s[\![\rho]\!] \quad \text{eq. 11}$$

$[\![\cdot]\!]$ denotes a difference operation taken across the shock front. This is the Rankine-Hugoniot jump equation derived from the law of conservation of mass and written in an Eulerian framework [86]. As seen, the equation relates the jump in momentum across the shock front to the jump in material density.

3.1.2 Jump equations in linear momentum and energy conservation

The remaining two jump equations are derived from the laws of balance of linear momentum and energy, respectively

$$\frac{d}{dt}\int_{\Omega_x} \rho\dot{x}\, d\Omega = \oint_{\Gamma_x} t\, d\Gamma + \int_{\Omega_x} \rho b\, d\Omega \qquad \text{eq. 12}$$

$$\frac{d}{dt}\int_{\Omega_x} \rho(\varepsilon + \frac{1}{2}\dot{x}^2)\, d\Omega = \oint_{\Gamma_x} (t\dot{x} - qn)\, d\Gamma + \int_{\Omega_x} (\rho b\dot{x} + \rho h h) d\Omega \qquad \text{eq. 13}$$

where t is surface traction, b is body force, q is heat flux, and h is the rate of body heat transfer per unit mass. Reconsidering the uniaxial plane-wave problem in Figure 1, derivation of the jump equations from eq. 12 and eq. 13 follows a similar process as given in Section 3.1.1, and lead to [86]

$$[\![\rho\dot{x}]\!]u_s = [\![-p + \rho\dot{x}^2]\!] \qquad \text{eq. 14}$$

$$\left[\!\left[\rho(\varepsilon + \frac{1}{2}\dot{x}^2)\right]\!\right] u_s = \left[\!\left[\rho\left(\varepsilon + \frac{1}{2}\dot{x}^2\right)\dot{x} - p\dot{x}\right]\!\right] \qquad \text{eq. 15}$$

The jump eq. 11, eq. 14 and eq. 15 are written in scalar form following their typical derivation; they can be extended to multi-dimensional form following vector notation, e.g., [86].

3.1.3 Jump equations in Lagrangian form

In the preceding section the plane-wave propagation problem was derived in the Eulerian form. However, the Lagrangian form may also be necessary. For example, data from shock response experiments is often gathered in a Lagrangian setting (measurement devices move with the material) and therefore require expression of the jump equations in Lagrangian form.

The jump eq. 11, eq. 14 and eq. 15 can be translated to a Lagrangian description utilizing the relationship between shock front velocity expressed in the Eulerian and Lagrangian forms, i.e., u_s and U_s, respectively [86]. Consider a shock wave propagating in the reference configuration from point X at time t to $X' = X + \Delta X$ over a time increment Δt. The wave propagates from point x to x' in the spatial configuration over the same period of time. Let the coordinate of the point x' at time $t+\Delta t$ be defined as

$$x' = x + \Delta x + \dot{x}^{-}\Delta t \qquad \text{eq. 16}$$

where x' is defined by 1) location of the wave, x, at time t 2) an incremental distance in the spatial configuration, Δx, which can be related to an incremental distance in the reference configuration, ΔX, and 3) a displacement due to the downstream particle velocity, $\dot{x}^{-}$, over

the time increment Δt. Under the assumption of uniaxial deformation, mapping between Δx and ΔX can be expressed as [86]

$$\Delta x = J\Delta X = \frac{\rho^R}{\rho^-}\Delta X \qquad \text{eq. 17}$$

where J is the Jacobian, ρ^R is density in the reference configuration, and ρ^- is material density in the spatial configuration ahead of the shock. Using eq. 16, shock velocity in the spatial configuration can be expressed as

$$u_s = \frac{x' - x}{\Delta t} = \frac{\Delta x + \dot{x}^-\Delta t}{\Delta t} = \frac{\Delta x}{\Delta t} + \dot{x}^- \qquad \text{eq. 18}$$

Using eq. 17 into eq. 18 gives the relationship between shock velocities as

$$u_s = \frac{\rho^R}{\rho^-}\frac{\Delta X}{\Delta t} + \dot{x}^- = \frac{\rho^R}{\rho^-}U_s + \dot{x}^- \qquad \text{eq. 19}$$

Substituting eq. 19 into eq. 11, eq. 14 and eq. 15 gives the Lagrangian expressions of the Rankine-Hugoniot jump equations [86]

$$\rho^R U_s \left[\!\left[-\frac{1}{\rho}\right]\!\right] = [\![\dot{x}]\!] \qquad \text{eq. 20}$$

$$\rho^R U_s [\![\dot{x}]\!] = [\![-p]\!] \qquad \text{eq. 21}$$

$$\rho^R U_s \left[\!\left[\varepsilon + \frac{1}{2}\dot{x}^2\right]\!\right] = [\![-p\dot{x}]\!] \qquad \text{eq. 22}$$

3.1.4 Rayleigh line equations

The so-called Rayleigh line equations are commonly used in conjunction with Hugoniot thermodynamic response curves[6] written in the pressure-volume (p-v) and pressure-particle velocity (p-$\dot{x}$) planes. These equations are used to relate the shock front velocity to the state and field variable discontinuities at the jump. The Rayleigh line equations are derived directly from the Rankine-Hugoniot jump eq. 20, eq. 21 and eq. 22, as follows. The first equation is a simple rearrangement of eq. 21 and is expressed as

$$U_s = \frac{1}{\rho^R}\frac{[\![-p]\!]}{[\![\dot{x}]\!]} \qquad \text{eq. 23}$$

where the shock front velocity is directly related to the slope of the line defining the jump from the state $(p^-, \dot{x}^-)$ to $(p^+, \dot{x}^+)$ in the p-$\dot{x}$ Hugoniot plane. The second equation is obtained by solving for $[\![\dot{x}]\!]$ in eq. 21 and substituting into eq. 20, to give

$$U_s = \frac{1}{\rho^R}\left(\frac{[\![-p]\!]}{[\![-v]\!]}\right)^{1/2} \qquad \text{eq. 24}$$

where the shock front velocity is related to the slope of the line defining the jump from the state (p^-, v^-) to (p^+, v^+) in the p-v Hugoniot plane.

3.2 Equation of state and Hugoniot thermodynamic response curves

The Rankine-Hugoniot jump equations provide three equations to be applied to the five unknown variables at the shock front. Assuming that one of the five variables is known as

[6] Hugoniot response curves and their use discussed in Section 3.2

the driving stimulus for the shock, then one additional expression is required to fully resolve the jump conditions at the front [87]. The fourth equation is provided by introducing a material-specific description of the material state behind the front. This relationship is can be obtained from an equation of state (EOS) or a Hugoniot thermodynamic response curve.

The EOS describes the relationship between pressure, volume, and internal energy based on the properties of a specific material. Equations of state are most commonly used to describe the state variable relationships of inviscid fluids, i.e., materials that can sustain large pressures but possess no shear strength. Although solid materials do not behave in this manner under typical static or dynamic loads, use of an EOS to describe a solid material's response to shock is appropriate due to the presence of extremely high pressures relative to the material shear strength. An example of an EOS commonly used for isotropic, solid continua is the Mie-Grüeneisen equation of state. In its complete form, the Mie-Grüeneisen EOS is given as [86]

$$p(v,\eta) = p^{(\eta)}(v) + \theta_R \frac{\gamma(v)}{v} \chi(v) \int_{\eta_R}^{\eta} \omega(\eta') d\eta' \qquad \text{eq. 25}$$

where η is specific entropy, $p^{(\eta)}$ is pressure at constant entropy, θ_R is a reference temperature, $\gamma(v)$ is the so-called Grüeneisen coefficient, and $\chi(v)$ and $\omega(\eta)$ are given as

$$\chi(v) = exp\left[-\int_{v_R}^{v} \frac{\gamma(v')}{v'} dv'\right] \qquad \text{eq. 26}$$

$$\omega(\eta) = exp\left[-\int_{\eta_R}^{\eta} \frac{1}{C^v(\eta')} d\eta'\right] \qquad \text{eq. 27}$$

where v_R is a reference specific volume, η_R is a reference specific entropy, and C^v is specific heat at constant volume. A form of the Mie-Grüeneisen EOS more commonly used in numerical methods is [90]

$$p(v) = p^{(H)}(v) + \frac{\gamma(v)}{v}\left[\varepsilon(v) - \varepsilon^{(H)}(v)\right] \qquad \text{eq. 28}$$

where $p^{(H)}(v)$ and $\varepsilon^{(H)}(v)$ are the pressure-volume and internal energy-volume relationships defined by appropriate Hugoniot response curves. The important point made from eq. 28 is that in practice, introduction of Hugoniot curves to a theoretical equation of state provides a simpler, more computationally efficient form for numerical implementation. Further, due to the semi-empirical basis provided by the Hugoniot data (obtained experimentally), physical characteristics of the specific material considered are directly embedded into the EOS relationship. For brittle materials such as concrete, it is found that use of the Hugoniot response curves to describe state variable relationships is often even further exploited. In practice, Hugoniot relationships, such as the pressure-volume relationship, may often be used completely in place of a theoretical equation of state to define the material's high-pressure response [91, 92, 93].

The Hugoniot relationships are expressed in terms of the transition of two state variables (i.e., pressure and specific volume, pressure and particle velocity, etc.) across a shock, and are most often based on the so-called quiescent initial state[7] [86]. In essence, the Hugoniot curves can be thought of as a plane taken from a three dimensional space defined by an

[7] Quiescent initial state implies that material ahead of the shock is at rest and is under simple atmospheric pressure, i.e., in an un-shocked state.

equation of state [94]. For example, consider an equation of state relationship expressed in terms of pressure, internal energy and density, shown schematically in Figure 2a. Taking a plane from the space and expressing the EOS solution along that plane solely in terms of two variables, pressure and density, a two dimensional curve is obtained as shown in Figure 2b. This curve defines all possible pressure and density states that can be achieved by "shocking-up" from an initial state that lies on the same curve. In other words, assuming that the initial material state ahead of a shock front is known, say (p^-, ρ^-) in Figure 2b, then the pressure-density Hugoniot "centered" on that initial state defines all possible end states that can be achieved behind the front, i.e. (p^+, ρ^+). With reference to section 3.1.4, the line connecting the state jump in the pressure-density or pressure-particle velocity Hugoniot is the Rayleigh line. From eq. 23 and eq. 24 it is seen that when used in conjunction with the reference material density, the Rayleigh line can be used to determine the shock front velocity.

Three commonly used Hugoniot relationships are the shock velocity-particle velocity Hugoniot, U_s-$\dot{x}$, the pressure-particle velocity Hugoniot, p-$\dot{x}$, and the pressure-volume Hugoniot, p-v. The U_s-$\dot{x}$ Hugoniot is found to be generally linear for most materials. As such, it is expressed in the form

$$U_s = C_B(sgn[\![\dot{x}]\!]) + A[\![\dot{x}]\!] \qquad \text{eq. 29}$$

where C_B is the material bulk sound speed, $sgn[\![\cdot]\!]$ is the sign of the difference operation and A is a dimensionless constant determined from experimental data. The p-$\dot{x}$

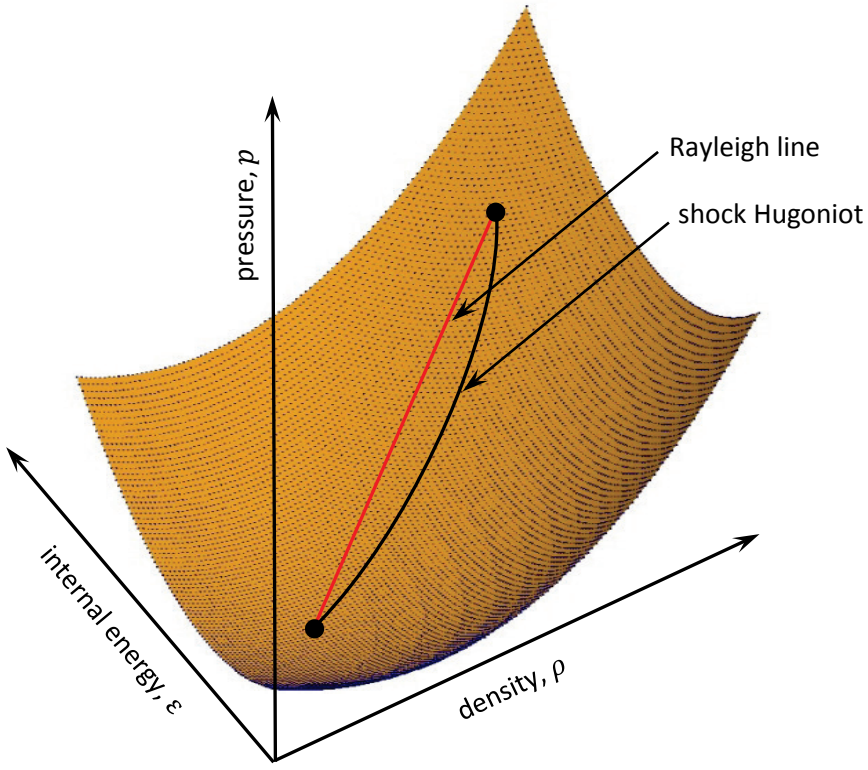

(a)

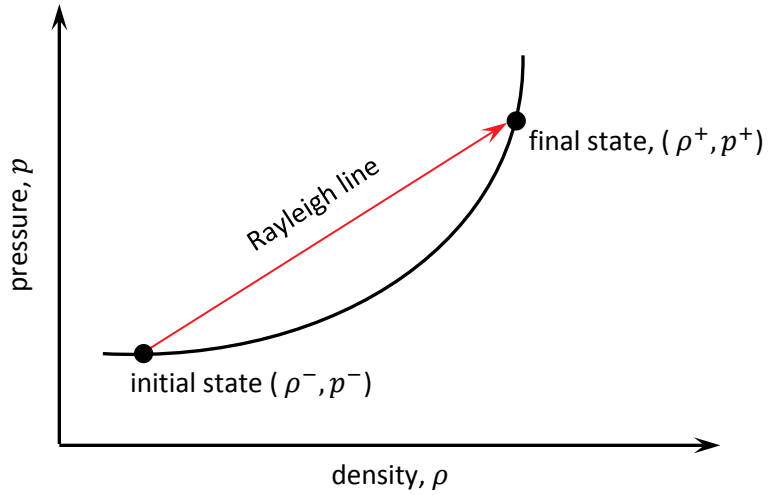

(b)

Figure 2. (a) Equation of state relationship expressed in terms of pressure, internal energy and density (adapted from [94]), b) pressure-density Hugoniot plane

Hugoniot is obtained by substituting the definition of U_s from eq. 29 into the jump eq. 21 to give

$$[\![p]\!] = \rho^R\{C_B(sgn[\![\dot{x}]\!]) + A[\![\dot{x}]\!]\}[\![\dot{x}]\!] \qquad \text{eq. 30}$$

The *p*-*v* Hugoniot expression is derived by using eq. 29 in conjunction with the jump eq. 20 and eq. 21 to give

$$[\![p]\!] = \frac{(\rho^R C_B)^2(v^- - v^+)}{[1 - \rho^R A(v^- - v^+)]^2} \qquad \text{eq. 31}$$

The common method used to experimentally determine Hugoniot response curves is flyer plate impact experiments [88, 89, 95]. The flyer plate experiments are repeated with varying impact conditions so that a number of end shock states are achieved, all shocked from the same initial state. Multiple end-state points are collected along the Hugoniot, essentially tracing the Hugoniot curves. Pressure and particle velocity data are typically collected from the impact experiments. Using these data, the shock front velocity may be determined from the Rayleigh line eq. 23. With this information the other Hugoniot curves can be fully determined.

3.3 Interface effects

An important consideration in the study of solid materials' hydrodynamic response to shock loading is wave reflections and interaction at material interfaces. In the case of brittle materials these interface effects can lead to spall fracture or dynamic fracture, which occurs when shock-induced tensile stresses exceed the materials' tensile strength. Shock waves are

initially generated as traveling compressive waves, such as from a blast wave impinging on a structure or a projectile impacting a target. Since the initial wave generation is compressive in nature, additional phenomena must be responsible for the generation of tensile stresses. These phenomena are interface effects, or the generation of wave reflections at material interfaces that interact with the initial incident wave to create tensile stresses. The location and magnitude of tensile stresses are driven by the wave interactions.

Two types of material interfaces can be considered in the generation of shock wave reflections [96]. The simplest type occurs at the material free surface, where the interface is between the solid material and air. As an incident compression wave impinges on the free surface, a reflected wave is generated to satisfy the traction free condition at the material boundary. The reflected wave, which is tensile in nature, propagates back into the material. Depending on the shape of the trailing portion of the incident compressive wave, interaction of the incident and reflected waves can result in a region of tensile stress near the free surface. When the tensile stress is large enough to exceed the material's dynamic tensile strength, spall fracture occurs. The formation of shock-induced spall fracture due to free surface reflections is commonly observed experimentally, and is often used to measure the so-called spall strength of the material [97, 98, 99]. An example of shock-induced spall resulting from a contact detonation experiment is shown in Figure 3. The second type of interface to be considered is between dissimilar components of a heterogeneous material. The process for generation of tensile stresses is similar to the free surface case, but here

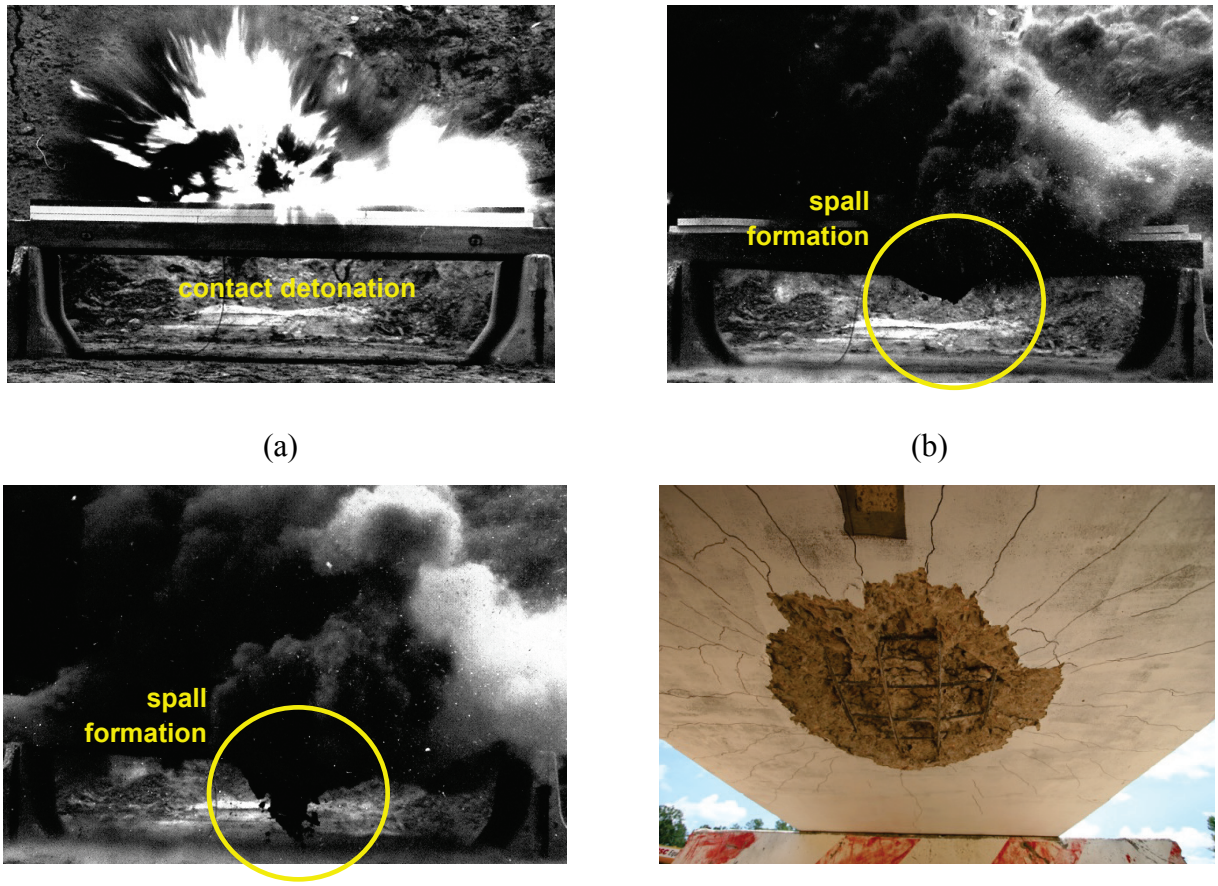

Figure 3. Spall due to contact detonation on concrete slab, a) time = 0 msec, b) time = 14 msec, c) time = 53 msec, and d) final spall condition on bottom of slab (courtesy ERDC)

reflected wave properties are governed by the so-called impedance mismatch condition of the materials (discussed further below). The key interface compatibility conditions are continuity of pressure and particle velocity; these terms dictate the reflected wave conditions at the interface. Analytically, the compatibility conditions can be enforced directly from the p-$\dot{x}$ Hugoniot, given in eq. 30. The p-$\dot{x}$ Hugoniot can be written for each material at the

interface, where the pressure and particle velocity conditions ahead of the shock front, i.e., p^- and $\dot{x}^-$, are assumed to be known from the initial state. The compatibility conditions dictate that pressure and particle velocity behind the reflected wave, i.e., p^+ and $\dot{x}^+$, be continuous, giving two equations written in terms of the two unknowns.

A term often used in the discussion of interface reflections is material shock impedance, commonly denoted as Z [87]. The equation for shock impedance is given as

$$Z = \rho^R U_s \qquad \text{eq. 32}$$

where ρ^R is initial density of the material and U_s is the shock front velocity. With reference to the Rayleigh line eq. 23, the shock impedance is the ratio between the jump in pressure and particle velocity across a shock front

$$Z = \rho^R U_s = \frac{[\![-p]\!]}{[\![\dot{x}]\!]} \qquad \text{eq. 33}$$

In practice, shock impedance is used for relative comparison of the shock propagation characteristics of materials joined at an interface, which gives an indication of the nature of the reflected wave. Graphically, shock impedance is an indicator of the shape and slope of the pressure-particle velocity Hugoniot, as shown in Figure 4.

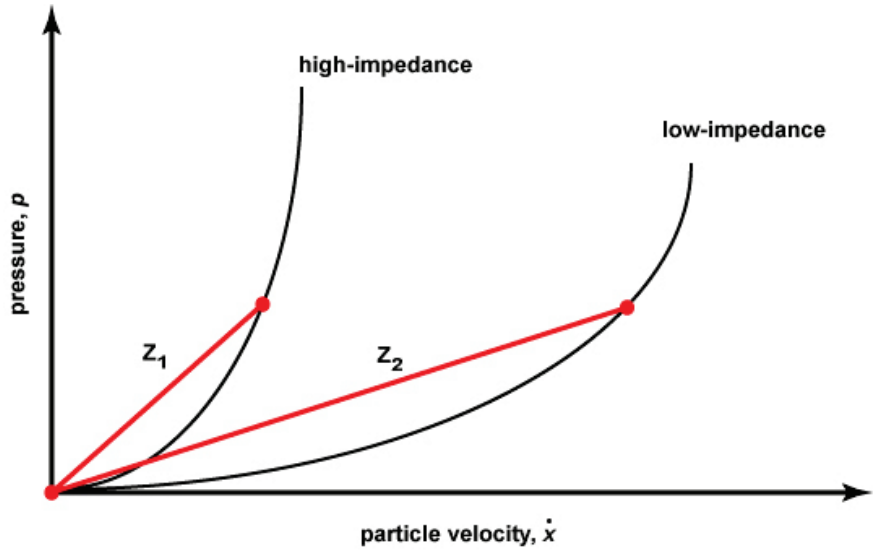

Figure 4. Comparison of high-impedance (Z_1) and low-impedance (Z_2) materials in the p-$\dot{x}$ Hugoniot plane

Comparison of material impedances, also known as defining the so-called impedance mismatch, indicates whether the reflected wave will "shock-up" or "shock-down" from the incident wave. According to Cooper [87], for the case of a shock wave propagating from a low-impedance material into a material with higher impedance, the reflected wave pressure will be greater than the incident, or a shock-up condition occurs. As a general statement, shock-up conditions do not lead to the generation of tensile stresses [96]. Conversely, when a shock wave propagates across an interface from a high-impedance material to a material with lower impedance the reflected pressure is lower than the incident, creating a shock-down condition [87]. Shock-down conditions can lead to regions of tensile stress [96].

3.4 Second law of thermodynamics and the entropy constraint

The discontinuous solution of a conservation equation is not always uniquely determined solely by the numerical solution of the governing conservative equation. For example, consider the one-dimensional hyperbolic conservation law

$$u(x,t)_{,t} + (u^2/2)_{,x} = 0 \qquad \text{eq. 34}$$

with the initial conditions

$$u(x,0) = \begin{cases} 0 & x < 0 \\ 1 & x \geq 1 \end{cases} \qquad \text{eq. 35}$$

There are two possible solutions that satisfy this initial value problem

$$u(x,t) = \begin{cases} 0 & x/t < 0.5 \\ 1 & x/t \geq 0.5 \end{cases} \qquad \text{eq. 36}$$

$$u(x,t) = \begin{cases} 0 & x/t < 0 \\ x/t & 0 \leq x/t \leq 1 \\ 1 & x/t > 1 \end{cases} \qquad \text{eq. 37}$$

where eq. 36 describes a shock solution and eq. 37 describes a rarefaction solution. Although both solutions satisfy the conservation equation, only one solution (the rarefaction solution in this case) is admissible according to the second law of thermodynamics. The second law of thermodynamics states that for an irreversible and adiabatic process in a closed thermodynamic system $\partial S > 0$, where S is entropy of the system. In this investigation the shock process is assumed to be irreversible and adiabatic based on the extremely short time scale of the shock event, as such the second law of thermodynamics requires that entropy must increase across a shock. Considering this requirement of the second law, the question is

now "what is the constraint for an increase in entropy to occur?" To describe this entropy production constraint, the proof by Jeffrey and Tanuiti [100] is referred to. First consider a material with a compressive shock, where the material ahead of the discontinuity has internal energy e_0 and the material behind the discontinuity has internal energy e_1. From the relationship between internal state variables, $p = f(v, e)$, where p is pressure and v is specific volume, a curve, E_0, is assumed to exist in the pressure-volume space that describes all of the possible $p - v$ states that can exist for an internal energy e_0. A similar curve, E_1, is assumed for internal energy e_1. Letting (e_0, p_0, v_0) be the state ahead of the jump and (e_1, p_1, v_1) be the state behind, the jump from E_0 to E_1 is shown schematically in Figure 5.

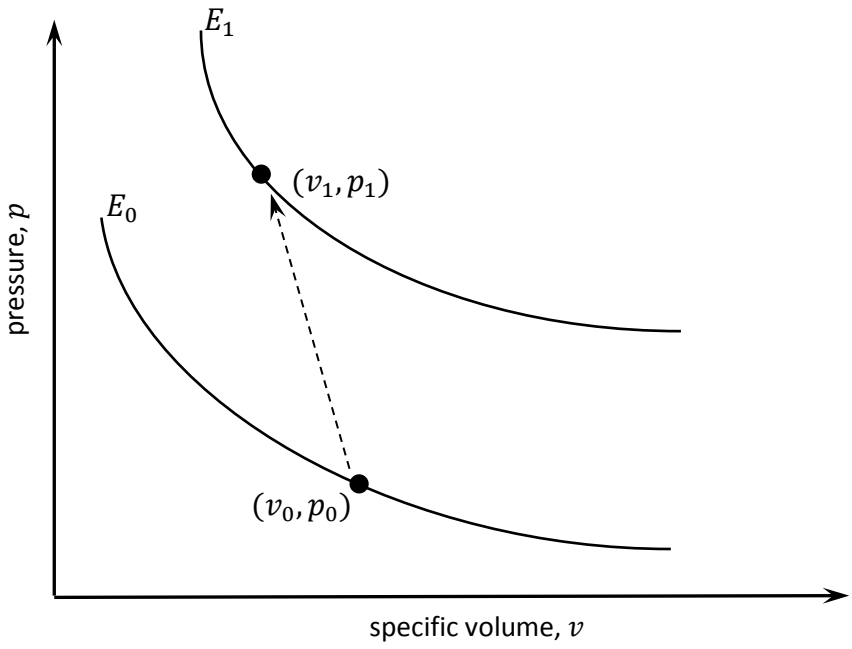

Figure 5. Energy jump across a compressive shock

The fact that curve E_1 lies above E_0 in Figure 5 is proven in Jeffrey and Tanuiti [100], and states that internal energy of a material increases across a compressive shock. Now consider an isentrope, or line of constant entropy, that passes through (e_1, p_1, v_1) with entropy S_1. Jeffrey and Tanuiti [100] prove that the slope of the isentrope is greater than that of E_0 or E_1 at any point along these constant internal energy curves. As a consequence, the isentrope intersects E_1 and E_0 as shown in Figure 6. The isentropic curve intersects E_0 at the point (v', p') so that the entropy at this point is also S_1. The entropy at the point (v_0, p_0) is S_0. Now all that remains in defining the nature of the entropy change across the jump is to define the relationship between S_0 and S_1.

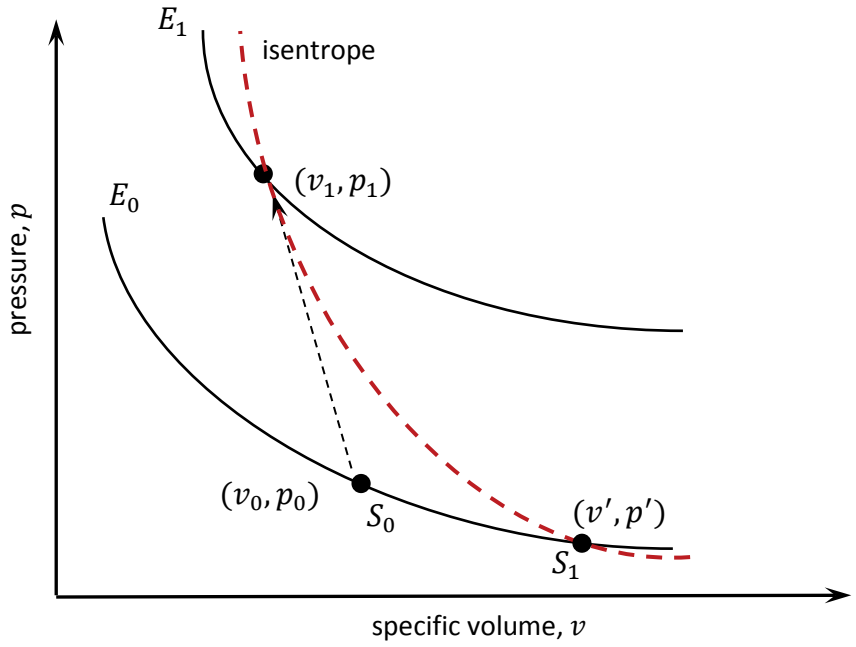

Figure 6. Isentropic line at a compressive shock jump

Consider the definition of entropy

$$\Theta\, dS = de + p\, dv \qquad \text{eq. 38}$$

where Θ is absolute temperature. Along the curve E_0, internal energy is constant so that $de = 0$. Further, p remains positive for the compressive shock so that only the change in specific volume, dv, is considered. Moving from the entropy state ahead of the shock, S_0, to the entropy state behind the shock, S_1, the specific volume increases from v_0 to v'. According to eq. 38 and using the conditions stated above, this implies that $dS > 0$. Therefore, this shows that jumping from the state (v_0, p_0) to the state (v_1, p_1) results in a change in entropy where $S_1 > S_0$, that is to say, entropy increases. Otherwise stated, this shows that in the case of a discontinuity where $v_1 < v_0$ entropy must increase. Jeffrey and Tanuiti [100] further show by the same process that in the case of a discontinuity where $v_1 > v_0$ entropy must decrease. Now referring back to the second law of thermodynamics, this shows that entropy only increases for a compressive discontinuity, and therefore compressive discontinuities exist as shocks. However, since entropy decreases across an expansion discontinuity, these types of discontinuities immediately degenerate into smooth expansion waves or rarefaction waves. This relationship between specific volume and entropy change forms the entropy production constraint for shock wave formation and propagation.

Referring back to the conservation law problem in eq. 34 and eq. 35, the entropy constraint indicates that the physically admissible solution can be determined by the specific volume change across the jump. One straightforward way to determine this is by

characteristic projections. Using characteristic projections (discussed further in Section 4.4.2) the specific volume change across the discontinuity is negative. Therefore, the rarefaction solution is the entropy-correct solution to this conservation law problem. Other techniques have been developed to enforce this entropy constraint in a numerical framework. Lax [101] proposed a simple constraint for convex scalar flux functions known as the Lax shock condition; Oleinik [102] proposed a more general form applicable to non-convex scalar flux functions. Entropy inequalities, e.g. [103, 104], have been developed to enforce the entropy constraint. The Riemann solution in Godunov's method [39] guarantees entropy satisfaction. Other approximate Riemann solvers for systems of equations, such as Roe's method [105, 106], require an additional entropy fix [107, 108]. Chessa and Belytschko [109] suggested the use of a local Riemann problem to satisfy entropy production in a finite element formulation.

3.5 Numerical error at the shock

Accurately capturing the fine scale structure of the shock front is critical for numerical modeling of shock effects. The desired result is sharp definition of the discontinuity without excessive oscillation or dissipation in the solution. Oscillations that stem from Gibbs phenomenon can result in significant over-prediction of field and state variables, which may lead to premature material failure in the model. Likewise, excessive dissipation can result in poor resolution of the front location and an under-prediction of the shock solution.

Spurious oscillations and/or excessive dissipation in the discontinuous solution of a partial differential equation (PDE) can be described by Gibbs phenomenon effects [43] and the presence of dissipative or dispersive terms in the approximating equations [36]. Gibbs phenomenon describes numerical oscillation from the perspective of frequency analysis, where the truncation of higher-frequency components in the approximation yields persistent and non-physical solution oscillation [43]. Analysis of the approximation equations, particularly in the FD method, also shows that dissipative or dispersive effects may result directly from truncation error in the approximation [36]. Methods to improve the numerical approximation of discontinuous solutions can be developed by mitigating both Gibbs phenomenon and the dissipative or dispersive effects.

3.5.1 Gibbs phenomenon

Gibbs phenomenon is formally defined as the presence of persistent oscillations in the numerical approximation of a discontinuous function by Fourier series analysis [43]. It is observed that when a truncated Fourier sine/cosine series is used to approximate a discontinuous function, oscillations arise near the discontinuity. With the inclusion of additional series terms the oscillations localize to the jump, yet remain persistent (converging to an amplitude 1.18 times greater than the true solution at the front). In contrast, the same is not true for Fourier series approximation of a smooth function, where oscillations do not occur even with a minimal number of series terms. An example of Gibbs phenomenon is shown in Figure 7a, where a step function is approximated using 10 and 100 terms. For

comparison, the Fourier series approximation of a smooth function, $f(x) = x^2$, using the same number of terms is shown Figure 7b. The series approximation equations are found in any standard mathematical text, e.g., [110]. As seen Figure 7a, with increasing series terms the approximate solution behind the jump improves, but oscillations persist in the immediate vicinity of the discontinuity. In Figure 7b, the smooth function approximation does not exhibit any persistent oscillation. These examples show how a discontinuous function contains an infinite series of high-frequency components and their truncation in a numerical approximation results in persistent oscillation at the jump.

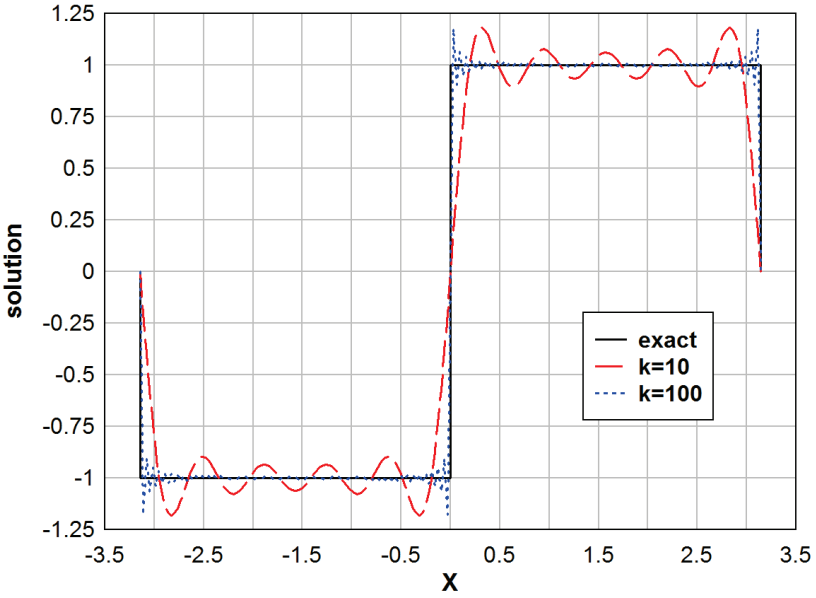

(a)

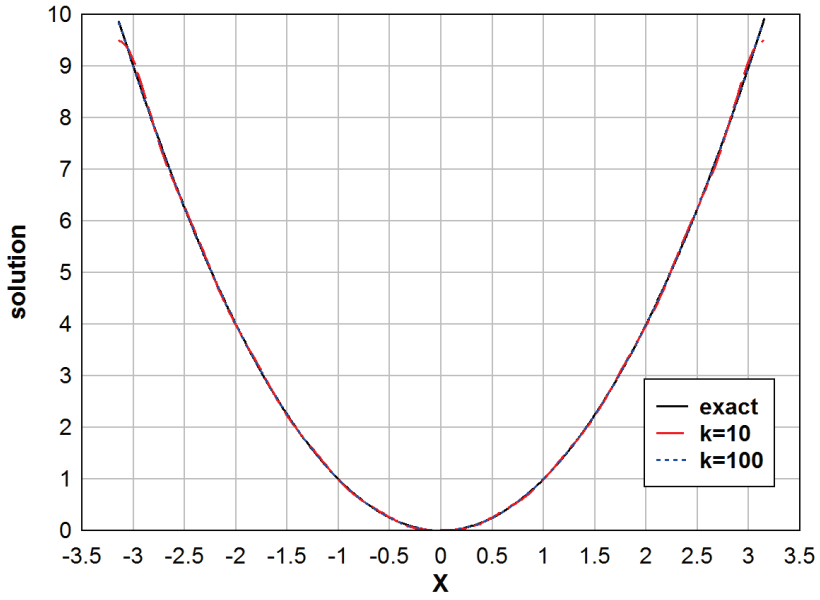

(b)

Figure 7. Fourier series approximation of a) step function showing Gibbs phenomenon, and b) smooth function without persistent oscillation (k = number of series terms)

3.5.2 Dissipation and dispersion due to truncation error

For FD schemes in particular, the numerical error at the discontinuous solution has also been described in terms of dissipative and/or dispersive terms resulting from truncation error in the approximation [36]. To describe the presence of dissipative truncation error, consider a simplified model equation for the linear one dimensional wave equation

$$\frac{\partial u(x,t)}{\partial t} + c\frac{\partial u(x,t)}{\partial x} = 0 \qquad \text{eq. 39}$$

where $u(x,t)$ is the displacement solution and c is a constant wave speed. Consider the Lax method solution of eq. 39, which provides a first-order accurate solution that is non-oscillatory but also dissipative. The Lax method difference equation is [36]

$$u_j^{n+1} = \frac{1}{2}\left(u_{j+1}^n + u_{j-1}^n\right) - \frac{c\Delta t}{2\Delta x}\left(u_{j+1}^n - u_{j-1}^n\right) \qquad \text{eq. 40}$$

where the position of calculation points is $j\Delta x$, Δt is the time increment, and Δx is the calculation point spacing. Tannehill et al. [36] use Taylor series expansion of u_j^{n+1}, u_{j+1}^n, and u_{j-1}^n, to obtain

$$\frac{\partial u}{\partial t} + c\frac{\partial u}{\partial x} = \frac{c\Delta x}{2}\left(\frac{1}{v} - v\right)\frac{\partial^2 u}{\partial x^2} + \frac{c(\Delta x)^2}{3}(1 - v^2)\frac{\partial^3 u}{\partial x^3} + \cdots \qquad \text{eq. 41}$$

where v is the Courant number

$$v = \frac{c\Delta t}{\Delta x} \qquad \text{eq. 42}$$

The left hand side of eq. 41 matches the model eq. 39, and the right hand side represents the approximation error. The leading error term is observed to be a function of $\partial^2 u/\partial x^2$, which is analogous to the presence of a viscosity term for viscous fluid flow. Therefore, as a result of the truncation error a viscous term is naturally included in the approximation. This is sometimes referred to as "implicit viscosity" [36]. The effect of this kind of approximation in problems with discontinuities is the introduction of dissipation, which naturally eliminates solution oscillations but also tends to reduce sharpness of the discontinuous front. According to Tannehill et al. [36], first-order FD approximation schemes generally exhibit implicit viscosity and are therefore non-oscillatory but also exhibit reduced accuracy in resolution of the shock front.

To investigate the dispersive effects of truncation error, model eq. 39 can be approximated by a second-order accurate FD equation. Here the well-known Lax-Wendroff equation is used. The Lax-Wendroff difference equation is [36]

$$u_j^{n+1} = u_j^n - \frac{c\Delta t}{2\Delta x}\left(u_{j+1}^n - u_{j-1}^n\right) + \frac{c^2(\Delta t)^2}{2(\Delta x)^2}\left(u_{j+1}^n - 2u_j^n + u_{j-1}^n\right) \qquad \text{eq. 43}$$

Rewriting eq. 43 in the same manner as eq. 41, the following is obtained

$$\frac{\partial u}{\partial t} + c\frac{\partial u}{\partial x} = -c\frac{(\Delta x)^2}{6}(1-v^2)\frac{\partial^3 u}{\partial x^3} - \frac{c(\Delta x)^3}{8}v(1-v^2)\frac{\partial^4 u}{\partial x^4} + \cdots \qquad \text{eq. 44}$$

where again, the left-hand side matches the original model equation and the right-hand side is the truncation error. In this case the leading error term is a function of $\partial^3 u/\partial x^3$. When this term is dominant, dispersion may occur so that phase error is introduced into the frequency

components of the solution and cause solution oscillation. This form of dispersion error is typical of higher-order accurate schemes [36].

From consideration of the Lax and Lax-Wendroff methods, the key point is that dissipation or dispersion may naturally enter the approximation through truncation error. Dissipative effects, typical of first-order accurate schemes, tend to introduce implicit viscosity which eliminates oscillations but also reduces accuracy of the shock front resolution. Dispersive effects are typical of higher-order schemes and tend to yield sharp jumps but also induce solution oscillation. Therefore, an approach that combines the two might be used to minimize both oscillation and dissipation. This is the essential idea behind flux limiter improvement of shock solutions, where the solution accuracy is adaptively reduced at the shock front and remains higher-order accurate elsewhere.

3.6 Monotonicity and total variation

In the development of numerical methods to model discontinuous problems, the concept of monotonicity is widely used as a descriptor of oscillation-free schemes. In general, a monotone scheme is one that does not spuriously produce new solution extrema. The Lax method is a monotone scheme. However, due to oscillations formed by the Lax-Wendroff method it is non-monotone. The theorem of S.K. Godunov [39] formally states that linear numerical schemes greater than first-order accurate cannot guarantee a monotone solution. This is also known as Godunov's order barrier theorem, which shows that for a linear, one-step, higher-order accurate solution to a PDE such as

$$\frac{\partial \varphi}{\partial t} + c\frac{\partial \varphi}{\partial x} = 0 \qquad t > 0, \quad x \in \mathbb{R} \qquad \text{eq. 45}$$

monotonicity is only guaranteed under the condition

$$\upsilon = c\frac{\Delta t}{\Delta x} \in \mathbb{N} \qquad \text{eq. 46}$$

where υ is the Courant number, $\mathbb{R}$ is the set of real numbers and $\mathbb{N}$ is the set of natural numbers. Adopting the CFL condition for stability, satisfaction of eq. 46 only occurs when $\upsilon = 1$.

Total variation (TV) is used to quantify the evolution of local extrema in the solution and therefore provides a measure of monotonicity, or lack thereof. The discrete form of the TV equation for a numerical solution at time step *n* is given as

$$TV(u^n) = \sum_{j=1}^{numpts-1} \left|u_{j+1}^n - u_j^n\right| \qquad \text{eq. 47}$$

Monotone schemes exhibit the total variation diminishing (TVD) condition such that

$$TV(u^{n+1}) \leq TV(u^n) \qquad \text{eq. 48}$$

Harten proved that monotone schemes are TVD, and that TVD schemes preserve monotonicity in the solution [36, 111].

3.7 Limiters and artificial viscosity

Two traditionally used approaches for improvement of discontinuous solutions are the use of limiters and artificial viscosity. Limiters essentially reduce higher-order accurate methods to a first-order scheme near a discontinuity. This tends to minimize oscillation without inducing excessive dissipation. Artificial viscosity explicitly introduces dissipation to the problem in order to transform the discontinuity into a smooth jump over a thin transition zone. As a consequence the discontinuity is smoothed and oscillation is reduced, but a subjective length scale is also required for the transition zone definition.

3.7.1 Limiters

Limiters are constructed by modifying otherwise higher-order schemes in the vicinity of a discontinuity to give a first-order approximation in that region. The result is to provide monotone or near-monotone schemes that capture the discontinuity profile without excessive dissipation. Traditionally limiters are constructed by formulating a higher-order difference equation so that higher-order terms are adaptively suppressed by multiplication with an embedded limiter function [36]. The limiter functions can be designed so that they are not active in smooth solution regions, but in strong gradient regions they suppress the higher-order approximation terms.

As an example of formulating a limiter-modified FD scheme, consider the following form of the Lax method solution to Burgers' equation [36]

$$u_j^{n+1} = u_j^n - \frac{\Delta t}{\Delta x}\left[f_{j+1/2}^n - f_{j-1/2}^n\right] \quad \text{eq. 49}$$

where $f_{j+1/2}^n$ is the numerical flux given by

$$f_{j+1/2}^n = \frac{1}{2}\left[F_j^n + F_{j+1}^n - \frac{\Delta x}{\Delta t}\left(u_{j+1}^n - u_j^n\right)\right] \quad \text{eq. 50}$$

where $F_{j+1}^n = 1/2\left(u_{j+1}^n\right)^2$. Also consider an expression of the Lax-Wendroff solution in the same form as eq. 49, but with the numerical flux given as [36]

$$f_{j+1/2}^n = \frac{1}{2}\left(F_j^n + F_{j+1}^n\right) - \frac{1}{2}\frac{\Delta t}{\Delta x}\left(u_{j+1/2}^n\right)^2\left(u_{j+1}^n - u_j^n\right) \quad \text{eq. 51}$$

Taking the difference between eq. 50 and eq. 51 gives the difference between the Lax and Lax-Wendroff fluxes. If this difference is added back to the Lax flux in eq. 50 a modified flux, $f_{j+1/2}^{n^*}$, is defined.

$$f_{j+1/2}^{n^*} = \frac{1}{2}\left[F_j^n + F_{j+1}^n - \frac{\Delta x}{\Delta t}\left(u_{j+1}^n - u_j^n\right)\right] + \phi\frac{\Delta x}{\Delta t}\left(\frac{u_{j+1}^n - u_j^n}{2}\right)\left[1 - \left(u_{j+1/2}^n\frac{\Delta t}{\Delta x}\right)^2\right] \quad \text{eq. 52}$$

The modified flux can also be enriched with a limiter function, ϕ, that acts on the higher order terms (reference eq. 52). The limiter function varies between 0 and 1, where in this case $\phi = 1$ recovers the second-order accurate Lax-Wendroff equation and $\phi = 0$ recovers the first-order Lax equation. As a consequence, the limiter transforms the numerical approximation between higher-order accuracy in smooth regions of the solution and first-order accuracy at discontinuities.

3.7.2 Artificial viscosity

The purpose of artificial viscosity is to explicitly incorporate dissipation into higher-order numerical schemes so that perfect discontinuities are transformed into smooth transition layers. Since artificial viscosity is dissipative in nature, the key is to incorporate it in a way to minimize oscillation without excessive smoothing of the discontinuity. This generally requires the definition of non-physical parameters in the viscosity expression, which introduces subjectivity to the formulation. Regardless, artificial viscosity is widely used as an effective means to mitigate spurious solution oscillation in shock propagation problems.

Artificial viscosity was initially proposed by VonNeumann and Richtmyer [59] for one dimensional fluid dynamics problems. In their formulation an artificial pressure term, q, was added to the conservation equations of momentum and energy, and was proposed in quadratic form [59]

$$q = \frac{(c_0 \Delta x)^2}{V} \frac{\partial \dot{x}}{\partial x} \left| \frac{\partial \dot{x}}{\partial x} \right| \qquad \text{eq. 53}$$

where V is specific volume, c_0 is a dimensionless parameter, and $c_0 \Delta x$ is a length term governing the width of the shock transition layer. With increasing $c_0 \Delta x$, solution oscillations are reduced but at the expense of greater shock front smearing. The value of c_0 was proposed to be 1.5 to 2 so that the shock front is smoothed over 3 to 4 calculation cells [61]. Since the artificial pressure is a function of the square of velocity gradient, it is active in strong gradient regions but negligible in regions of smooth flow. As an example of the use of

artificial viscosity, the solution to a one dimensional plane wave propagation problem is shown in Figure 8. Strong form of the problem statement and second-order difference equations were taken directly from Richtmeyer and Morton [61]. The term c_0 equals 0.4 and 2 in Figure 8a and Figure 8b, respectively. In each figure the pressure solution and computed artificial pressure are given. It is observed that once the solution is sufficiently non-oscillatory the artificial pressure is only active at the jump. Further, oscillations are significantly reduced with increasing $c_0\Delta x$, which is accompanied by an increase in width of the transition layer. A combination of linear and quadratic terms in the artificial viscosity expression was later proposed [60, 62]

$$q = \frac{(c_0\Delta x)^2}{V}\frac{\partial \dot{x}}{\partial x}\left|\frac{\partial \dot{x}}{\partial x}\right| + \frac{c_L}{V}a\Delta x\left|\frac{\partial \dot{x}}{\partial x}\right| \qquad \text{eq. 54}$$

where c_L is another dimensionless parameter (stated to be ~1) and a is the local sound speed. The purpose of including the linear term in eq. 54 was to improve oscillation damping behind the shock front (reference the persistent, low amplitude oscillations in Figure 8b). This combined form is very similar to what is currently used in many modern codes, where the velocity gradient is replaced by the trace of the strain rate tensor [65]

$$q = \frac{l}{V}(C_0 l\dot{\varepsilon}_{kk}^2 - C_1 a\dot{\varepsilon}_{kk}) \qquad \text{eq. 55}$$

where l is the characteristic length measurement, C_0 and C_1 are constants and $\dot{\varepsilon}_{kk}$ is the volumetric strain rate. In modern FE applications, the linear term of eq. 55 is viewed as the mechanism to control oscillation behind the jump. The quadratic term is viewed as a

mechanism to avoid excessive volumetric strain (and so-called element collapse) by applying the artificial pressure at the shock jump while the hydrostatic internal force evolves through the shock transition.

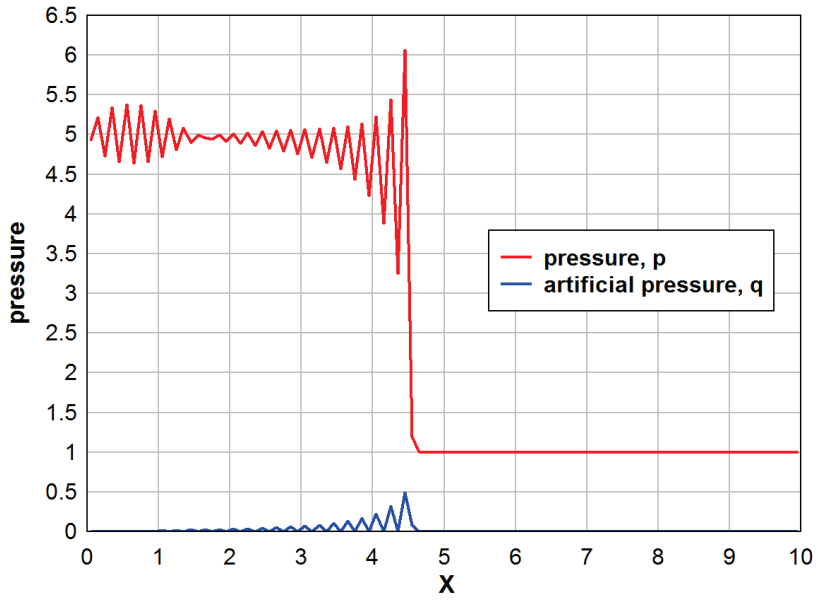

(a)

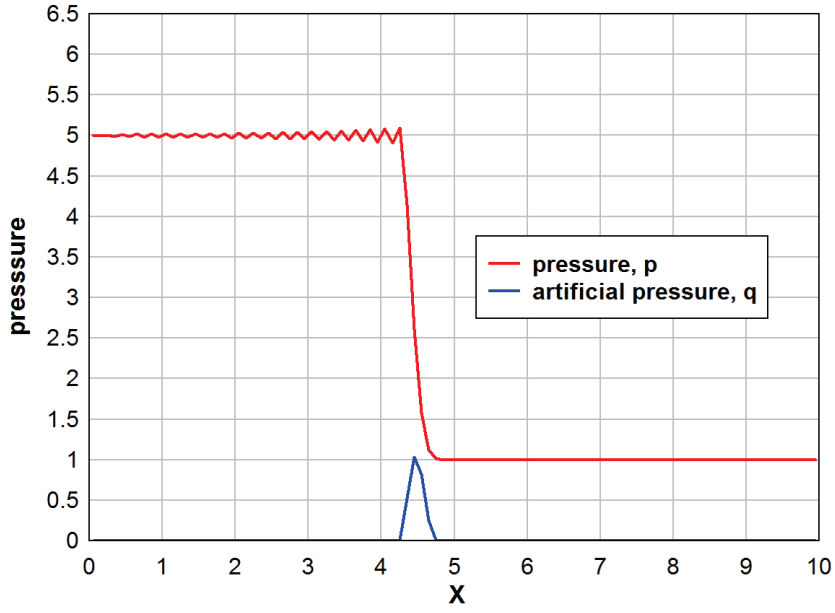

(b)

Figure 8. Plane wave propagation using 2nd order difference equations and artificial viscosity, (a) $c_0 = 0.4$ and (b) $c_0 = 2$; $\Delta x=0.1$, $\Delta t=0.0016$ in both cases

CHAPTER 4 RKPM FORMULATION FOR SHOCK-FORMING SCALAR CONSERVATION LAWS

Accurate shock modeling requires that two critical issues be addressed in the numerical formulation: 1) correct representation of the essential shock physics, and 2) control of Gibbs phenomenon oscillation at the shock. The first issue requires embedment of the correct shock physics into the formulation; the second deals with control on the oscillatory instability that results from approximation of the discontinuous solution. The essential shock physics include the Rankine-Hugoniot (R-H) jump condition and the second law of thermodynamics for entropy production. The relationship between shock velocity and the state or field variable jump at the shock is defined by the R-H condition. This provides the connection between continuous fields adjacent to the discontinuity and satisfaction ensures correct velocity of the shock front. The second law of thermodynamics requires that entropy must increase during an irreversible adiabatic process. This provides a conditional constraint on the physically correct shock solution, namely that discontinuities in a compressive state propagate as shocks and discontinuities in an expansion state degenerate to rarefactions, e.g. [100]. To satisfy this entropy condition, numerical formulations are typically enriched with an entropy production constraint [101, 102, 104, 107, 108, 112, 113].

In this chapter a stable (oscillation limiting) and flux conserved RKPM formulation is

developed for shock-forming scalar conservation laws. This formulation is developed as a foundation for extension to the equations of nonlinear solids in the following chapter. To construct the formulation a smoothed flux divergence is formed under the framework of SCNI. This new flux divergence is then locally enriched with a Riemann solution to satisfy the physics of entropy production. The Riemann-enriched flux divergence is embedded into the meshfree formulation through a velocity correction that also provides oscillation control at the shock. The correction is constrained to the shock region using an automatic shock detection algorithm that is constructed using the intrinsic spectral decomposition feature of the RK approximation. Several numerical examples are provided at the end of the chapter to verify accuracy of the proposed scalar law formulation.

4.1 Reproducing kernel approximation

The RK approximation [24, 25] of a function, $u(\boldsymbol{x})$, is derived from the convolution

$$\bar{u}(\boldsymbol{x}) = u(\boldsymbol{x}) * \bar{\phi}_a^n(\boldsymbol{x}) = \int_{-\infty}^{\infty} u(\boldsymbol{\tau})\, \bar{\phi}_a^n(\boldsymbol{x}; \boldsymbol{x}-\boldsymbol{\tau})\, d\tau \qquad \text{eq. 56}$$

where $\bar{u}(\boldsymbol{x})$ is the approximation of $u(\boldsymbol{x})$ and $\bar{\phi}_a^n(\boldsymbol{x}; \boldsymbol{x}-\boldsymbol{\tau})$ is an n^{th} order complete reproducing kernel. Derivation of the RK approximation from this convolution is the essential link to its spectral filtering property discussed in the next section. The reproducing kernel is defined as

$$\bar{\phi}_a^n(\boldsymbol{x}; \boldsymbol{x}-\boldsymbol{\tau}) = C(\boldsymbol{x}; \boldsymbol{x}-\boldsymbol{\tau})\phi_a(\boldsymbol{x}-\boldsymbol{\tau}) \qquad \text{eq. 57}$$

where $\phi_a(\boldsymbol{x}-\boldsymbol{\tau})$ is a kernel function of compact support size a and $C(\boldsymbol{x};\boldsymbol{x}-\boldsymbol{\tau})$ is a correction function that imposes n^{th} order reproducibility according to an n^{th} order complete monomial basis. The RK approximation expressed in eq. 56 is the so-called continuous form. For the numerical solution of an initial-boundary value problem, the partial differential equation is discretized in space with a set of np discrete points. Accordingly, a discrete form of the RK approximation is required [25]

$$u^h(\boldsymbol{x}) = \sum_{I=1}^{np} \Psi_I(\boldsymbol{x})\, d_I \qquad \text{eq. 58}$$

where $u^h(\boldsymbol{x})$ is the RK approximation, $\Psi_I(\boldsymbol{x})$ is the reproducing kernel shape function, and d_I are a set of nodal coefficients to be determined. The RK shape function is defined similar to the continuous reproducing kernel

$$\Psi_I(\boldsymbol{x}) = C(\boldsymbol{x};\boldsymbol{x}-\boldsymbol{x}_I)\,\phi_a(\boldsymbol{x}-\boldsymbol{x}_I) \qquad \text{eq. 59}$$

where $\phi_a(\boldsymbol{x}-\boldsymbol{x}_I)$ is a compact kernel function defining the approximation continuity and locality and $C(\boldsymbol{x};\boldsymbol{x}-\boldsymbol{x}_I)$ is the correction function that imposes the reproducing conditions. Using a set of n^{th} order complete monomials, the correction function is

$$\mathrm{C}(\boldsymbol{x};\boldsymbol{x}-\boldsymbol{x}_I) = \sum_{|\alpha|=0}^{n} (\boldsymbol{x}-\boldsymbol{x}_I)^{\alpha}\; b_{\alpha}(\boldsymbol{x}) \qquad \text{eq. 60}$$

$$= \boldsymbol{H}^T(\boldsymbol{x}-\boldsymbol{x}_I)\,\boldsymbol{b}(\boldsymbol{x}) \qquad \text{eq. 61}$$

where $|\alpha| \equiv \alpha_1+\alpha_2+\alpha_3$, $\quad (\boldsymbol{x}-\boldsymbol{x}_I)^{\alpha} \equiv (x_1-x_{1I})^{\alpha_1}(x_2-x_{2I})^{\alpha_2}(x_3-x_{3I})^{\alpha_3}$, and $b_{\alpha}(\boldsymbol{x}) \equiv b_{\alpha_1\alpha_2\alpha_3}(\boldsymbol{x})$. The n^{th} order complete basis functions are contained in $\boldsymbol{H}^T(\boldsymbol{x}-\boldsymbol{x}_I)$

$$\boldsymbol{H}^T(\boldsymbol{x}-\boldsymbol{x}_I)=[1,(x_1-x_{1I}),(x_2-x_{2I}),(x_3-x_{3I}),(x_1-x_{1I})^2,\dots,(x_3-x_{3I})^n] \quad \text{eq. 62}$$

The vector $\boldsymbol{b}(\boldsymbol{x})$ contains coefficients that are obtained by imposition of the reproducing conditions

$$\sum_{I=1}^{np}\Psi_I(\boldsymbol{x})\,x_{1I}^{\alpha_1}x_{2I}^{\alpha_2}x_{3I}^{\alpha_3}=x_1^{\alpha_1}x_2^{\alpha_2}x_3^{\alpha_3} \qquad |\alpha|=0,1,\cdots,n \quad \text{eq. 63}$$

which can be transformed to

$$\sum_{I=1}^{np}\Psi_I(\boldsymbol{x})\,(\boldsymbol{x}-\boldsymbol{x}_I)^{\alpha}=\delta_{\alpha_1 0}\delta_{\alpha_2 0}\delta_{\alpha_3 0} \qquad |\alpha|=0,1,\cdots,n \quad \text{eq. 64}$$

Now eq. 59 and eq. 61 are introduced to eq. 64 to obtain

$$\sum_{I=1}^{np}[\boldsymbol{H}(\boldsymbol{x}-\boldsymbol{x}_I)\boldsymbol{H}^T(\boldsymbol{x}-\boldsymbol{x}_I)\,\phi_a(\boldsymbol{x}-\boldsymbol{x}_I)]\boldsymbol{b}(\boldsymbol{x})=\boldsymbol{M}(\boldsymbol{x})\boldsymbol{b}(\boldsymbol{x})=\boldsymbol{H}(0) \quad \text{eq. 65}$$

$$\boldsymbol{b}(\boldsymbol{x})=\boldsymbol{M}^{-1}(\boldsymbol{x})\boldsymbol{H}(0) \quad \text{eq. 66}$$

where $\boldsymbol{M}(\boldsymbol{x})$ is the moment matrix, $\boldsymbol{H}^T(0)=[1,0,\dots,0]$, and the coefficients $\boldsymbol{b}(\boldsymbol{x})$ are determined by eq. 66. The RK shape function is then

$$\Psi_I(\boldsymbol{x})=\boldsymbol{H}^T(\boldsymbol{x}-\boldsymbol{x}_I)\boldsymbol{M}^{-1}(\boldsymbol{x})\boldsymbol{H}(0)\phi_a(\boldsymbol{x}-\boldsymbol{x}_I) \quad \text{eq. 67}$$

For time dependent problems the discrete RK approximation is written as

$$u^h(\boldsymbol{x},t)=\sum_{I=1}^{np}\Psi_I(\boldsymbol{x})\,d_I(t) \quad \text{eq. 68}$$

where the nodal coefficients, $d_I(t)$, are a function of time.

In the RK approximation the domain discretization is meshfree. As such, nodal interaction

occurs according to the overlap of kernel supports that is governed by the prescribed kernel locality. In this way the discretization is geometrically non-conforming. In contrast to mesh-based methods that impose strict conforming requirements on the element or cell discretization, mesh sensitivity is significantly reduced in the meshfree method. Consequently, meshfree methods like RKPM are well suited for problems involving large deformation, fragmentation, and evolving contact surfaces [35, 114, 115, 116]. A typical meshfree RKPM discretization for a large deformation impact problem is shown in Figure 9, where compact spherical kernels are used. Locality of the meshfree approximation is governed by kernel support size and the weighting function used in the kernel definition. The reproducing kernel shape function using a B-spline kernel and power function kernel is also shown. The B-spline is a smooth function that yields smooth weighting over the kernel support; the power function localizes weighting toward the node and is useful in rough solutions. The kernel selection can be specifically designed based on the desired continuity and locality properties of the meshfree approximation.

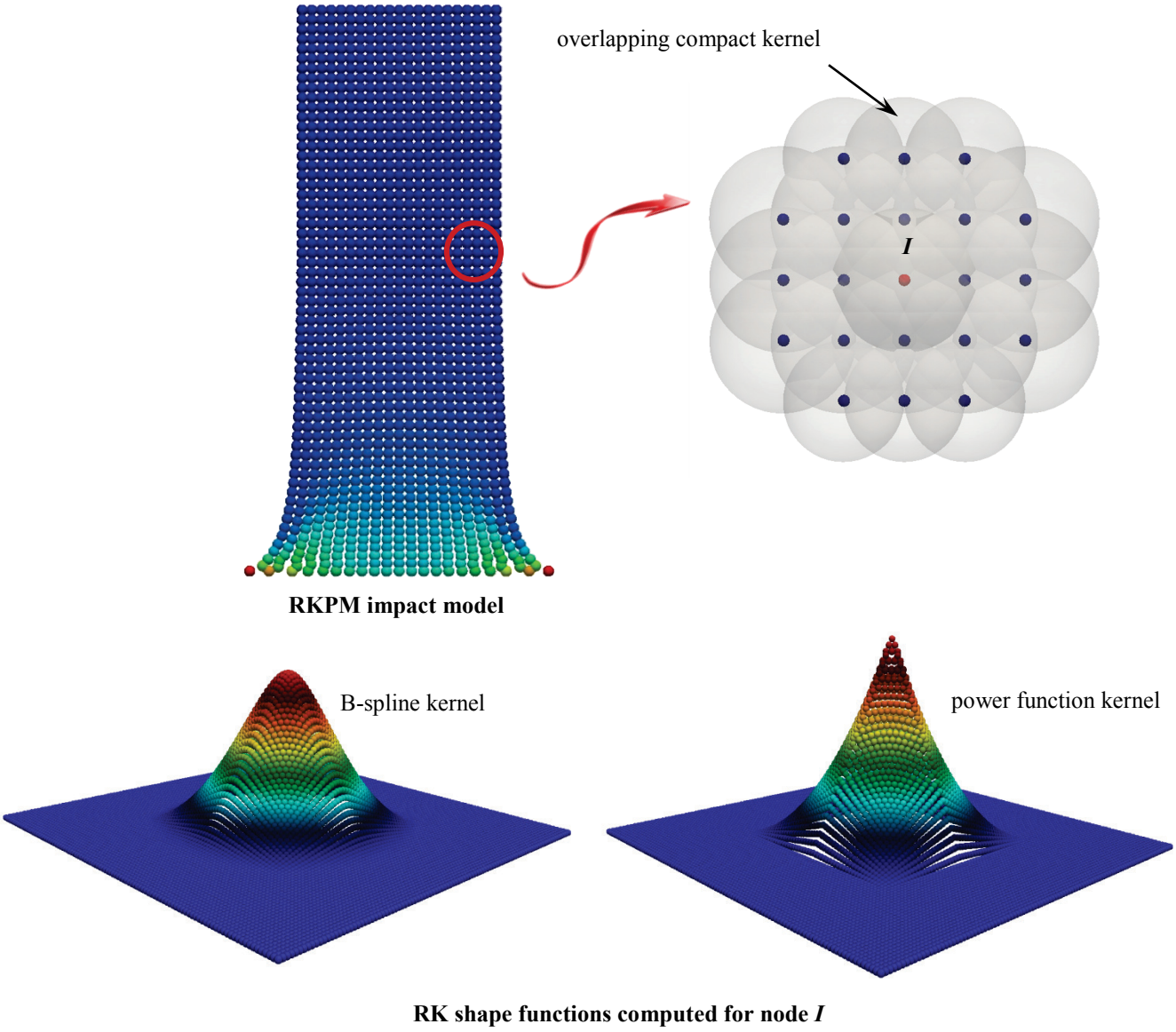

Figure 9. Typical meshfree discretization and RK shape functions using different kernel locality

4.2 Shock detection using RK spectral filters

For accurate shock modeling, automatic identification of the shock region is an important first step. In this formulation shock detection is used to identify regions where a local correction is applied to enforce the shock physics and oscillation control. Conveniently, the RK approximation possesses a unique spectral decomposition feature that behaves similarly to frequency filtering in wavelet filter analysis [68, 81]. This filtering property can be used in conjunction with the high frequency response spectra at a discontinuity to design a new algorithm for strong shock detection.

A wavelet filter is constructed through the convolution of an input signal, $g(\boldsymbol{x})$, and filter function, $\bar{f}(\boldsymbol{x})$

$$\bar{g}(\boldsymbol{x}) = g(\boldsymbol{x}) * \bar{f}(\boldsymbol{x}) = \int_{-\infty}^{\infty} g(\boldsymbol{\tau})\, \bar{f}(\boldsymbol{x}-\boldsymbol{\tau})\, d\tau \qquad \text{eq. 69}$$

where $\bar{g}(\boldsymbol{x})$ is the low-pass output of the filtering operation. The essential ingredient is the filter function that defines the pass band limit for the filtering operation. The RK approximation possesses an intrinsic spectral filtering property according to the correspondence between the convolution in eq. 56 and the filter defined in eq. 69. Through the convolution in eq. 56, the reproducing kernel $\bar{\phi}_a^n(\boldsymbol{x};\boldsymbol{x}-\boldsymbol{\tau})$, referred to as the approximation kernel hereon, is also a filter operating on $u(\boldsymbol{x})$. Polynomials up to order n are unfiltered in $\bar{u}(\boldsymbol{x})$ according to the reproducing condition. In this way the RK approximation is the filtered low-pass output, and the filter limit is defined according to the kernel basis. For functions that cannot be exactly reproduced (say a rational function), the

RK filter limit is also influenced by the support size dilation. In these cases the approximation kernel behaves as a low-pass filter where the filter limit contracts with a decrease in basis order or an increase in support size. You, Chen and Lu [68] defined another filter of the RK approximation

$$\hat{u}(\boldsymbol{x}) = \bar{u}(\boldsymbol{x}) * \hat{\phi}_b^m(\boldsymbol{x}) \qquad \text{eq. 70}$$

where $\hat{\phi}_b^m(\boldsymbol{x})$ is called a filter kernel that is constructed with basis order m (not necessarily equal to n) and support dilation b (not necessarily equal to a). The eq. 70 is a filter of the RK approximation itself, where $\hat{u}(\boldsymbol{x})$ is the low-pass output of the initial RK approximation. The discrete form of eq. 70 is [68]

$$u_{low}^h(\boldsymbol{x}, t) = \sum_{I=1}^{np}\left[\sum_{J=1}^{np} \Psi_I^{n,a}(\boldsymbol{x}_J)\, \Psi_J^{m,b}(\boldsymbol{x})\right] d_I(t) \qquad \text{eq. 71}$$

$$= \sum_{I=1}^{np} \Psi_I^*(\boldsymbol{x})\, d_I(t) \qquad \text{eq. 72}$$

where $\Psi_I^{n,a}(\boldsymbol{x}_J)$ and $\Psi_J^{m,b}(\boldsymbol{x})$ are RK shape functions computed with the indicated basis order and support size, and $u_{low}^h(\boldsymbol{x}, t)$ is the low-pass component of $u^h(\boldsymbol{x}, t)$. In eq. 72 $\Psi_I^*(\boldsymbol{x})$ is the filtering RK shape function, and the pass limit is designed according to the selected basis order and support size. The significance of this second filtering operation is that it provides a two-scale spectral decomposition of the discrete numerical solution

$$u_{high}^h(\boldsymbol{x}, t) = u^h(\boldsymbol{x}, t) - u_{low}^h(\boldsymbol{x}, t) \qquad \text{eq. 73}$$

where $u^h_{high}(\boldsymbol{x}, t)$ is the high-pass component of the RK approximation.

For shock forming problems the focus is on the approximate solution to discontinuities that form naturally according to the governing physics. Fourier series analysis shows that the solution spectrum for discontinuous approximations contains an infinite series of high frequency terms that localize toward the jump. Consequently, with a properly designed filter the high-pass component of the RK approximation can also be used as a high-pass error indicator at a shock. Therefore, it is necessary to determine appropriate filter limits for the RK approximation. That is to say, an appropriate basis order and support dilation must be determined for use in eq. 71 when shocks are to be detected. Numerical experiments were conducted in one- and two-dimensions to study the behavior of the two-scale decomposition as a function of the filtering RK shape function pass limit. As an example, an approximation of the function

$$u(x) = \begin{cases} 1 & 0 \leq x \leq 1 \\ 0 & 1 < x \leq 2 \end{cases} \qquad \text{eq. 74}$$

is shown in Figure 10. The approximation kernel was formed using a linear basis ($n = 1$). In Figure 10a the two-scale decomposition is shown with a constant filter kernel basis ($m = 0$) and filter kernel support $b = 2a$. The high-pass component of the approximation, $u^h_{high}(x)$, is localized to within two nodes of the discontinuity. Figure 10b shows the decomposition with a constant filter kernel basis, but with the filter kernel support increased to $b = 3a$. The high-pass component is still localized, but in this case is contained within three nodes of the discontinuity according to the increase in the filter kernel pass limit. The

results of additional studies followed similar and showed that with a single-order reduction in the degree of the filter kernel, $m = n - 1$, and filter support dilation $b = 2a$ or $b = 3a$, a sharp high-pass signal that is localized to the shock is consistently obtained.

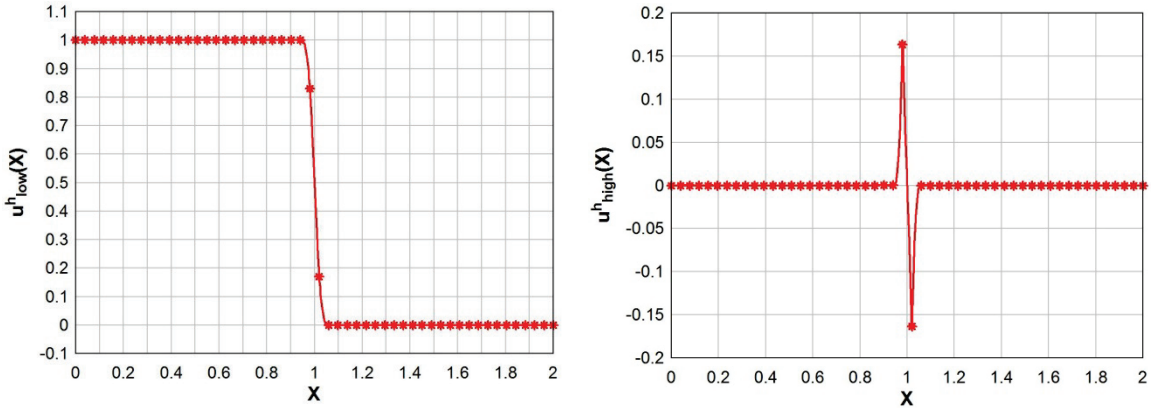

(a)

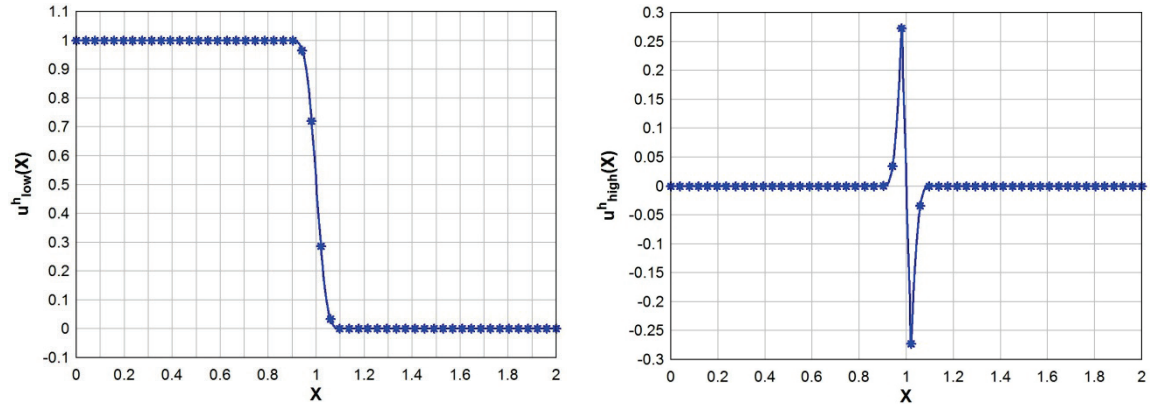

(b)

Figure 10. Two-scale RK spectral decomposition, a) filter kernel $m = 0$ and $b = 2a$, b) filter kernel $m = 0$ and $b = 3a$

Using the high-pass component of the RK approximation formed from an appropriately constructed two-scale decomposition, an automatic shock detection algorithm can be developed. In this work two approaches were considered. The first considers the high-pass component as a high-pass error and constructs a shock indicator based on relative error density. A measure of the global high-pass error is defined by the L_2 norm

$$e_{global}(t) = \left\| u^h(\boldsymbol{x},t) - u^h_{low}(\boldsymbol{x},t) \right\|_0 = \left\{ \int_\Omega \left[u^h(\boldsymbol{x},t) - u^h_{low}(\boldsymbol{x},t) \right]^2 \, d\Omega \right\}^{1/2} \quad \text{eq. 75}$$

so that the high-pass global error density is obtained

$$\bar{e}_{global}(t) = \frac{e_{global}(t)}{\int_\Omega d\Omega} \quad \text{eq. 76}$$

Similar local error measures, $\bar{e}_{local}(t)$, are defined for computational sub-domains that can be constructed in various ways (e.g., cell topology used for numerical integration). A relative local error density can be obtained

$$e_{rel} = \frac{\bar{e}_{local}(t)}{\bar{e}_{global}(t)} \quad \text{eq. 77}$$

which is utilized as an automatic shock detector based on limiting criterion for e_{rel} in this work. Another approach was developed herein where detection was based solely on the magnitude of the nodal high-pass error. This technique is similar to one used by Lee et al. [66] for adaptive refinement in stress concentration problems, and it minimizes computational cost by avoiding integration of the local and global error at each time step. Both approaches have been used successfully for automatic shock detection in this research

as will be shown below.

An example of using the RK spectral decomposition feature to detect a shock is shown in Figure 11. The non-linear Burgers' equation was used to simulate a shock with magnitude of 1.0 traveling in a two-dimensional domain from the origin at $x = 0, y = 0$ diagonally to the point $x = 2, y = 2$. The location of the shock at time $t = 0.6$ is shown Figure 11a. The high-pass component of the RK approximation at the same time is shown in Figure 11b, where the high-pass approximation is localized to the region in the immediate vicinity of the shock. The detection algorithm based on magnitude of the nodal high-pass error was used to automatically detect the transient shock, which is shown in Figure 11b as the larger white nodes. A detection constraint of $\left|u^h_{high}(\boldsymbol{x}, t)\right| > 0.03$ was used to automatically identify the shock region. In the transient calculation this technique accurately tracked the shock as it travelled through the problem domain.

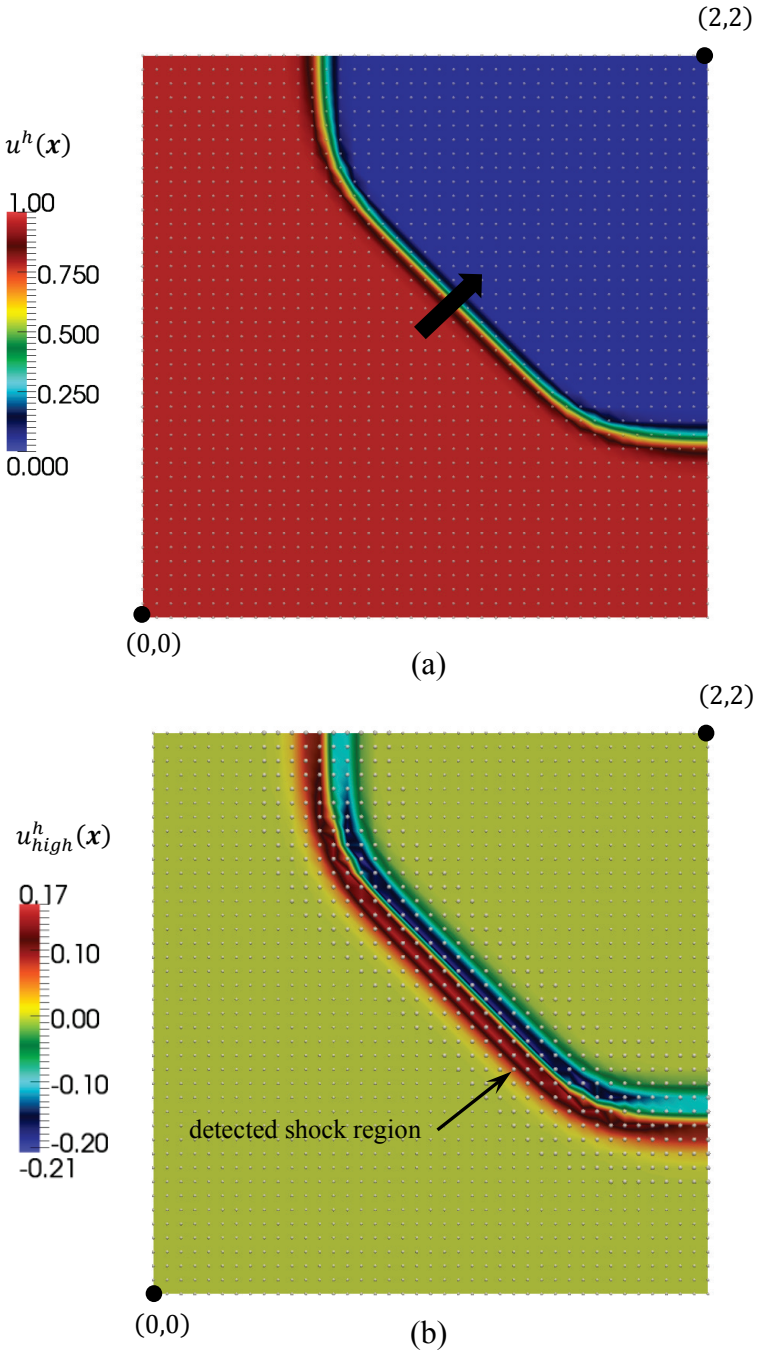

Figure 11. Shock detection algorithm applied to Burgers' equation a) shock location, and b) high-pass component of RK approximation at shock front

4.3 Weak form and stabilized conforming nodal integration

4.3.1 Weak form and Galerkin equation

Consider the following inviscid conservation equation in the multi-dimensional domain, Ω,

$$u(\boldsymbol{x},t)_{,t}+\boldsymbol{\nabla}\cdot\boldsymbol{F}\big(u(\boldsymbol{x},t)\big)=0 \qquad \text{eq. 78}$$

where $\boldsymbol{F}\big(u(\boldsymbol{x},t)\big)^T=\big[f\big(u(\boldsymbol{x},t)\big),g\big(u(\boldsymbol{x},t)\big),h\big(u(\boldsymbol{x},t)\big)\big]$ and $f\big(u(\boldsymbol{x},t)\big)$, $g\big(u(\boldsymbol{x},t)\big)$, and $h\big(u(\boldsymbol{x},t)\big)$ are analytical flux functions defined in the principal directions. The eq. 78 is shock forming in the presence of non-linear flux as defined by the physics of the problem. To construct the RKPM weak formulation a test function, $w(\boldsymbol{x},t)\in H_g^1$, is introduced to eq. 78, which is integrated over the domain, Ω, to obtain

$$\int_\Omega w(\boldsymbol{x},t)\big[u(\boldsymbol{x},t)_{,t}+\boldsymbol{\nabla}\cdot\boldsymbol{F}\big(u(\boldsymbol{x},t)\big)\big]\,d\Omega=0 \qquad \text{eq. 79}$$

Here integration by parts on the flux divergence term is avoided for the purpose of constructing the Riemann-enriched smoothed flux divergence, which is addressed in a later section. The Galerkin equation is obtained by introducing the approximation of the test and trial functions

$$\int_\Omega w^h(\boldsymbol{x},t)\left[u^h(\boldsymbol{x},t)_{,t}+\boldsymbol{\nabla}\cdot\boldsymbol{F}\Big(u^h(\boldsymbol{x},t)\Big)\right]\,d\Omega=0 \qquad \text{eq. 80}$$

where the approximated trial function is defined in eq. 68, and the approximated test function is defined similarly. The numerical solution of eq. 80 is prone to strong oscillation when

higher-order spatial approximations are introduced at the shock. To control these oscillations a correction is constructed according to the essential shock physics that will engender the formulation with an oscillation limiting feature.

4.3.2 Rankine-Hugoniot jump condition

A key ingredient of the essential shock physics is satisfaction of the Rankine-Hugoniot (R-H) jump condition at the shock. The jump condition is satisfied by the weak formulation of the governing equation in conservative form, which is shown by considering eq. 79 with integration over the arbitrary space-time domain, Υ (ref. Figure 12)

$$\int_{t=0}^{\infty}\int_{x=-\infty}^{\infty} w(x,t)\left[u(x,t)_{,t} + f\left(u(x,t)\right)_{,x}\right]\, dx\, dt = 0 \qquad \text{eq. 81}$$

Only one spatial dimension is considered for discussion. With the test function bounded according to the H_g^1 space, it is referred to as a compact test function with the properties $w(\infty,t) = w(-\infty,t) = w(x,\infty) = 0$. Further, with specified initial conditions over Υ the test function exhibits the property $w(x,0) = 0$. Now apply integration by parts to $\int_0^{\infty} w(x,t)u(x,t)_{,t}\ dt$ and $\int_{-\infty}^{\infty} w(x,t)f(u(x,t))_{,x}\ dx$ in eq. 81 to obtain

$$\int_0^{\infty} w(x,t)u(x,t)_{,t}\ dt = w(x,t)u(x,t)|_0^{\infty} - \int_0^{\infty} w(x,t)_{,t}\, u(x,t)\, dt \qquad \text{eq. 82}$$

$$= -\int_0^{\infty} w(x,t)_{,t}\, u(x,t)\, dt \qquad \text{eq. 83}$$

$$\int_{-\infty}^{\infty} w(x,t) f\big(u(x,t)\big)_{,x}\, dx = \int_{-\infty}^{\infty} w(x,t) f\big(u(x,t)\big) n_x\, d\Gamma - \int_{-\infty}^{\infty} w(x,t)_{,x}\, f\big(u(x,t)\big)\, dx \qquad \text{eq. 84}$$

$$= -\int_{-\infty}^{\infty} w(x,t)_{,x}\, f\big(u(x,t)\big)\, dx \qquad \text{eq. 85}$$

which is substituted back into eq. 81 to obtain

$$\int_{t=0}^{\infty} \int_{x=-\infty}^{\infty} w(x,t)_{,t}\, u(x,t) + w(x,t)_{,x}\, f\big(u(x,t)\big)\, dx\ dt\ = 0 \qquad \text{eq. 86}$$

In the presence of a shock, a discontinuity forms in Υ along the boundary Γ_s such that the space-time domain is divided into two smooth sub-domains, Υ^- and Υ^+. Normal to the discontinuity is $\mathbf{n} = [n_x,\ n_t]$, which is a function of space and time as shown in Figure 12. Solutions to the left and right of the discontinuity are $u^-(x,t)$ and $u^+(x,t)$, respectively. Considering the discontinuity, eq. 86 can be written as

$$\int_{\Upsilon^-} w(x,t)_{,t}\, u(x,t) + w(x,t)_{,x}\, f\big(u(x,t)\big)\, dx\, dt + \int_{\Upsilon^+} w(x,t)_{,t}\, u(x,t) + w(x,t)_{,x}\, f\big(u(x,t)\big)\, dx\, dt = 0 \qquad \text{eq. 87}$$

Again using integration by parts and the divergence theorem and making use of the weak form expression of eq. 79 applied to the smooth sub-domains, eq. 87 is transformed to the contour integral over the discontinuity

$$\int_{\Gamma_s} w(x,t)\big[u^-(x,t) n_t^- + f\big(u^-(x,t)\big) n_x^-\big]\, d\Gamma = -\int_{\Gamma_s} w(x,t)\big[u^+(x,t) n_t^+ + f\big(u^+(x,t)\big) n_x^+\big]\, d\Gamma \qquad \text{eq. 88}$$

Due to arbitrariness of the test function and considering that $\mathbf{n}^- = -\mathbf{n}^+$, eq. 88 implies

$$u^-(x,t) n_t + f\big(u^-(x,t)\big) n_x = u^+(x,t) n_t + f\big(u^+(x,t)\big) n_x \qquad \text{eq. 89}$$

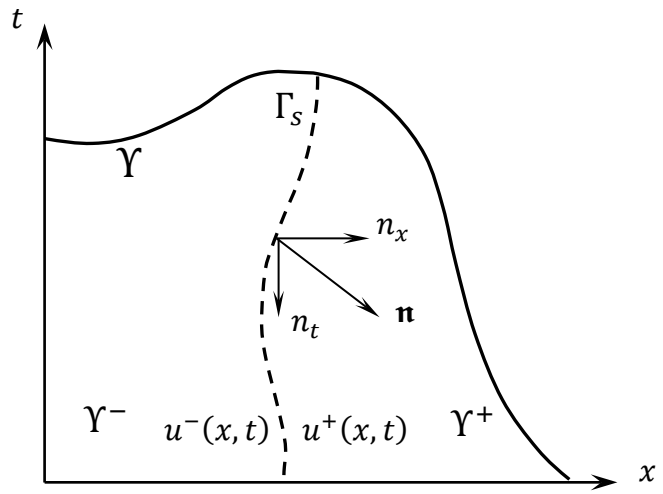

Figure 12. Arbitrary space-time domain, ϒ

The shock velocity, ξ, is related to $\mathbf{n}$ by $\xi = dx/dt = -n_t/n_x$, which is used with eq. 89 to obtain

$$\xi = \frac{f\left(u^-(x,t)\right) - f\left(u^+(x,t)\right)}{u^-(x,t) - u^+(x,t)} \qquad \text{eq. 90}$$

The Rankine-Hugoniot jump equation is given by eq. 90, and shows that the R-H jump condition is naturally embedded in the weak form of eq. 79.

4.3.3 Stabilized conforming nodal integration

Chen et al. [27, 28] introduced a type of stabilized conforming nodal integration for stable direct nodal integration of the weak form that achieves optimal convergence with linear basis. This method avoids the loss of accuracy associated with Gauss integration in a meshfree framework and stabilizes direct nodal integration to avoid spurious modes that arise from integration of the nodal derivatives. In this work SCNI is further used as a framework

to construct a locally corrected flux divergence operator that is flux conserving and embeds the essential shock physics for entropy production into the meshfree formulation.

To build the SCNI framework, first consider an arbitrary discretization of the domain Ω with a set of np nodes as shown in Figure 13. The domain is tessellated to construct a set of conforming integration cells that are centered on the nodes; Voronoi cell tessellation can be used to construct this type of domain sub-division. The integration cell associated with the I^{th} node is Ω_I, which has a boundary Γ_I composed of a set of line segments with outward normal $\boldsymbol{n}$. The integration cells are conforming so that $\cup\, \Omega_{I=1\ldots np} = \Omega$ and $\cap\, \Omega_{I=1\ldots np} = \{\,\}$.

In the SCNI framework the gradient at the node is approximated using a smoothed gradient operator, which can be defined in a general form as

$$\boldsymbol{\nabla}\varsigma(\boldsymbol{x},t)|_{\boldsymbol{x}_I} \approx \int_{\Omega_I} \boldsymbol{\nabla}\varsigma(\boldsymbol{x},t)\, \varphi(\boldsymbol{x};\boldsymbol{x}-\boldsymbol{x}_I)\, d\Omega \equiv \widetilde{\boldsymbol{\nabla}}\varsigma_I(t) \qquad \text{eq. 91}$$

where $\widetilde{\boldsymbol{\nabla}}\varsigma_I(t)$ is the smoothed gradient of $\varsigma(\boldsymbol{x},t)|_{\boldsymbol{x}_I}$ and $\varsigma(\boldsymbol{x},t)$ is a sufficiently differentiable function defined in Ω_I. The kernel function $\varphi(\boldsymbol{x};\boldsymbol{x}-\boldsymbol{x}_I)$ is defined according to the desired characteristics of the gradient approximation. If the kernel function is constant over Ω_I, then the divergence theorem transforms the smoothed gradient operation to the contour integral

$$\widetilde{\boldsymbol{\nabla}}\varsigma_I(t) = \int_{\Gamma_I} \varsigma(\boldsymbol{x},t)\varphi(\boldsymbol{x};\boldsymbol{x}-\boldsymbol{x}_I)\, \boldsymbol{n}\, d\Gamma \qquad \text{eq. 92}$$

where $\boldsymbol{n}$ is the outward normal to Γ_I; eq. 92 can be evaluated using any desired numerical integration technique. By eq. 92 the smoothed gradient approximation requires the evaluation of $\varsigma(\boldsymbol{x},t)$ over Γ_I, and not its derivative, which is an appealing attribute of this technique.

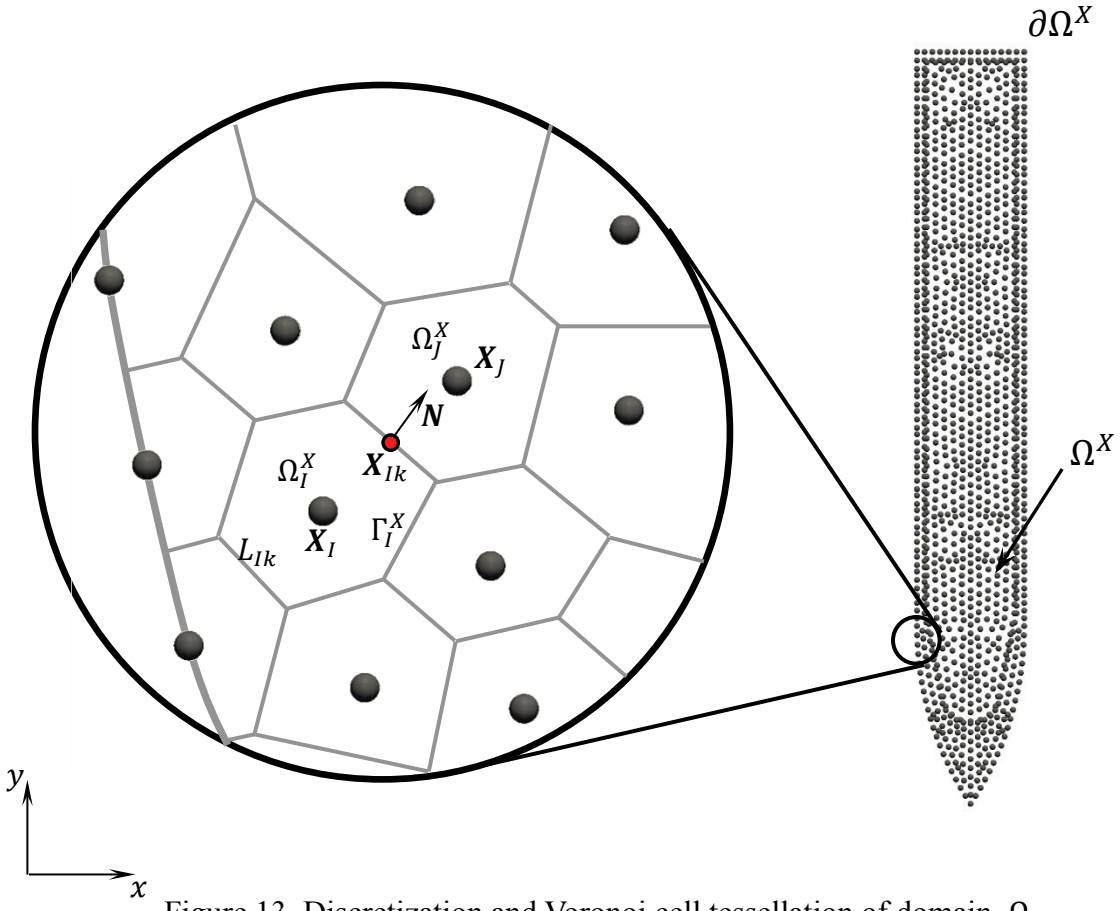

Figure 13. Discretization and Voronoi cell tessellation of domain, Ω

4.4 Smoothed flux divergence with local Riemann enrichment

4.4.1 Smoothed flux divergence

In the proposed formulation the weak form is integrated using SCNI, which engenders it with the benefits of this integration technique. To utilize SCNI a flux divergence approximation is introduced, similar to the smoothed gradient approximation in eq. 91; this is referred to as the smoothed flux divergence (SFD). Under the SCNI framework the SFD will

be locally enriched at the shock to enforce the entropy-related shock physics and ensure the physically correct shock propagation. Consider the flux divergence term in eq. 80 and construct a smoothed flux divergence using the approximation

$$\boldsymbol{\nabla}\cdot\boldsymbol{F}\left(u^h(\boldsymbol{x},t)\right)\Big|_{\boldsymbol{x}_I} \approx \int_{\Omega_I}\boldsymbol{\nabla}\cdot\boldsymbol{F}\left(u^h(\boldsymbol{x},t)\right)\varphi(\boldsymbol{x};\boldsymbol{x}-\boldsymbol{x}_I)\,d\Omega \equiv \widetilde{\boldsymbol{\nabla}}\cdot\boldsymbol{F}_I^h(t) \qquad \text{eq. 93}$$

A piecewise constant kernel is introduced to the approximation

$$\varphi(\boldsymbol{x};\boldsymbol{x}-\boldsymbol{x}_I)=\begin{cases}1/V_I & \boldsymbol{x}\in\Omega_I\\ 0 & otherwise\end{cases} \qquad \text{eq. 94}$$

where V_I is the volume of Ω_I. Using the divergence theorem with the piecewise constant kernel definition, eq. 93 is transformed to

$$\widetilde{\boldsymbol{\nabla}}\cdot\boldsymbol{F}_I^h(t)=\frac{1}{V_I}\int_{\Gamma_I}\boldsymbol{F}\left(u^h(\boldsymbol{x},t)\right)\cdot\boldsymbol{n}\,d\Gamma \qquad \text{eq. 95}$$

where $\widetilde{\boldsymbol{\nabla}}\cdot\boldsymbol{F}_I^h(t)$ is the SFD.

This formulation is flux conserving when a) the SFD in eq. 95 is computed on an underlying cell structure that is conforming, and b) the numerical flux calculation on the integration cell boundaries is consistent for the adjacent cells. To show this, eq. 95 is transformed back to a domain integral

$$\widetilde{\boldsymbol{\nabla}}\cdot\boldsymbol{F}_I^h(t)=\frac{1}{V_I}\int_{\Omega_I}\boldsymbol{\nabla}\cdot\boldsymbol{F}\left(u^h(\boldsymbol{x},t)\right)\,d\Omega \qquad \text{eq. 96}$$

If according to the first requirement the sub-domains, Ω_I, are conforming so that $\cup\ \Omega_{I=1\ldots np}=\Omega$ and for $I\neq J$, then we have

$$\sum_{I=1}^{np} \int_{\Gamma_I/\partial\Omega} \boldsymbol{F}\left(u^h(\boldsymbol{x},t)\right) \cdot \boldsymbol{n}\ d\Gamma = 0 \qquad \text{eq. 97}$$

This yields

$$\sum_{I=1}^{np} \int_{\Omega_I} \boldsymbol{\nabla} \cdot \boldsymbol{F}\left(u^h(\boldsymbol{x},t)\right)\ d\Omega = \sum_{I=1}^{np} \int_{\Gamma_I} \boldsymbol{F}\left(u^h(\boldsymbol{x},t)\right) \cdot \boldsymbol{n}\, d\Gamma \qquad \text{eq. 98}$$

$$\sum_{I=1}^{np} \int_{\Gamma_I/\partial\Omega} \boldsymbol{F}\left(u^h(\boldsymbol{x},t)\right) \cdot \boldsymbol{n}\ d\Gamma + \int_{\partial\Omega} \boldsymbol{F}\left(u^h(\boldsymbol{x},t)\right) \cdot \boldsymbol{n}\, d\Gamma = \int_{\partial\Omega} \boldsymbol{F}\left(u^h(\boldsymbol{x},t)\right) \cdot \boldsymbol{n}\, d\Gamma = \int_{\Omega} \boldsymbol{\nabla} \cdot \boldsymbol{F}\left(u^h(\boldsymbol{x},t)\right)\ d\Omega \qquad \text{eq. 99}$$

Now consider Figure 13 where the boundary between sub-domains Ω_I and Ω_J is the line segment L_{IJ}. The contour integral along this line segment with respect to the sub-domain Ω_I is

$$\left(\int_{\mathrm{L}_{IJ}} \boldsymbol{F}\left(u^h(\boldsymbol{x},t)\right) \cdot \boldsymbol{n}\ d\Gamma\right)^{[I]} \qquad \text{eq. 100}$$

where $(\cdots\cdots)^{[I]}$ implies evaluation of the contour integral when approaching the boundary from Ω_I. Similarly, the contour integral along L_{IJ} when approaching the boundary from Ω_J is

$$\left(\int_{\mathrm{L}_{IJ}} \boldsymbol{F}\left(u^h(\boldsymbol{x},t)\right) \cdot \boldsymbol{n}\ d\Gamma\right)^{[J]} \qquad \text{eq. 101}$$

Using $\boldsymbol{n}^I = -\boldsymbol{n}^J$, the following holds as long as the second requirement for consistency in the numerical flux is satisfied, i.e., $\left(\boldsymbol{F}\left(u^h(\boldsymbol{x},t)\right)\right)^{[I]} = \left(\boldsymbol{F}\left(u^h(\boldsymbol{x},t)\right)\right)^{[J]}$

$$\left(\int_{\mathrm{L}_{IJ}} \boldsymbol{F}\left(u^h(\boldsymbol{x},t)\right) \cdot \boldsymbol{n}\ d\Gamma\right)^{[I]} = -\left(\int_{\mathrm{L}_{IJ}} \boldsymbol{F}\left(u^h(\boldsymbol{x},t)\right) \cdot \boldsymbol{n}\ d\Gamma\right)^{[J]} \qquad \text{eq. 102}$$

If the condition in eq. 102 holds true for all Γ_I, then flux is conserved.

For numerical implementation, the SFD in eq. 95 is evaluated using the SCNI integration cell topology shown in Figure 14a. The boundary, Γ_I, is composed of a set of line segments $\mathbb{L}_I = \{L_{Ik}\}_{k=1}^{s}$ where s is the number of sides of Γ_I, with the length, midpoint and outward normal of segment L_{Ik} denoted as l_{Ik}, $\boldsymbol{x}_{Ik}$ and $\boldsymbol{n}_{Ik}$, respectively. Newton-Cotes quadrature is used to numerically integrate eq. 95, so that

$$\widetilde{\boldsymbol{\nabla}} \cdot \boldsymbol{F}_I^h(t) = (1/V_I) \sum_{k=1}^{s} \boldsymbol{F}\Big(u^h(\boldsymbol{x},t)\Big)\Big|_{\boldsymbol{x}_{Ik}} \cdot \boldsymbol{n}_{Ik} l_{Ik} \qquad \text{eq. 103}$$

In eq. 103 the analytical flux definition is required, which is defined for the particular conservation problem being studied. As examples of constructing the SFD, consider two model problems and their analytical flux definitions: the linear advection equation and the non-linear inviscid Burgers' equation. These same model problems will be used for numerical examples later. The flux definitions and corresponding smoothed flux divergence expressions are as follows.

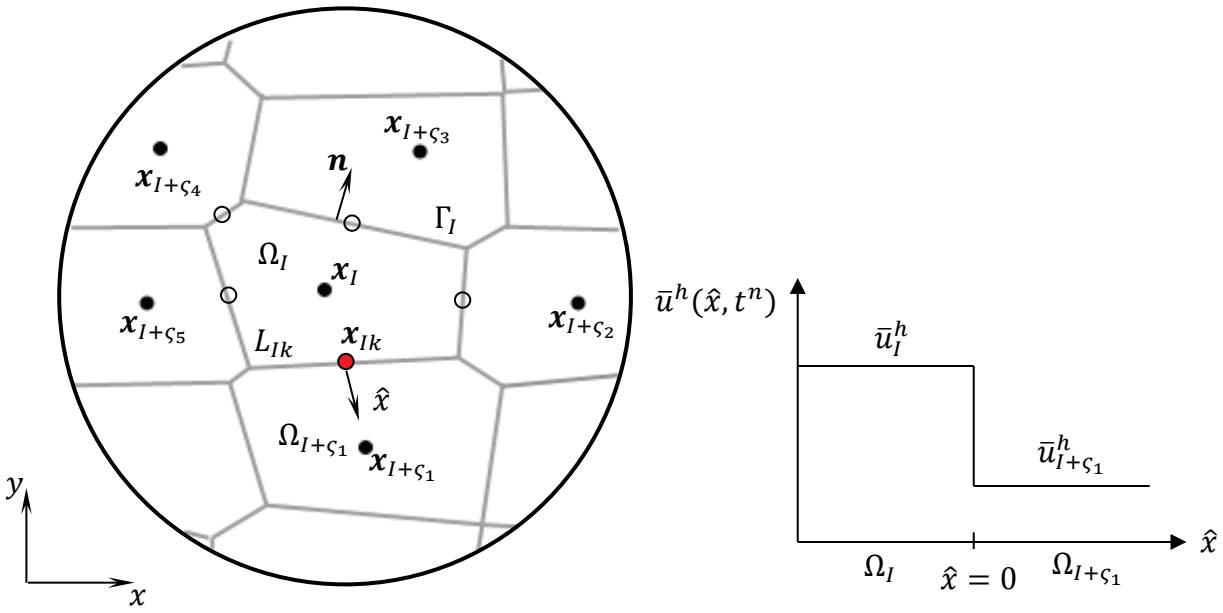

(a) (b)

Figure 14. (a) SCNI integration cell topology and b) local Riemann problem at shock

Linear advection with constant coefficients

Assuming a two-dimensional domain, the analytical flux definition for linear advection with constant coefficients is

$$\boldsymbol{F}\big(u(\boldsymbol{x},t)\big) = \begin{bmatrix}\alpha\, u(\boldsymbol{x},t)\\ \beta\, u(\boldsymbol{x},t)\end{bmatrix} \qquad \text{eq. 104}$$

where α and β are advection constants. Substituting into eq. 103 gives

$$\widetilde{\boldsymbol{\nabla}} \cdot \boldsymbol{F}_I^h(t) = (1/A_I)\sum_{k=1}^{s}\big[\,\alpha\, u^h(\boldsymbol{x},t)|_{\boldsymbol{x}_{Ik}} n_{xIk}\, l_{Ik} + \beta\, u^h(\boldsymbol{x},t)|_{\boldsymbol{x}_{Ik}} n_{yIk}\, l_{Ik}\big] \qquad \text{eq. 105}$$

Introducing the spatial approximation from eq. 58 gives

$$\widetilde{\boldsymbol{\nabla}} \cdot \boldsymbol{F}_I^h(t) =$$
$$(1/A_I) \sum_{k=1}^{s} \left[\alpha \left(\sum_{J=1}^{np} \Psi_J(\boldsymbol{x}_{Ik}) d_J(t) \right) n_{xIk}\, l_{Ik} + \beta \left(\sum_{J=1}^{np} \Psi_J(\boldsymbol{x}_{Ik}) d_J(t) \right) n_{yIk}\, l_{Ik} \right] \quad \text{eq. 106}$$

$$= (1/A_I) \sum_{J=1}^{np} \sum_{k=1}^{s} \Psi_J(\boldsymbol{x}_{Ik}) \left(\alpha\, n_{xIk}\, l_{Ik} + \beta n_{yIk} l_{Ik} \right) d_J(t) \quad \text{eq. 107}$$

Let

$$b_J^I = (1/A_I) \sum_{k=1}^{s} \Psi_J(\boldsymbol{x}_{Ik}) \left(\alpha\, n_{xIk}\, l_{Ik} + \beta n_{yIk} l_{Ik} \right) \quad \text{eq. 108}$$

so that the smoothed flux divergence for the linear advection equation at $\boldsymbol{x}_I$ is

$$\widetilde{\boldsymbol{\nabla}} \cdot \boldsymbol{F}_I^h(t) = \sum_{J=1}^{np} b_J^I\, d_J(t) \quad \text{eq. 109}$$

Non-linear Burgers' equation

Again assuming a two-dimensional domain, the analytical flux definition for Burgers' equation is

$$\boldsymbol{F}\left(u(\boldsymbol{x},t)\right) = \begin{bmatrix} 0.5 \left(u(\boldsymbol{x},t)\right)^2 \\ 0.5 \left(u(\boldsymbol{x},t)\right)^2 \end{bmatrix} \quad \text{eq. 110}$$

The flux in eq. 110 presents a complexity due to the requirement for an approximation of u^2. To address this, consider that

$$\boldsymbol{\nabla} \cdot \boldsymbol{F}\left(u^h(\boldsymbol{x},t)\right) = \frac{\partial F_i}{\partial u^h} \frac{\partial u^h}{\partial x_i} \quad \text{eq. 111}$$

so that for Burgers' equation

$$\boldsymbol{\nabla} \cdot \boldsymbol{F}\left(u^h(\boldsymbol{x},t)\right) = u^h(\boldsymbol{x},t) u^h(\boldsymbol{x},t)_{,x} + u^h(\boldsymbol{x},t) u^h(\boldsymbol{x},t)_{,y} \quad \text{eq. 112}$$

$$= u^h(\boldsymbol{x},t)[\mathbf{I}\cdot\boldsymbol{\nabla}u^h(\boldsymbol{x},t)] \qquad \text{eq. 113}$$

where $\mathbf{I}^{\mathbf{T}} = [1 \quad 1]$. Considering a discrete numerical solution in space and time, the coefficient $u^h(\boldsymbol{x},t)$ in eq. 113 can be approximated by the discrete solution at the previous time step, which is denoted as ζ_I. Introducing this approximation along with a smoothed gradient operator gives

$$\tilde{\boldsymbol{\nabla}}\cdot\boldsymbol{F}_I^h(t) = \zeta_I\left[\mathbf{I}\cdot\tilde{\boldsymbol{\nabla}}u_I^h(t)\right] \qquad \text{eq. 114}$$

where $\tilde{\boldsymbol{\nabla}}u_I^h(t)$ is defined according to eq. 92 using the piecewise constant kernel defined in eq. 94. Using Newton-Cotes quadrature for numerical integration gives

$$\tilde{\boldsymbol{\nabla}}u_I^h(t) = (1/A_I)\ \textstyle\sum_{k=1}^{s} u^h(\boldsymbol{x},t)|_{\boldsymbol{x}_{Ik}}\boldsymbol{n}_{Ik}l_{Ik} \qquad \text{eq. 115}$$

$$= (1/A_I)\ \textstyle\sum_{k=1}^{s}\left(\sum_{J=1}^{np}\Psi_J(\boldsymbol{x}_{Ik})d_J(t)\right)\boldsymbol{n}_{Ik}l_{Ik} \qquad \text{eq. 116}$$

where the spatial approximation from eq. 58 was introduced. Substituting eq. 116 into eq. 114 gives

$$\tilde{\boldsymbol{\nabla}}\cdot\boldsymbol{F}_I^h(t) = (\zeta_I/A_I)\left[\textstyle\sum_{J=1}^{np}\sum_{k=1}^{s}\Psi_J(\boldsymbol{x}_{Ik})\left(n_{xIk}l_{Ik}+n_{yIk}l_{Ik}\right)d_J(t)\right] \qquad \text{eq. 117}$$

Let

$$b_J^I = (\zeta_I/A_I)\textstyle\sum_{k=1}^{s}\Psi_J(\boldsymbol{x}_{Ik})\left(\ n_{xIk}\ l_{Ik}+n_{yIk}l_{Ik}\right) \qquad \text{eq. 118}$$

The smoothed flux divergence for Burgers' equation at $\boldsymbol{x}_I$ is obtained by substituting eq. 118

into eq. 109.

4.4.2 Riemann-enriched boundary flux

To enforce the essential physics corresponding with the entropy production constraint and to control Gibbs phenomenon at the jump, a correction of the meshfree solution is required at the shock. The correction is formed using a Godunov-type approach, where the smoothed flux divergence is enriched in the local shock region with a Riemann solution. The solution of the Riemann problem inherently satisfies the entropy production constraint and therefore guarantees the physically correct shock propagation in .the numerical solution. The enrichment is limited to the shock region according to the shock detection algorithm, and is therefore referred to as a local Riemann enrichment of the SFD in this work.

The Riemann problem is a special initial value problem (IVP) constructed in a domain, Ω, where initial conditions are piecewise constant over a series of conforming sub-domains, $\{\Omega_I\}_{I=1}^{np}$, due to the use of lower order approximation to limit the oscillation. These piecewise constant initial conditions (ICs) create numerical discontinuities at the sub-domain boundaries, which are viewed as a local shock problem in this research. As a consequence, the updated solution at the sub-domain boundary can be determined in straightforward manner using characteristic projections. The important point is that the physically correct shock or rarefaction solution is guaranteed from analysis of the characteristic projections, and as a result the solution naturally enforces the entropy production constraint. If the piecewise constant smoothed flux divergence in each cell is reconstructed at each time step, then in the

detected shock region the Riemann solution can be used to determine $\boldsymbol{F}\left(u^h(\boldsymbol{x},t)\right)\Big|_{\boldsymbol{x}_{Ik}}$ in eq. 103 so that the smoothed flux divergence is locally enriched. Furthermore, since the Riemann problem can be naturally constructed on the SCNI cell topology it is easily incorporated into the meshfree framework.

To construct a general Riemann problem, consider the piecewise constant ICs, $u(x,t^n)$, shown in Figure 15a. The ICs are discontinuous at the sub-domain boundary, x^*, which is located at the junction of Ω_I and Ω_J.

$$u(x,t^n)=\begin{cases}u_I & x\in\Omega_I\\ u_J & x\in\Omega_J\end{cases} \qquad \text{eq. 119}$$

The characteristic speed of the wavelet projections is

$$\lambda\big(u(x,t^n)\big)=\frac{\partial f\big(u(x,t^n)\big)}{\partial u(x,t^n)} \qquad \text{eq. 120}$$

where $f\big(u(x,t)\big)$ is the analytical flux function. These projections or characteristic lines are shown in Figure 15b and Figure 15c, where each characteristic line describes how $u(x,t^n)$ projects in space and time for $t>t^n$. If, as shown in Figure 15b, the characteristics converge as a result of $\lambda(u_I)>\lambda\big(u_J\big)$ then a shock forms and the discontinuity propagates with a velocity, ξ. The Riemann shock solution for $x\in\Omega_I\cup\Omega_J$ is

$$u(x,t)=\begin{cases}u_I & (x-x^*)/(t-t^n)<\xi\\ u_J & (x-x^*)/(t-t^n)>\xi\end{cases} \qquad \text{eq. 121}$$

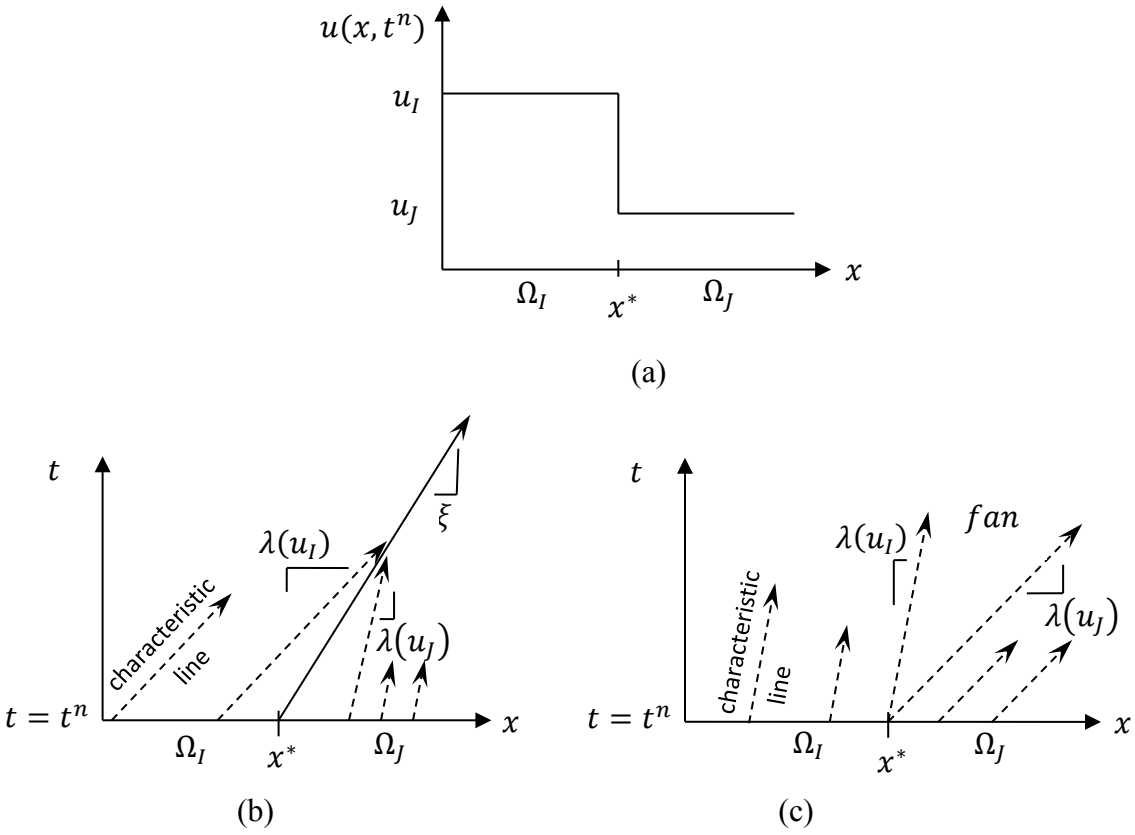

Figure 15. General Riemann IVP, a) piecewise constant initial conditions, b) shock due to converging characteristics, and c) rarefaction due to diverging characteristics

which is derived directly from the characteristic projections. The solution at the sub-domain boundary is found by evaluating at $x = x^*$. If, as shown in Figure 15c, the characteristics diverge as a result of $\lambda(u_I) < \lambda(u_J)$ then a rarefaction forms and the discontinuity degenerates into a fan. The Riemann rarefaction solution is

$$u(x,t) = \begin{cases} u_I & (x-x^*)/(t-t^n) \le \lambda(u_I) \\ u((x-x^*)/(t-t^n)) & \lambda(u_I) < (x-x^*)/(t-t^n) < \lambda(u_J) \\ u_J & (x-x^*)/(t-t^n) \ge \lambda(u_J) \end{cases} \quad \text{eq. 122}$$

The solution at the boundary is again found by substituting $x = x^*$. In eq. 122, $u((x-x^*)/(t-t^n))$ is the general solution inside of the fan, where $(x-x^*)/(t-t^n)$ is the slope of characteristic lines inside of the fan. It can be shown for that for convex flux functions, the expression for $u((x-x^*)/(t-t^n))$ is found by solving $\partial f\big(u(x,t)\big)/\partial u(x,t) = (x-x^*)/(t-t^n)$, where the analytical flux function is defined according to the problem being considered [103].

To capture shocks in the meshfree formulation, the local Riemann problem is constructed on boundary segments of each SCNI integration cell in the shock region. Consider an integration cell, Ω_I, as previously described in Figure 14a, which is now assumed to be located near a shock. The cell topology is described in section 4.4.1, where Γ_I is composed of a set of line segments, $\mathbb{L}_I$. The set of nodes whose cell boundaries intersect with $\mathbb{L}_I$ is $\mathbb{X}_I = \{\boldsymbol{x}_{I+\varsigma_k} |\, 0 < I + \varsigma_k \le np,\ k = 1 \ldots s, \varsigma_k \ne 0\}$. To construct the piecewise constant initial conditions for the Riemann problem, a cell-averaged solution in Ω_I at time $t = t^n$ is defined

$$\bar{u}_I^h\big|_{t^n} = (1/V_I) \int_{\Omega_I} u^h(\boldsymbol{x}, t^n)\, d\Omega \quad \text{eq. 123}$$

Similar cell-averaged solutions are defined for each of the adjoining cells, which are denoted

as $\bar{u}_{I+\varsigma_k}^h\big|_{t^n}$. To evaluate the smoothed flux divergence in eq. 103, the Riemann solution is sought at the midpoint, $\boldsymbol{x}_{Ik}$, of each boundary segment, L_{Ik}. A variety of techniques can be used to construct the local Riemann problem, such as dimensional splitting [117], unsplit finite volume approaches [117], or a rotated Riemann problem aligned with dominant flow features [118]. Regardless of the specific solution technique, the local Riemann problem for each boundary segment is constructed along a local coordinate axis, $\hat{x}$, with its origin located at the midpoint, $\boldsymbol{x}_{Ik}$. An example of the local Riemann problem centered on $\boldsymbol{x}_{Ik}$ is shown in Figure 14b. The solution is sought at the integration cell boundary, which coincides with $\hat{x} = 0$ in the local coordinate system. Referencing the general Riemann solutions in eq. 121 and eq. 122, the local Riemann solution at the midpoint, $u^{RP}(\boldsymbol{x}_{Ik}, t^n)$, is defined as

for $\lambda(\bar{u}_I^h) > \lambda(\bar{u}_{I+\varsigma_1}^h)$ (shock):

$$u^{RP}(\boldsymbol{x}_{Ik}, t^n) = \begin{cases} \bar{u}_I^h\big|_{t^n} & 0 < \xi \\ \bar{u}_{I+\varsigma_k}^h\big|_{t^n} & 0 > \xi \end{cases} \qquad \text{eq. 124}$$

for $\lambda(\bar{u}_I^h) < \lambda(\bar{u}_{I+\varsigma_k}^h)$ (rarefaction):

$$u^{RP}(\boldsymbol{x}_{Ik}, t^n) = \begin{cases} \bar{u}_I^h\big|_{t^n} & 0 \le \lambda\left(\bar{u}_I^h\right) \\ u|_{t^n} & \lambda\left(\bar{u}_I^h\right) < 0 < \lambda\left(\bar{u}_{I+\varsigma_k}^h\right) \\ \bar{u}_{I+\varsigma_k}^h\big|_{t^n} & 0 \ge \lambda\left(\bar{u}_{I+\varsigma_k}^h\right) \end{cases} \qquad \text{eq. 125}$$

Introducing this Riemann solution to eq. 103 gives the locally enriched smoothed flux divergence

$$\widetilde{\boldsymbol{\nabla}} \cdot \boldsymbol{F}_I^h(t) = (1/V_I) \sum_{k=1}^{s} \boldsymbol{F}\left(u^{RP}(\boldsymbol{x}_{Ik}, t^n)\right) \cdot \boldsymbol{n}_{Ik}\, l_{Ik} \qquad \text{eq. 126}$$

where $\boldsymbol{F}\left(u^{RP}(\boldsymbol{x}_{Ik}, t^n)\right)$ is referred to as the Riemann-enriched boundary flux.

4.5 Flux-corrected velocity

The smoothed flux divergence was constructed under the SCNI framework in eq. 103, and a local Riemann enrichment was introduced in eq. 126 to enforce the entropy-correct shock solution. It is now desired to adaptively apply the Riemann enrichment at the shock, and couple with that enrichment a mechanism to control Gibbs phenomenon oscillations at the jump. These objectives are achieved in the proposed formulation through the construction of a Godunov-type of flux-corrected velocity. To construct the flux-corrected velocity, the governing eq. 78 is integrated over the domain $\Omega_I \times [t^n, t^{n+1}]$ to obtain

$$\int_{\Omega_I} \int_{t^n}^{t^{n+1}} \left(u(\boldsymbol{x}, t)_{,t} + \boldsymbol{\nabla} \cdot \boldsymbol{F}\left(u(\boldsymbol{x}, t)\right)\right) dt \, d\Omega = 0 \qquad \text{eq. 127}$$

Integrating the time derivative gives

$$\int_{\Omega_I} \left(u(\boldsymbol{x}, t^{n+1}) - u(\boldsymbol{x}, t^n)\right) d\Omega + \int_{t^n}^{t^{n+1}} \int_{\Omega_I} \boldsymbol{\nabla} \cdot \boldsymbol{F}\left(u(\boldsymbol{x}, t)\right) d\Omega \, dt = 0 \qquad \text{eq. 128}$$

Considering the domain integral in eq. 128, introduce the meshfree approximation at $\boldsymbol{x}_I$ as an approximation of the cell-averaged solution

$$u^h(\boldsymbol{x}, t^n)|_{\boldsymbol{x}_I} \approx (1/V_I) \int_{\Omega_I} u(\boldsymbol{x}, t^n) \, d\Omega \rightarrow \int_{\Omega_I} u(\boldsymbol{x}, t^n) \, d\Omega \approx \mathrm{V}_I u^h(\boldsymbol{x}, t^n)|_{\boldsymbol{x}_I} \qquad \text{eq. 129}$$

and denote $\mathrm{V}_I u_I^n \equiv \mathrm{V}_I u^h(\boldsymbol{x}, t^n)|_{\boldsymbol{x}_I}$. Introducing the approximation from eq. 129 into eq. 128 gives

$$\mathrm{V}_I u_I^{n+1} - \mathrm{V}_I u_I^n + \int_{t^n}^{t^{n+1}} \int_{\Omega_I} \boldsymbol{\nabla} \cdot \boldsymbol{F}\Big(u^h(\boldsymbol{x}, t)\Big)\, d\Omega\, dt = 0 \qquad \text{eq. 130}$$

where the meshfree approximation was also introduced to the flux divergence term. Now consider the domain integral in eq. 130 and introduce the smoothed flux divergence from eq. 95, the Riemann-enriched boundary flux from eq. 126, and with employment of explicit time integration we have

$$\mathrm{V}_I u_I^{n+1} - \mathrm{V}_I u_I^n + \Delta t\, \gamma_I^n = 0 \;\; \rightarrow \;\; u_I^{n+1} = u_I^n - \Delta t\, \gamma_I^n / V_I \qquad \text{eq. 131}$$

where

$$\gamma_I^n = V_I \widetilde{\boldsymbol{\nabla}} \cdot \boldsymbol{F}_I^h(t) = \sum_{k=1}^{s} \boldsymbol{F}\Big(u^{RP}(\boldsymbol{x}_{Ik}, t^n)\Big) \cdot \boldsymbol{n}_{Ik}\, l_{Ik} \qquad \text{eq. 132}$$

The eq. 131 is equivalent to the Godunov evolution equation, where the solution is projected forward in time using the flux-corrected velocity, γ_I^n / V_I, which is a first order oscillation limiter embedded with the Riemann-enriched smoothed flux divergence. To adaptively apply the flux-corrected velocity at the shock front, the temporal evolution equation is constructed

$$d_I^{n+1} = d_I^n + \Delta t\big\{(1-\alpha)\dot{d}_I^n + \alpha \dot{d}_I^{n+1} + \vartheta_I\big[(\alpha-1)\dot{d}_I^n - \alpha \dot{d}_I^{n+1} - \gamma_I^n / V_I\big)\big]\big\} \qquad \text{eq. 133}$$

where $d_I(t)$ is the nodal coefficient of the RK approximation in eq. 58, α is the generalized Trapezoidal rule parameter and

$$\vartheta_I = \begin{cases} 1 & \boldsymbol{x}_I \in \textit{detected shock region} \\ 0 & \textit{otherwise} \end{cases} \qquad \text{eq. 134}$$

Here ϑ_I controls the adaptive flux-corrected velocity at the shock according to the RK shock

detection algorithm. This flux-corrected velocity provides oscillation control at the shock front, enforces the essential shock physics, and maintains RKPM higher-order accuracy away from the shock region.

4.6 Numerical examples

In this section several numerical examples are provided to verify performance of the proposed formulation. Each example solves the conservation equation

$$u(\boldsymbol{x},t)_{,t}+\boldsymbol{\nabla}\cdot\boldsymbol{F}\big(u(\boldsymbol{x},t)\big)=0 \qquad \text{eq. 135}$$

with the flux defined according to the selected model problem. In the following examples, the flux divergence is calculated based on the proposed SFD technique, while the correction of the velocity field is invoked only when shocks are detected. The first example solves the linear advection equation using the smoothed flux divergence from eq. 103. Plane wave propagation in a two-dimensional domain is modeled to verify convergence for smooth wave propagation and confirm higher-order accuracy for smooth solutions in accordance with the adaptive flux correction. The second example solves the non-linear Burgers' equation with jump conditions selected to degenerate into a rarefaction wave. The corrected and uncorrected RKPM solutions are compared to a fine-scale Lax-Friedrichs reference solution to evaluate performance for fan formation. In the third example Burgers' equation is solved with smooth initial conditions that evolve into a plane shock wave. This example evaluates performance of the automatic shock detection algorithm and performance of the flux-

corrected velocity for adaptive limiting of solution oscillation in the presence of shock formation. The uncorrected RKPM, corrected RKPM, and full Godunov solutions are compared to a fine-scale Lax-Friedrichs reference solution to evaluate accuracy improvement. The last example solves Burgers' equation for a two-dimensional shock wave propagation that travels skew to the principal axes over a two-dimensional domain. In this case performance of the formulation with respect to oscillation control in the presence of multi-dimensional flow is verified.

In all examples the RK approximation was constructed using linear basis and circular kernel supports. Normalized support size of 1.75 was used, where the normalized support is the support size divided by nodal spacing. Temporal integration was performed by central differencing so that the uncorrected solution is fully second-order accurate in space and time. The time step for each problem was selected using a Courant number of 0.25. For the shock detection algorithm the absolute value of the high-pass solution was used as the shock indicator, with limiting criterion $\left|u^h_{high}(\boldsymbol{x}_I)\right| > 0.03$.

4.6.1 Linear advection

The linear advection equation is solved for the propagation of a smooth wave in the *x*-direction of a two-dimensional domain. The analytical flux function is

$$\boldsymbol{F}\big(u(\boldsymbol{x},t)\big) = \begin{bmatrix} u(\boldsymbol{x},t) \\ 0 \end{bmatrix} \qquad \text{eq. 136}$$

Initial and boundary conditions were, respectively,

$$u(\boldsymbol{x},0) = \begin{cases} 1 & z < 0 \\ 1 - 6z^2 + 6z^3 & 0 \le z < 0.5 \\ 2(1-z)^3 & 0.5 \le z < 1 \\ 0 & 1 < z \end{cases} \qquad z = (x - 0.1)/0.5 \qquad \text{eq. 137}$$

$$u(x = 0, t) = 1 \quad \& \quad u(x = 1, t) = 0 \qquad \text{eq. 138}$$

Results are shown in Figure 16 and Figure 17, where the nodal spacing is $\Delta x = 0.0125$. Since the solution remained smooth the detection algorithm did not detect a shock and therefore only the SFD is invoked in the flux divergence calculation while the velocity field remains uncorrected. As seen in Figure 16 the wave solution remains smooth and propagates uniformly in time. Figure 17 confirms solution convergence to the exact solution with refinement of the nodal spacing. For the coarser discretizations there are small oscillations at the head of the wave that are reduced with refinement. These are not considered Gibbs-type oscillations since they are essentially eliminated with model refinement, as compared to shock-induced oscillations that remain persistent at the jump. Based on the results of this problem, accuracy of the proposed SFD formulation for smooth wave propagation is verified.

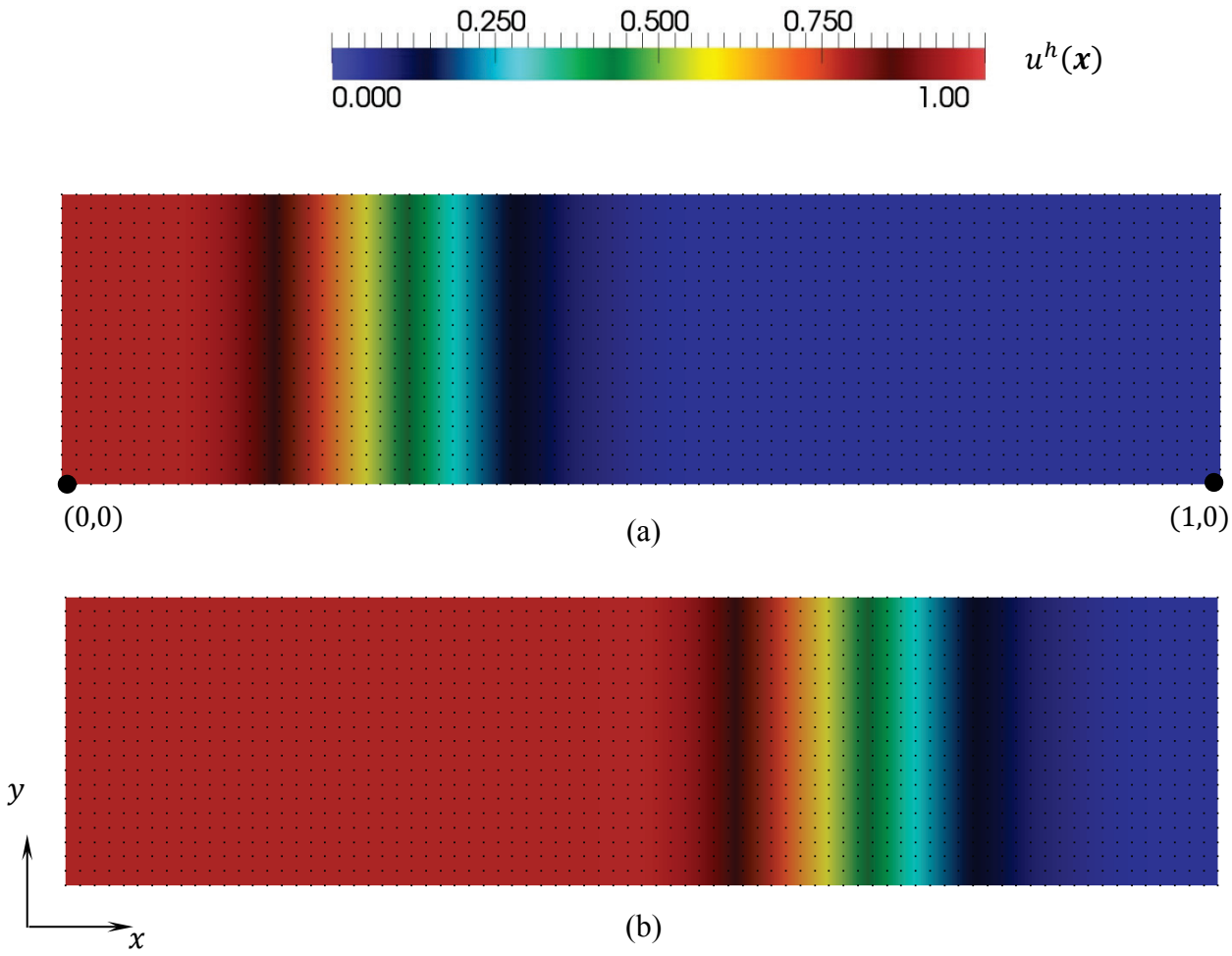

Figure 16. Smooth advection wave, a) initial conditions, and b) RKPM solution at $t = 0.4$

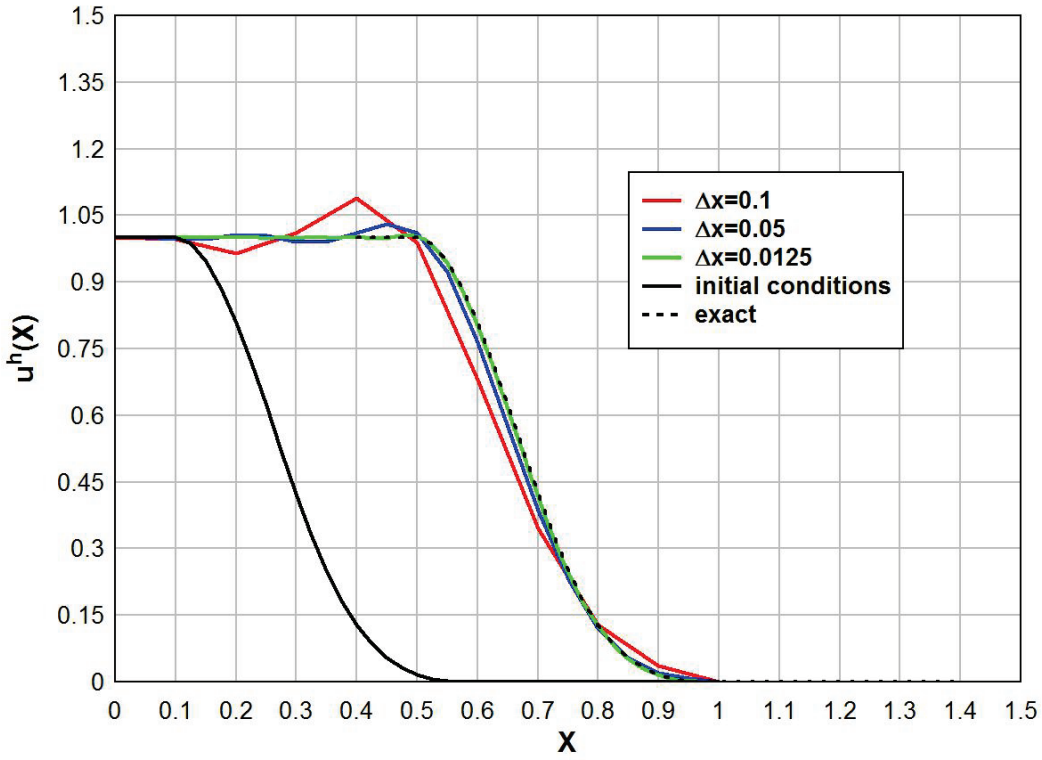

Figure 17. Solution convergence for smooth advection wave using RKPM shock modeling formulation

4.6.2 Nonlinear Burgers' equation with rarefaction formation

In this example the nonlinear Burgers' equation is solved with an initial condition jump condition selected to form a plane rarefaction wave. The analytical flux function is

$$\boldsymbol{F}\big(u(\boldsymbol{x},t)\big) = \begin{bmatrix} 0.5u(\boldsymbol{x},t)^2 \\ 0 \end{bmatrix} \qquad \text{eq. 139}$$

Initial and boundary conditions were, respectively,

$$u(\boldsymbol{x},0) = \begin{cases} 1 & x \le 1 \\ 2 & x > 1 \end{cases} \qquad \text{eq. 140}$$

$$u(x=0,t) = 1 \quad \& \quad u(x=2,t) = 2 \qquad \text{eq. 141}$$

Initial conditions and results from the corrected and uncorrected RKPM solutions are given in Figure 18, where the nodal spacing is $\Delta x = 0.0125$. In this rarefaction case the initial discontinuity degenerates into a smoothly expanding rarefaction wave. The corrected RKPM solution at time $t = 0.3$ (97 time steps) is shown in Figure 18b. The detection algorithm detected the initial discontinuity and applied the flux-corrected velocity for the first 15 steps. The corrected solution exhibited a very small oscillation behind the fan as a result of the initial discontinuity, with a maximum overshoot of 3 percent. The magnitude of the oscillations reduced with distance from the fan. The uncorrected solution at the same time is shown in Figure 18c. The initial discontinuity caused much larger oscillation error behind the wave that persisted with time; the maximum overshoot was 10 percent. These oscillations caused significant pollution of the solution well behind the wave. In Figure 19

the corrected and uncorrected solutions are compared with a fine scale Lax-Friedrichs (LF) solution (5x finer discretization) that was provided as a reference. The corrected RKPM solution closely matches the reference with nearly the same sharpness as the uncorrected. However, due to the locally-applied correction in the first 15 steps the oscillations driven by the initial discontinuity were limited. Consequently, the corrected RKPM formulation provided a much more accurate rarefaction solution in comparison to the uncorrected.

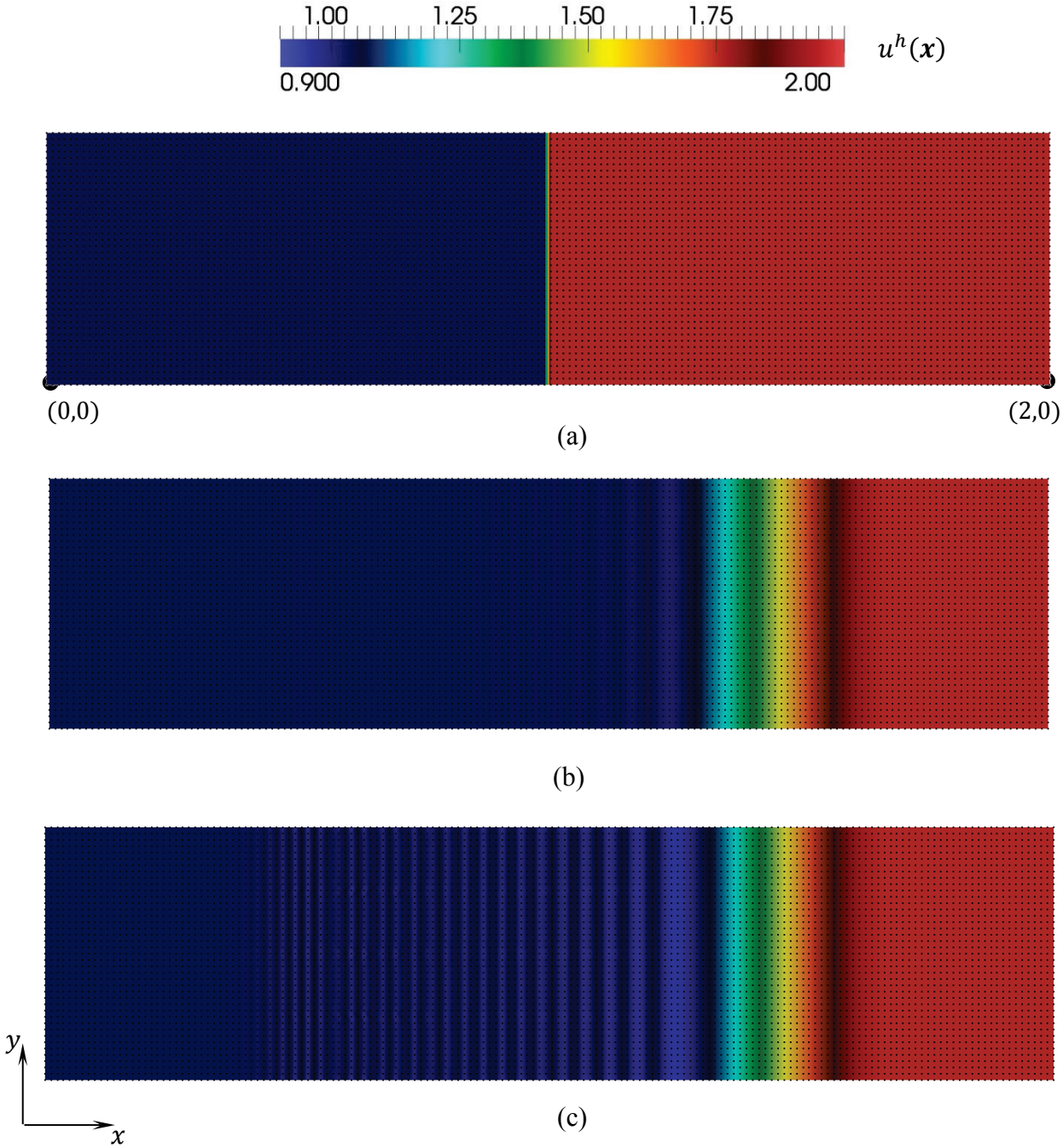

Figure 18. Rarefaction wave, a) initial conditions, b) corrected RKPM solution at $t = 0.3$, and c) uncorrected RKPM solution at $t = 0.3$

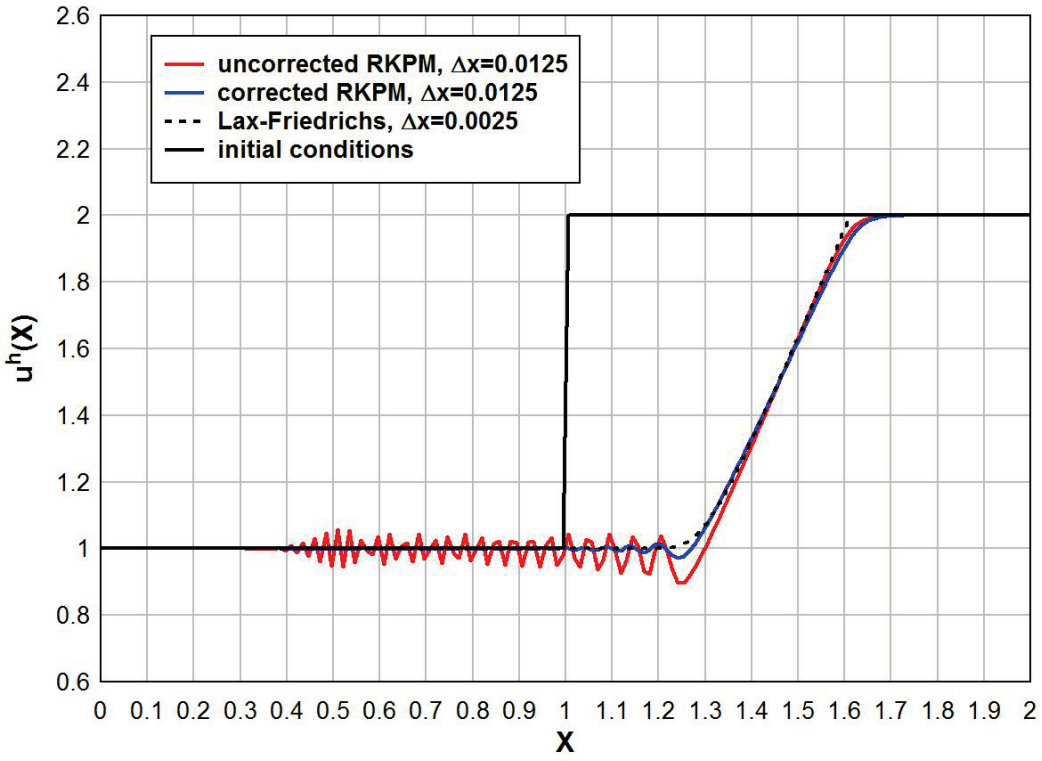

Figure 19. Rarefaction wave, comparison of corrected and uncorrected RKPM solutions to LF reference solution

4.6.3 Nonlinear Burgers' equation with plane shock formation

In this example nonlinear Burgers' equation with the flux in eq. 139 is solved again, but with smooth initial conditions that evolve into a shock according to the flux non-linearity. Initial conditions and boundary conditions were, respectively,

$$u(\boldsymbol{x},0)=\begin{cases}0.25(1-6z^2+6z^3) & 0\le z<0.5\\ 0.5(1-z)^3 & 0.5\le z<1\\ 0 & 1<z\end{cases}\qquad z=|x-0.3|/0.2 \qquad \text{eq. 142}$$

$$u(x=0,t)=0 \quad \& \quad u(x=1,t)=0 \qquad \text{eq. 143}$$

Results from the corrected and uncorrected RKPM solutions are shown in Figure 20 and Figure 21, respectively. Nodal spacing was $\Delta x = 0.00625$. The smooth initial conditions are shown in Figure 20a and the corrected RKPM solution at time $t = 0.6$ (385 steps) is shown in Figure 20b. Due to the non-linear flux the initially smooth conditions transformed into a shock wave traveling towards the right. In the corrected solution the shock formation was detected after 240 steps. Using the flux-corrected velocity in the shock region, oscillations were controlled while maintaining a sharp front. Prior to that time the solution was sufficiently smooth to use the uncorrected solution without loss of accuracy due to oscillation. The uncorrected solution at the same time is shown in Figure 21, which oscillated strongly. The corrected and uncorrected RKPM solutions are compared to a first-order Godunov solution and a fine-scale Lax-Friedrichs (LF) reference solution in Figure 22a and Figure 22b. Figure 22a shows the solution after 190 steps, just before the shock

formation occurs. Here the corrected and uncorrected solutions are the same because the shock has not formed and consequently no correction was made. The dissipative effect of the fully first-order accurate Godunov solution is observed; the Godunov method under-predicted the wave peak even for the smooth solution. Figure 22b compares the solutions after shock formation. The uncorrected solution oscillates strongly, and the Godunov solution is excessively dissipative. Using the adaptive flux-corrected velocity, the corrected RKPM solution gave a more accurate smooth solution and sharper shock peak while avoiding strong oscillations at the jump.

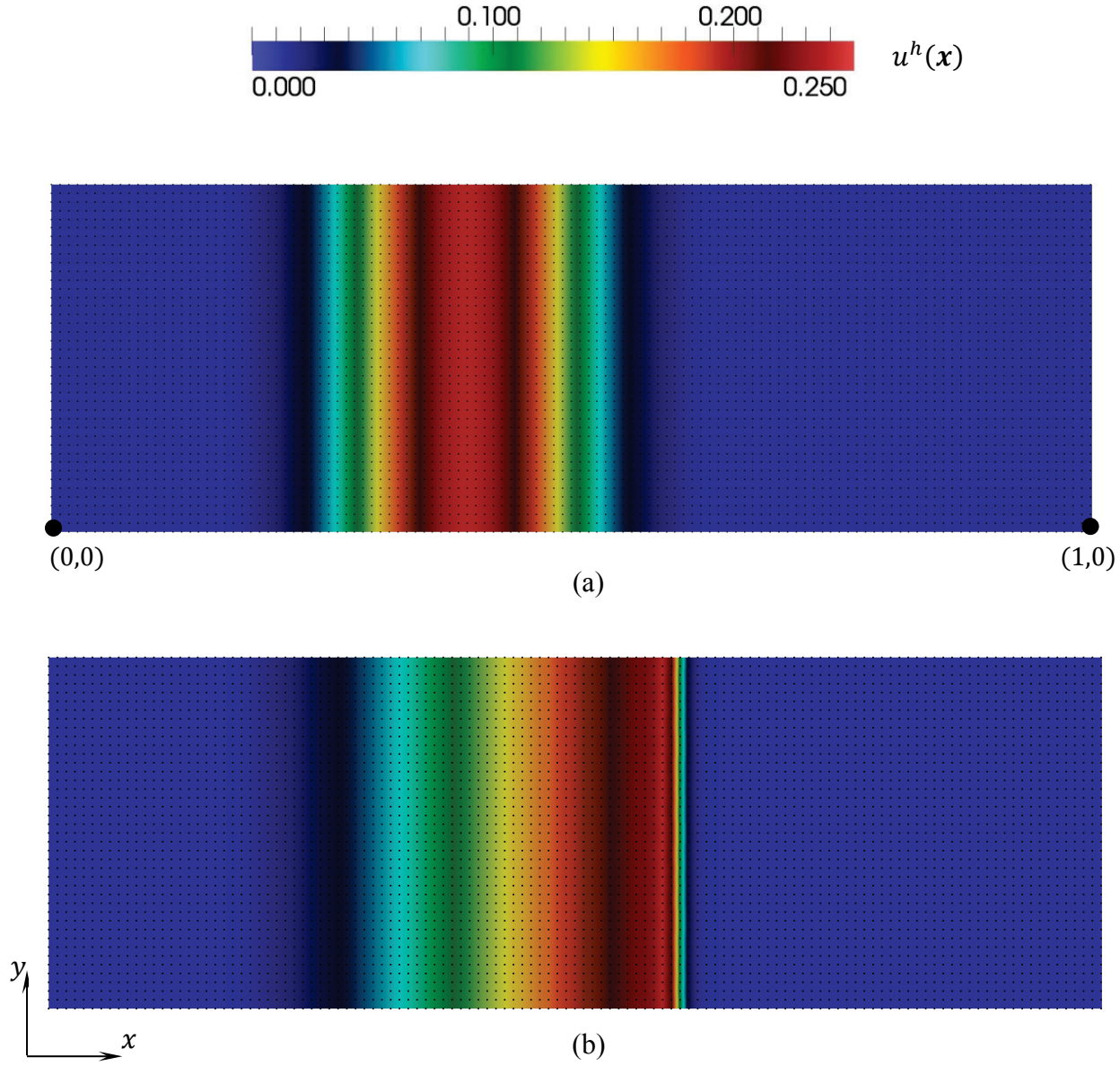

Figure 20. Plane shock wave, a) initial conditions, and b) corrected RKPM solution at $t = 0.6$

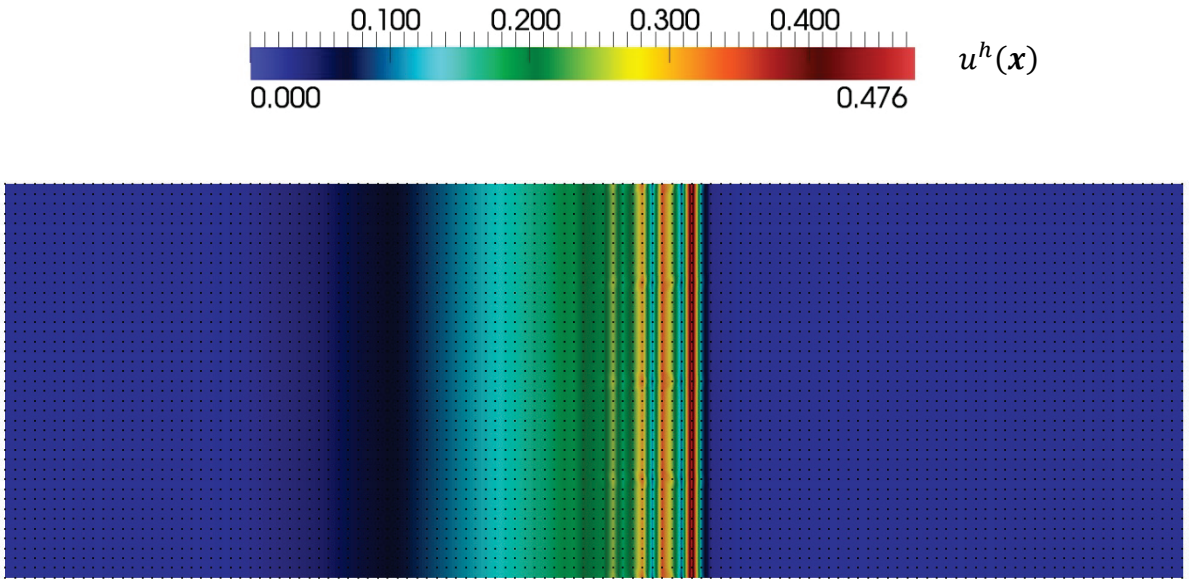

Figure 21. Plane shock wave, uncorrected RKPM solution at $t = 0.6$

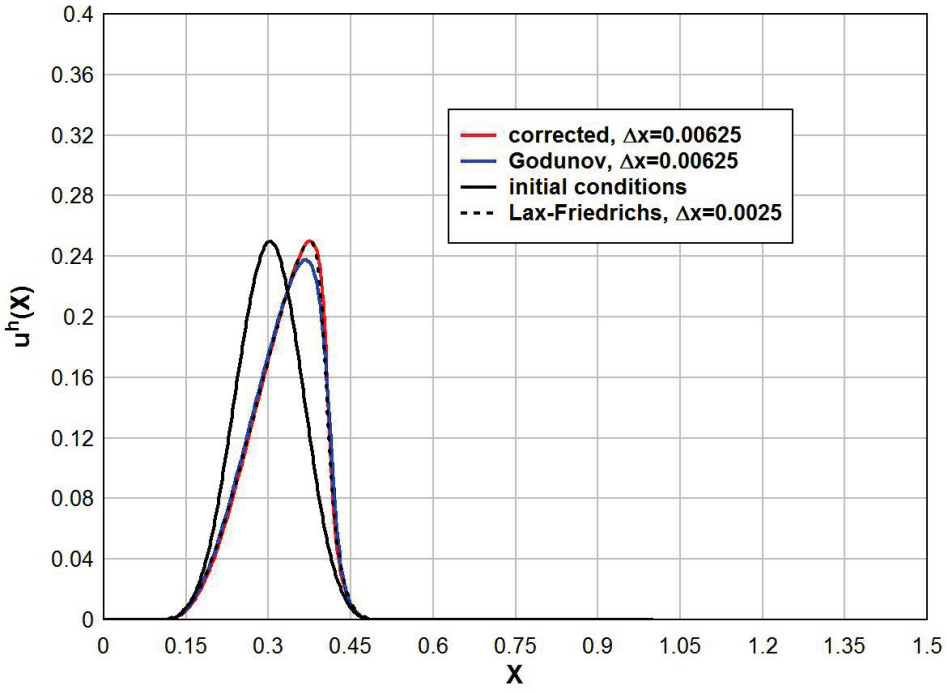

(a)

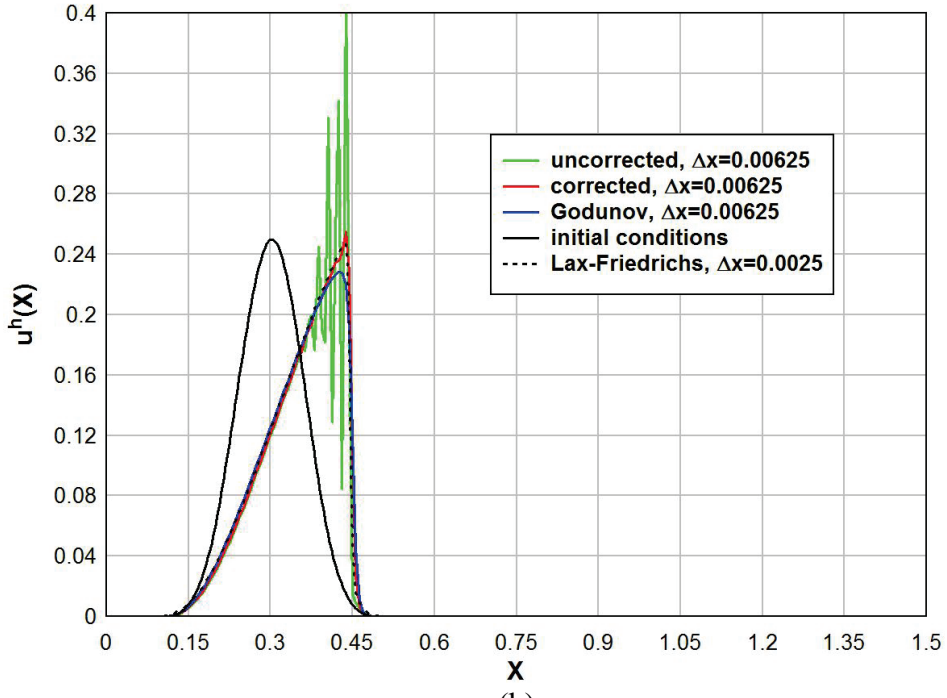

(b)

Figure 22. Plane shock wave, comparison of corrected and uncorrected RKPM solutions to Godunov and LF reference solution a) before shock formation and b) after shock formation

4.6.4 Nonlinear Burgers' equation with 2D shock propagation

In this example the nonlinear Burgers' equation is solved, but with the flux definition

$$\boldsymbol{F}\big(u(\boldsymbol{x},t)\big) = \begin{bmatrix} 0.5u(\boldsymbol{x},t)^2 \\ 0.5u(\boldsymbol{x},t)^2 \end{bmatrix} \qquad \text{eq. 144}$$

which yields two-dimensional wave propagation. Accordingly, this example tests the proposed formulation's ability to capture multi-dimensional shock wave propagation. Initial and boundary conditions were, respectively,

$$u(\boldsymbol{x},0) = \begin{cases} 1 & y \le (0.5 - x) \\ 0 & otherwise \end{cases} \qquad \text{eq. 145}$$

$$u(x = 0, t) = 1 \quad \& \quad u(y = 0, t) = 1 \qquad \text{eq. 146}$$

Results from the corrected RKPM solution are shown in Figure 23, where the nodal spacing was $\Delta x = 0.025$. The initial conditions with a regular nodal discretization are shown in Figure 23a. The corrected RKPM solution at time $t = 0.6$ with a regular discretization is shown in Figure 23b, and the same with an irregular discretization is shown in Figure 23c. The irregular discretization was constructed by using a random number generator operating on the regular nodal spacing in order to shift the nodal locations. Both of the corrected solutions are free of oscillation and sharply capture the wave which is propagating oblique to the discretization direction. In Figure 23c the wave front has a slight roughness transverse to the wave direction. This was caused by the way the initial conditions were specified on the irregular discretization, where the initial conditions had the same roughness. It is not a result

of the shock modeling formulation. Therefore, this example shows that by using the flux-corrected velocity to adaptively correct the RKPM solution at the shock front, oscillations were controlled for both regular and randomly distributed discretizations in the presence of multi-dimensional shock propagation.

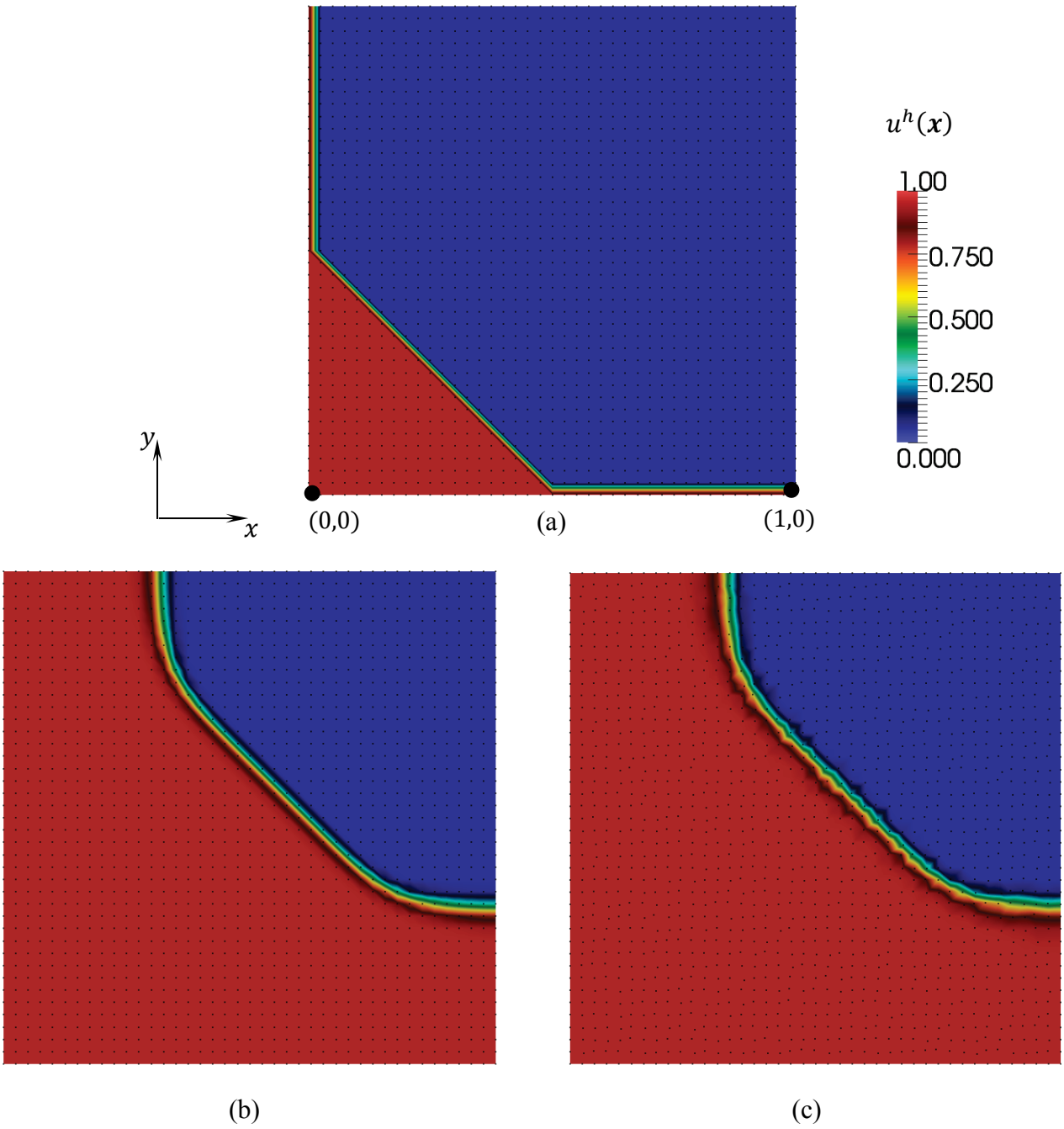

Figure 23. 2D shock wave at $t = 0.6$, a) initial conditions, b) corrected RKPM solution at with regular discretization, and c) corrected RKPM solution with irregular discretization

CHAPTER 5 RKPM FORMULATION FOR SHOCKS IN NONLINEAR SOLIDS

Many challenging engineering and scientific problems involve the response of nonlinear solid materials to extreme dynamic loading. The accompanying hydrodynamic effects are crucial, where the shock-driven pressure can dominate material response. In this chapter the RKPM shock modeling formulation for scalar conservation laws is extended to Cauchy's equation of motion for accurate shock modeling in nonlinear solids. Decomposition of the internal force vector into deviatoric and volumetric parts is employed, where the deviatoric part retains the material shear response and the volumetric part is corrected to embed the shock physics and provide oscillation control. Correction of the volumetric internal force vector is accomplished by introducing the Rankine-Hugoniot (R-H) jump equation for momentum conservation to the volumetric stress divergence through a smooth divergence operator. The divergence operator correction follows a Godunov-type approach using a Riemann problem formulated under the framework of SCNI. The Riemann solution is obtained from the R-H jump equation and enforces the physically correct shock propagation in accordance with the physics of entropy production. Through the embedded Riemann problem, the corrected divergence operator also engenders the formulation with an oscillation-limiting feature. Appropriate construction of the Riemann problem in the state and field variable approximations are used to control oscillation at the jump, without

requiring arbitrary parameters and length scales as in the traditional artificial viscosity approach. A new power function kernel for construction of the RK approximation is also introduced, which assists in controlling oscillation of the numerical solution at the jump. Nodal pressures are updated according to a Hugoniot-based deformation measure, which provides consistency with the Hugoniot-corrected volumetric stress divergence.

5.1 Power function kernel for approximation of discontinuities

Locality and smoothness of the RK approximation are governed by the behavior of the kernel function, $\phi_a(\boldsymbol{x} - \boldsymbol{x}_I)$ in eq. 67. A typically used set of kernels are the family of B-spline functions, which provide high levels of continuity and accuracy for smooth solutions due to the functions' inherent smoothness. In this research, a different type of kernel function was investigated, referred to herein as a power function kernel. The power function kernel is designed to be highly localized for use in approximating the rough, discontinuous solutions that are of importance in shock models. The increased localization provides a more accurate jump approximation and yields a reduced Gibbs phenomenon.

The power function is used as the kernel weighting over the compact support in the reproducing kernel approximation. In contrast to the cubic B-spline, weighting with distance from the kernel centroid is significantly reduced with this power function. The power function kernel is defined in eq. 147; the cubic B-spline kernel is given in eq. 148 for comparison. The measure of normalized distance from the kernel centroid, z, is defined in eq. 149, where $\boldsymbol{x}_I$ is the coordinate of the I^{th} node located at the kernel center and a is the

size of the compact support.

$$\phi_a(\boldsymbol{x}-\boldsymbol{x}_I)=\begin{cases}(1-z)^{\alpha} & 0\le z\le 1\\ 0 & 1<z\end{cases} \qquad \text{eq. 147}$$

$$\phi_a(\boldsymbol{x}-\boldsymbol{x}_I)=\begin{cases}1-6z^2+6z^3 & 0\le z\le 1/2\\ 2(1-z)^3 & 1/2<z\le 1\\ 0 & 1<z\end{cases} \qquad \text{eq. 148}$$

$$z=\frac{\|\boldsymbol{x}-\boldsymbol{x}_I\|}{a} \qquad \text{eq. 149}$$

In the power function kernel, the power term α controls the amount of kernel localization; increasing values of α result in increased locality. The kernel imparts C^0 continuity to the RK approximation due to the discontinuous derivative at the kernel centroid (i.e., at $z=0$). However, the discontinuous derivative is not an issue for integration techniques such as the meshfree SCNI [27] or SNNI [34], where nodal derivatives are not required. Away from the centroid the power function kernel provides arbitrarily high order of continuity according to the power term, but remains localized about the centroid.

An example of the power function kernel with power term values of $\alpha=2,4,\text{and }24$ is shown in Figure 24. The kernel is plotted over a kernel support domain with support size of $a=1$. A cubic B-spline kernel is plotted over the same domain for comparison. The localized nature of the power function kernel is clear, where the weighting localizes towards the kernel centroid with increasing values of α. Weighting towards the edges of the support is significantly reduced in comparison to the B-spline.

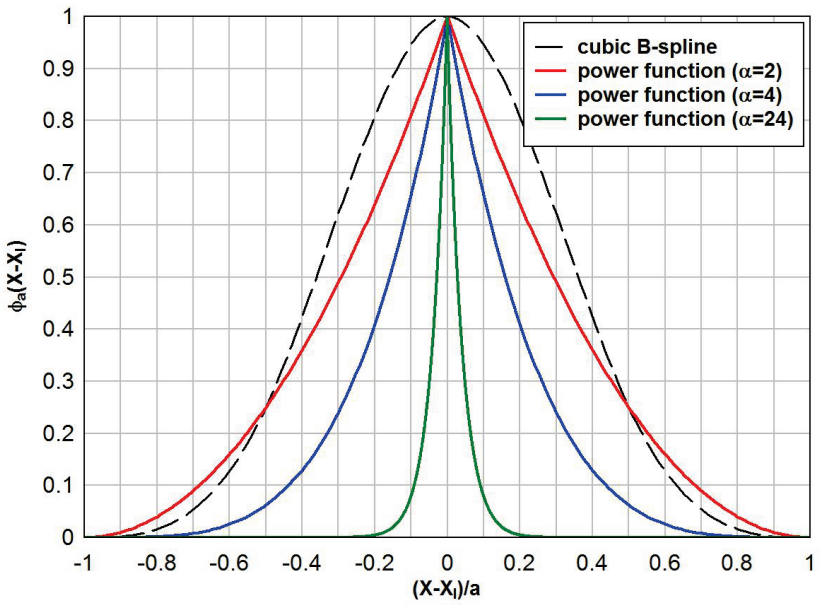

Figure 24. Comparison of power function (varying α) and B-spline kernels

The RK shape functions computed from eq. 67 with the power and B-spline kernels are compared in Figure 25; power function kernels with varying α values are shown alongside the corresponding shape functions. The shape functions were constructed with a linear basis, and the normalized support, defined as the support size divided by nodal spacing (a/h), was 2. According to this normalized support size the kernel support spans the distance of two nodal spaces away from the kernel centroid. In both cases the shape function is continuous over the full support domain. However, due to locality of the power function kernel, for increasing values of α the shape function value is essentially zero beyond the first pair of nodes adjacent to the centroid. In contrast, the shape function calculated from the cubic B-spline generates a much smoother weight distribution over the entire support. In the presence

of a discontinuity this will result in a stronger cross-jump interpolation. Another beneficial property of the power function kernel is recovery of a near kronecker delta condition, which is not generally obtained with the RK shape functions. Increasing values of the power term yield convergence toward the kronecker delta property, as shown in Figure 25.

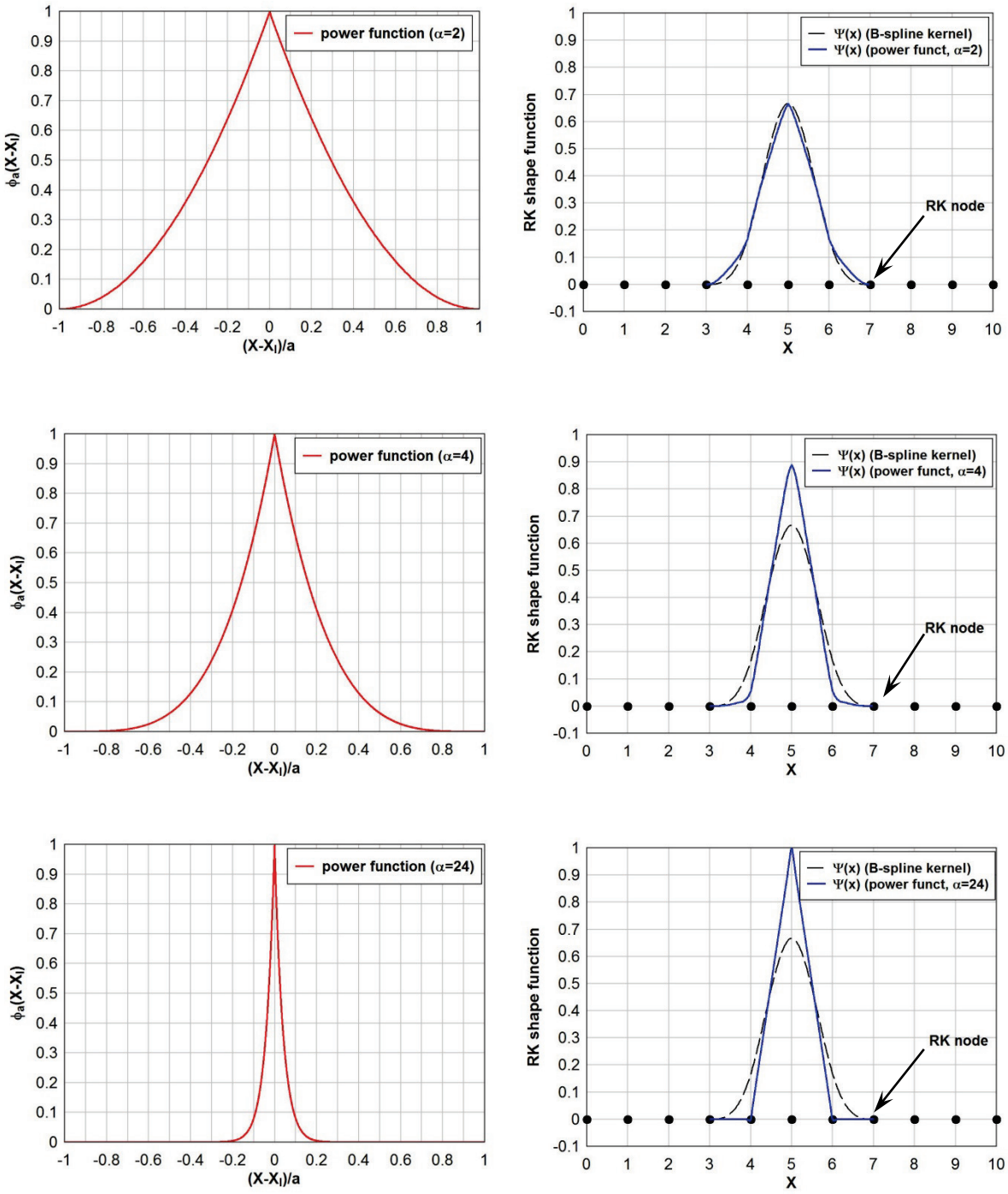

Figure 25. RK shape functions computed using the power function and B-spline kernels

To compare the approximation properties of the power function and B-spline kernels, the one-dimensional step function

$$u(x) = \begin{cases} 2 & 0 \leq x \leq 0.5 \\ 1 & 0.5 < x \leq 1 \end{cases} \quad \text{eq. 150}$$

was approximated over the domain $x \in [0,1]$. The set of nodal coefficients $\{d_I\}_{I=1}^{np}$ was solved by least squares minimization of

$$r = \sum_{I=1}^{np} \left(u_I - u_I^h\right)^2 \quad \text{eq. 151}$$

where r is the squared residual to be minimized, u_I is the solution of eq. 150 at x_I, and u_I^h is the RK approximation from eq. 58 evaluated at x_I. The RK shape functions were constructed using linear basis and a normalized support of 2. The power function and B-spline kernel approximations are compared in Figure 26. The cubic B-spline exhibits a strong overshoot at the jump with oscillations behind it. The power function approximation reduces oscillation with increasing values of α; for the approximation using $\alpha = 24$ there is a very small overshoot near the first node adjacent to the jump and is essentially non-oscillatory over the remainder of the domain. In Figure 26 the jump is located between the nodes, showing that there is no requirement for the discretization points to exactly coincide with the discontinuity in order for the power function to control oscillation.

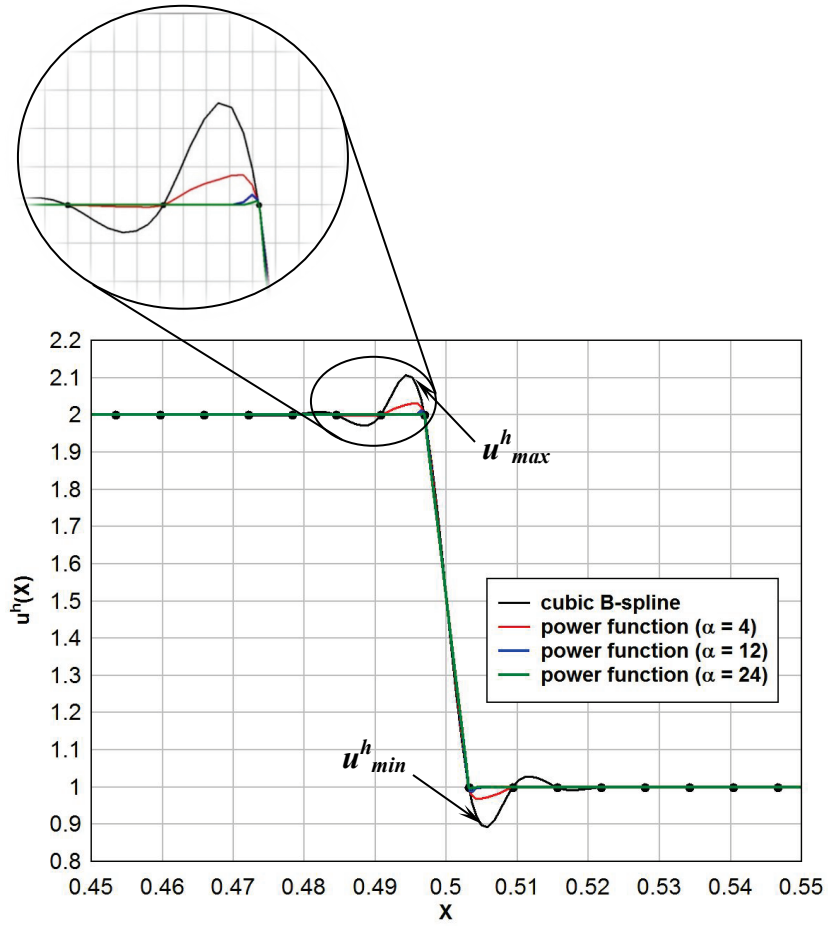

Figure 26. Discontinuity approximation using power function and B-spline kernels

An error measure is defined to quantify the jump error

$$err_{jump} = \left(u^h_{max} - u^h_{min}\right) - 1 \qquad \text{eq. 152}$$

where u^h_{max} and u^h_{min} are shown in Figure 26. The jump error for the approximation with the cubic B-spline was approximately 21 percent; the jump error for the power function approximation ($\alpha = 24$) was less than 1 percent.

Approximation behavior of the power function kernel was also investigated in two dimensions. As an example, the two dimensional step function

$$u(\boldsymbol{x}) = \begin{cases} 1 & x + y \leq 1 \\ 0 & otherwise \end{cases} \qquad \text{eq. 153}$$

was approximated using the power function and B-spline kernels. The shape functions were formed with linear basis and normalized support of 2. Approximation results are compared in Figure 27; note that the color scale is limited to a range of 0.75-1.25 to focus on the oscillations behind the jump. Similar to the one-dimensional results, the cubic B-spline approximation is oscillatory in the directions parallel and transverse to the discontinuity. In comparison, the power function approximation is non-oscillatory. The roughness in the power function approximation parallel with the discontinuity is due to interpolation between the discrete RK points, it is not oscillation due to the discontinuity.

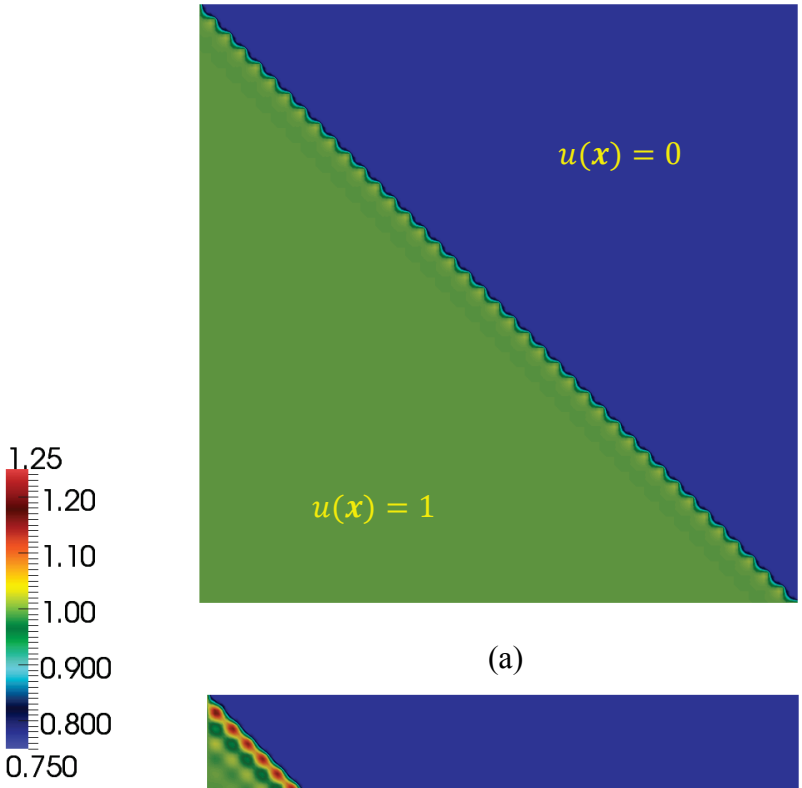

(a)

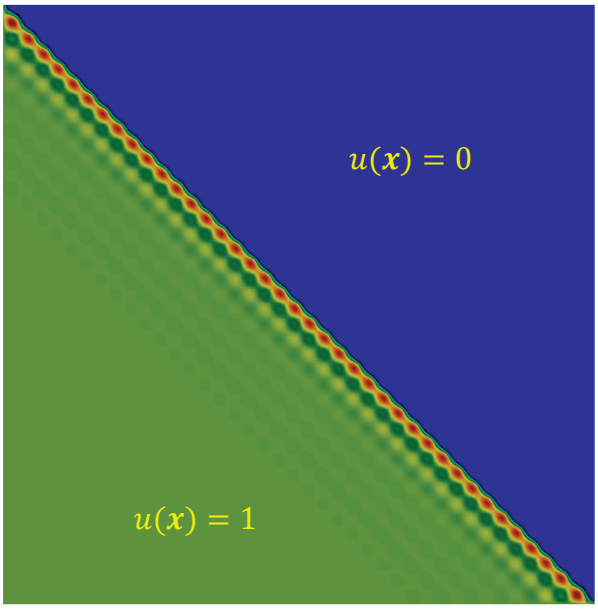

(b)

Figure 27. 2D discontinuity approximation using a) power function and b) B-spline kernels

To investigate the kernel functions' influence on convergence behavior, an error analysis was performed using the L_2 error norm. First the approximation of a smooth sine function was considered

$$u(x) = \sin(\pi x) \quad x \in [0,1] \qquad \text{eq. 154}$$

where linear basis and normalized support of 1.5 were used. The convergence analysis using power function (varying α values) and B-spline kernels is shown in Figure 28a. The convergence rate using both kernels is 2.0, which matches the theoretically expected rate. This shows that the power function kernel does not affect the solution convergence, since only continuity and locality are governed by the kernel. Accuracy of the power function kernel was not significantly affected by a change in power value, and the power function kernel accuracy for both α is somewhat lower than the B-spline because of the increased kernel locality. However, the design intent for the power function is application to rough solutions as in shocks, so this is not considered an issue. Convergence analysis was also performed for approximation of the discontinuous function in eq. 150. To focus on the oscillatory error, the analysis was limited to the subdomain upstream of the jump, i.e., from $x = 0$ to the first node upstream of the jump. The convergence analysis using various power term values is shown in Figure 28b. For this rough function, accuracy of the power function approximation significantly increases with increases in α. As with the smooth sine function, convergence rate is not affected by the change in kernel locality. The lower convergence rate in Figure 28b is due to the step function roughness.

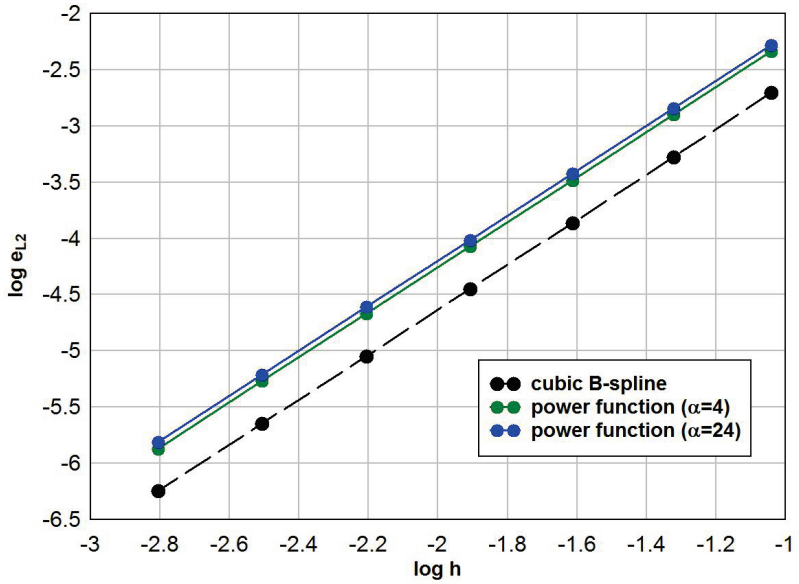

(a)

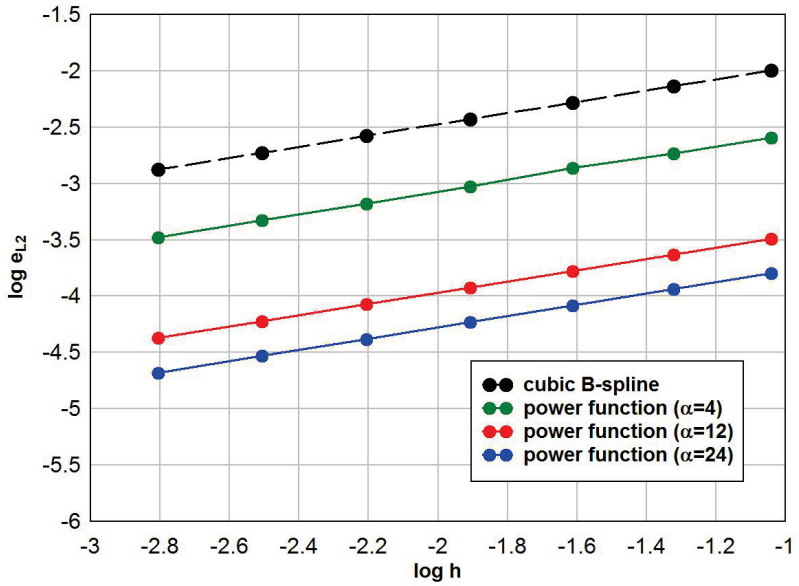

(b)

Figure 28. Comparison of L_2 convergence, a) smooth sine function, and b) discontinuous function

5.2 Weak form equation and Galerkin approximation

The shock modeling formulation for non-linear solids is constructed as a weak form of Cauchy's equation of motion

$$\rho\ddot{\boldsymbol{u}}(\boldsymbol{x},t) - \boldsymbol{\nabla}\cdot\boldsymbol{\tau}(\boldsymbol{x},t) + \rho\boldsymbol{b}(\boldsymbol{x},t) = \boldsymbol{0} \qquad \text{eq. 155}$$

where ρ is the material density, $\ddot{\boldsymbol{u}}(\boldsymbol{x},t)$ is acceleration of the solid, $\boldsymbol{\tau}(\boldsymbol{x},t)$ is Cauchy's stress tensor, and $\boldsymbol{b}(\boldsymbol{x},t)$ is the body force per unit mass. Here the notation $\boldsymbol{x}$ indicates a term in the deformed configuration; this is distinguished from the notation $\boldsymbol{X}$ used later in reference to the undeformed configuration. In the proposed formulation for solids the volumetric stress divergence (or equivalently the pressure gradient) is corrected to embed the essential shock physics and enforce oscillation control at the jump. To facilitate this correction, Cauchy's stress is decomposed into volumetric and deviatoric parts so that eq. 155 becomes

$$\rho\ddot{\boldsymbol{u}}(\boldsymbol{x},t) - \boldsymbol{\nabla}\cdot\boldsymbol{\tau}^{d}(\boldsymbol{x},t) - \boldsymbol{\nabla}\cdot\boldsymbol{\tau}^{v}(\boldsymbol{x},t) + \rho\boldsymbol{b}(\boldsymbol{x},t) = \boldsymbol{0} \qquad \text{eq. 156}$$

where $\boldsymbol{\tau}^{d}(\boldsymbol{x},t)$ and $\boldsymbol{\tau}^{v}(\boldsymbol{x},t)$ are the deviatoric and volumetric parts of Cauchy's stress, respectively. The volumetric stress divergence correction is constructed under the framework of SCNI [27, 28]. SCNI utilizes a conforming integration cell topology, and as a consequence is most efficiently used in conjunction with a total Lagrangian formulation to avoid topology reconstruction. Accordingly, the weak form of eq. 156 is expressed in the undeformed configuration as

$$\int_{\Omega^X} \rho^0 \boldsymbol{w}(\boldsymbol{X},t) \cdot \ddot{\boldsymbol{u}}(\boldsymbol{X},t) d\Omega + \int_{\Omega^X} \boldsymbol{\nabla w}(\boldsymbol{X},t) : \boldsymbol{\sigma}^d(\boldsymbol{X},t)\, d\Omega - \int_{\Omega^X} \boldsymbol{w}(\boldsymbol{X},t) \cdot$$

$$\left(\boldsymbol{\nabla} \cdot \boldsymbol{\sigma}^v(\boldsymbol{X},t)\right) d\Omega - \int_{\Gamma_h^X} \boldsymbol{w}(\boldsymbol{X},t) \cdot \boldsymbol{h}^0(\boldsymbol{X},t)\, d\Gamma + \int_{\Omega^X} \rho^0 \boldsymbol{w}(\boldsymbol{X},t) \cdot \boldsymbol{b}(\boldsymbol{X},t)\, d\Omega = 0 \quad \text{eq. 157}$$

where $\boldsymbol{w}(\boldsymbol{X},t) \in H_g^1$ is a test function, $\rho^0$is the material density in the undeformed configuration, and $\int_{\Omega^X} \cdots d\Omega$ and $\int_{\Gamma_h^X} \cdots d\Gamma$ indicate domain and contour integrals in the undeformed configuration. In eq. 157 the terms $\boldsymbol{\sigma}^d(\boldsymbol{X},t)$ and $\boldsymbol{\sigma}^v(\boldsymbol{X},t)$ indicate stress measures in the undeformed configuration that are derived from an appropriate transformation of the Cauchy stress, such as the Piola-Kirchoff stresses or others [119]. The term $\boldsymbol{h}^0(\boldsymbol{X},t)$ is the surface traction expressed in the undeformed configuration, i.e., $\boldsymbol{h}^0(\boldsymbol{X},t) = \boldsymbol{N}(\boldsymbol{X}) \cdot \boldsymbol{\sigma}(\boldsymbol{X},t)$. In the following weak form construction, integration by parts was only applied to the domain integration of the deviatoric stress. The volumetric portion was not integrated by parts in order to maintain the volumetric stress divergence in the variational equation so that its correction can be constructed later for the desired purposes. Although integration by parts was limited to the deviatoric stress, we have considered the contour integral over the natural boundary to include $\boldsymbol{h}^0(\boldsymbol{X},t)$, which is the total surface traction due to deviatoric and volumetric stresses. Use of the volumetric stress divergence correction to recover the total surface traction due to volumetric and deviatoric stresses is given in Section 5.5.

The approximated trial and test functions, $\boldsymbol{u}^h(\boldsymbol{X},t)$ and $\boldsymbol{w}^h(\boldsymbol{X},t)$ respectively, are introduced to the weak form equation to obtain the Galerkin approximation

$$\int_{\Omega^X} \rho^0 \boldsymbol{w}^h(\boldsymbol{X},t)\cdot\ddot{\boldsymbol{u}}^h(\boldsymbol{X},t)d\Omega + \int_{\Omega^X} \boldsymbol{\nabla} \boldsymbol{w}^h(\boldsymbol{X},t){:}\,\boldsymbol{\sigma}^d(\boldsymbol{X},t)\,d\Omega - \int_{\Omega^X} \boldsymbol{w}^h(\boldsymbol{X},t)\cdot$$

$$\left(\boldsymbol{\nabla}\cdot\boldsymbol{\sigma}^v(\boldsymbol{X},t)\right)d\Omega - \int_{\Gamma_h^X} \boldsymbol{w}^h(\boldsymbol{X},t)\cdot\boldsymbol{h}^0(\boldsymbol{X},t)\,d\Gamma + \int_{\Omega^X}\rho^0\boldsymbol{w}^h(\boldsymbol{X},t)\cdot\boldsymbol{b}(\boldsymbol{X},t)\,d\Omega = 0 \quad \text{eq. 158}$$

where $\ddot{\boldsymbol{u}}^h(\boldsymbol{X},t) = \sum_{I=1}^{np}\Psi_I(\boldsymbol{X})\,\ddot{\boldsymbol{d}}_I(t)$, $\boldsymbol{w}^h(\boldsymbol{X},t) = \sum_{I=1}^{np}\Psi_I(\boldsymbol{X})\,\boldsymbol{c}_I(t)$; $\boldsymbol{c}_I(t)$ are the coefficients corresponding to the test function, and the RK shape functions are constructed in the undeformed configuration. Since the shape functions are constructed in the undeformed configuration, they only need to be calculated once at the beginning of the simulation, which is a beneficial feature of this total Lagrangian formulation.

For strong shock problems, eq. 158 needs to contain the essential shock physics. Further, this weak treatment is prone to strong oscillation when higher-order spatial approximations are introduced at the shock. To address these issues the volumetric stress divergence is corrected, which is denoted as $\tilde{\boldsymbol{S}}(\boldsymbol{X},t)$ and is discussed in the next section. The corresponding weak form is

$$\int_{\Omega^X} \rho^0 \boldsymbol{w}^h(\boldsymbol{X},t)\cdot\ddot{\boldsymbol{u}}^h(\boldsymbol{X},t)d\Omega + \int_{\Omega^X} \boldsymbol{\nabla} \boldsymbol{w}^h(\boldsymbol{X},t){:}\,\boldsymbol{\sigma}^d(\boldsymbol{X},t)\,d\Omega - \int_{\Omega^X} \boldsymbol{w}^h(\boldsymbol{X},t)\cdot$$

$$\tilde{\boldsymbol{S}}(\boldsymbol{X},t)\,d\Omega - \int_{\Gamma_h^X} \boldsymbol{w}^h(\boldsymbol{X},t)\cdot\boldsymbol{h}^0(\boldsymbol{X},t)\,d\Gamma + \int_{\Omega^X}\rho^0\boldsymbol{w}^h(\boldsymbol{X},t)\cdot\boldsymbol{b}(\boldsymbol{X},t)\,d\Omega = 0 \quad \text{eq. 159}$$

The corrected Galerkin approximation in eq. 159 is the basis of the proposed hydrodynamic formulation for solids.

5.3 Corrected volumetric stress divergence

In the formulation for nonlinear solids to be discussed below, the volumetric stress divergence is corrected to introduce the essential shock physics and to also provide a mechanism for oscillation control. To construct the correction, begin by forming a smoothed divergence operation under the framework of SCNI. The operation is embedded with a Riemann problem that is formed on the SCNI integration cell topology and is solved using the R-H jump condition applied on the integration cell boundaries. As a consequence, the Riemann solution satisfies the entropy production constraint, e.g. [100], by following characteristic projections and ensuring recovery of the physically correct shock or rarefaction solution. Furthermore, through an appropriate approximation of the state and field variables used in the Riemann problem initial conditions, the formulation is made oscillation-limiting at the shock.

5.3.1 Smoothed volumetric stress divergence operation

To construct the smoothed divergence operation, consider the SCNI integration cell topology shown in Figure 13. The volumetric stress divergence at the I^{th} node is approximated as

$$\boldsymbol{\nabla}\cdot\boldsymbol{\sigma}^{v}(\boldsymbol{X},t)|_{\boldsymbol{X}_I} \approx \int_{\Omega_I^X} \boldsymbol{\nabla}\cdot\boldsymbol{\sigma}^{v}(\boldsymbol{X},t)\varphi(\boldsymbol{X};\boldsymbol{X}-\boldsymbol{X}_I)\, d\Omega \equiv \widetilde{\boldsymbol{\nabla}}\cdot\boldsymbol{\sigma}_I^{v}(t) \qquad \text{eq. 160}$$

A piecewise constant kernel function, $\varphi(\boldsymbol{X};\boldsymbol{X}-\boldsymbol{X}_I)$, is introduced to the approximation

$$\varphi(\boldsymbol{X};\boldsymbol{X}-\boldsymbol{X}_I) = \begin{cases} 1/V_I & \boldsymbol{X}\in\Omega_I^X \\ 0 & otherwise \end{cases} \qquad \text{eq. 161}$$

where $V_I = \int_{\Omega_I^X} d\Omega$. Using this kernel definition the smoothed volumetric stress divergence becomes

$$\widetilde{\boldsymbol{\nabla}} \cdot \boldsymbol{\sigma}_I^v(t) = (1/V_I) \int_{\Omega_I^X} \boldsymbol{\nabla} \cdot \boldsymbol{\sigma}^v(\boldsymbol{X}, t)\, d\Omega \qquad \text{eq. 162}$$

$$= (1/V_I) \int_{\Omega_I^X} \boldsymbol{\nabla} P(\boldsymbol{X}, t)\, d\Omega \qquad \text{eq. 163}$$

To obtain eq. 163, the definition of volumetric stress, $\boldsymbol{\sigma}^v(\boldsymbol{X}, t) = P(\boldsymbol{X}, t)\boldsymbol{I}$, was used, where $P(\boldsymbol{X}, t)$ is pressure and $\boldsymbol{I}$ is the identity matrix. Using the divergence theorem, eq. 163 can be transformed to the contour integral

$$\widetilde{\boldsymbol{\nabla}} \cdot \boldsymbol{\sigma}_I^v(t) = (1/V_I) \int_{\Gamma_I^X} P(\boldsymbol{X}, t)\boldsymbol{N}\, d\Gamma \qquad \text{eq. 164}$$

where $\boldsymbol{N}$ is the outward normal to Γ_I^X. To numerically integrate eq. 164, consider the boundary, Γ_I^X, in Figure 13 to be composed of a set of line segments, $\mathbb{L}_I = \{L_{Ik}\}_{k=1}^s$, where s is the total number of segments, and each segment is associated with a midpoint, length, and outward normal of $\boldsymbol{X}_{Ik}$, l_{Ik}, and $\boldsymbol{N}_{Ik}$, respectively. Using Newton-Cotes quadrature, the numerical approximation of the smoothed volumetric stress divergence is

$$\widetilde{\boldsymbol{\nabla}} \cdot \boldsymbol{\sigma}_I^v(t) = (1/V_I) \sum_{k=1}^s P(\boldsymbol{X}, t)|_{\boldsymbol{X}_{Ik}} \boldsymbol{N}_{Ik} l_{Ik} \qquad \text{eq. 165}$$

In eq. 165 an approximation of the pressure along the boundary of each integration cell is required, which is to be obtained from a Riemann problem solved with the Rankine-Hugoniot jump equation in the following section.

5.3.2 Riemann problem and R-H enriched boundary pressure

In the scalar law formulation a Riemann problem was formed on the SCNI integration cells, where the piecewise constant initial conditions formed numerical discontinuities at the cell boundaries. The Riemann solution was obtained by characteristic projections. In the nonlinear solids formulation a similar Riemann problem is defined on the integration cell topology. However, the numerical discontinuity is now viewed as a local contact shock problem that can be solved using the R-H jump equation relating pressure and particle velocity (referred to as the P-$\dot{u}$ Hugoniot hereafter). The solution of this boundary shock problem describes the behavior (velocity and magnitude) of shock waves emanating from the interface and is therefore similar to the solution obtained by characteristic projections. Consequently, the boundary shock problem ensures that the physically correct shock solution is embedded in the formulation, so that the properties of the second law of thermodynamics are enforced.

To construct the Riemann problem at each time step, initial conditions for pressure and particle velocity are formed as the cell-averaged solution within each SCNI integration cell

$$\bar{P}_I^n = (1/V_I) \int_{\Omega_I^X} P(\boldsymbol{X}, t^n) d\Omega \qquad \text{eq. 166}$$

$$\bar{\dot{\boldsymbol{u}}}_I^n = (1/V_I) \int_{\Omega_I^X} \dot{\boldsymbol{u}}(\boldsymbol{X}, t^n) d\Omega \qquad \text{eq. 167}$$

where $\dot{\boldsymbol{u}}(\boldsymbol{X}, t)$ denotes the particle velocity. For the integration cell topology shown in Figure 13, a one-dimensional Riemann problem can be defined across each segment of Γ_I^X,

where the Riemann problem is constructed along a local axis, $\widehat{\boldsymbol{X}}$, oriented parallel with the segment's outward normal, $\boldsymbol{N}$. The particle velocity in the direction of the local axis is required, and is found by the projection

$$\hat{u}_I^n = \bar{\dot{\boldsymbol{u}}}_I^n \cdot \boldsymbol{N} \qquad \text{eq. 168}$$

An example of the Riemann problem initial conditions constructed at the integration cell boundary between Ω_I and Ω_J is shown in Figure 29a. The boundary shock solution for the Riemann problem is sought at the point $\boldsymbol{X}_{Ik}$ in order to evaluate the smoothed volumetric stress divergence in eq. 165. To find the solution of $\dot{u}$ and P at the point $\boldsymbol{X}_{Ik}$, the P-$\dot{u}$ Hugoniot is utilized, e.g. [86]

$$[\![-P]\!] = \rho^0 U_s [\![\dot{u}]\!] \qquad \text{eq. 169}$$

where U_s is the shock velocity and $[\![\cdot]\!]$ is the difference operator. The experimentally determined relationship between shock velocity and particle velocity is also used, e.g. [86]

$$U_s = C_b sign[\![\dot{u}]\!] + A[\![\dot{u}]\!] \qquad \text{eq. 170}$$

which is a linear relationship for most materials and is typically determined by flyer plate impact experiments, i.e. [120]. In eq. 170, C_b is the bulk sound speed and A is the slope of the experimental data relating U_s and $\dot{u}$. By inserting eq. 170 into eq. 169, the pressure-particle velocity Hugoniot thermodynamic response curve discussed in Section 3.2 is obtained.

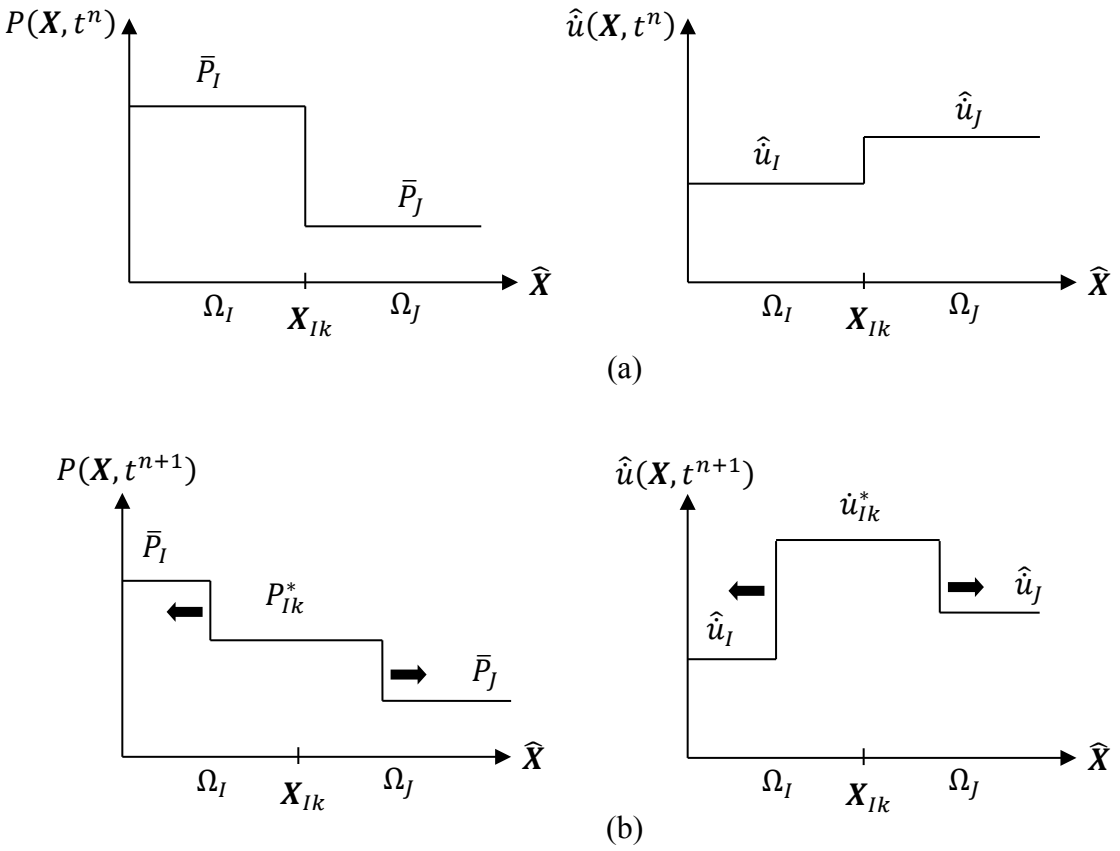

Figure 29. Riemann problem at integration cell boundary, a) initial conditions at time t^n, and b) boundary shock solution at time t^{n+1}

As shown in Figure 29b, the boundary shock solution consists of two discontinuities moving away from the interface. In the region between the discontinuities the consistency condition dictates that pressure and particle velocity be continuous across the interface, that is, at $\boldsymbol{X}_{Ik}$. Using this consistency requirement in conjunction with eq. 169 and eq. 170, a jump equation can be constructed across each of the new discontinuities propagating away from the boundary

$$(P_{Ik}^{*} - \bar{P}_I) = \rho_I^0 \{C_b sign(\dot{u}_{Ik}^{*} - \hat{u}_I) + A(\dot{u}_{Ik}^{*} - \hat{u}_I)\} (\dot{u}_{Ik}^{*} - \hat{u}_I) \quad \text{eq. 171}$$

$$(P_{Ik}^{*} - \bar{P}_J) = \rho_J^0 \{C_b sign(\dot{u}_{Ik}^{*} - \hat{u}_J) + A(\dot{u}_{Ik}^{*} - \hat{u}_J)\} (\dot{u}_{Ik}^{*} - \hat{u}_J) \quad \text{eq. 172}$$

where P_{Ik}^{*} and $\dot{u}_{Ik}^{*}$ are the boundary pressure and particle velocity at $\boldsymbol{X}_{Ik}$, respectively. These boundary terms are now available through the simultaneous solution of eq. 171 and eq. 172, which can be performed using a variety of techniques including Newton-Raphson methods and those proposed by van Leer [40] and Dukowicz [121]. The R-H enriched boundary pressure, P_{Ik}^{*}, can now be introduced to the smoothed volumetric stress divergence in eq. 165 to obtain

$$\tilde{\boldsymbol{S}}_I(t) = (1/V_I) \int_{\Gamma_I^X} P^{*}(\boldsymbol{X}, t) \boldsymbol{N} \, d\Gamma \quad \text{eq. 173}$$

$$= (1/V_I) \sum_{k=1}^{s} P_{Ik}^{*}(t) \, \boldsymbol{N}_{Ik} \, l_{Ik} \quad \text{eq. 174}$$

where $\tilde{\boldsymbol{S}}_I(t)$ is the corrected volumetric stress divergence or corrected pressure gradient. The R-H enriched boundary particle velocity, $\dot{u}_{Ik}^{*}$, will be used later in a technique to obtain updated nodal pressures that are consistent with the corrected pressure gradient.

5.3.3 Oscillation control

The numerical solution of shock forming problems is prone to strong oscillation due to Gibbs phenomenon at the shock front; significant solution error can result. Artificial viscosity [26, 59, 60] is commonly used to control shock-induced oscillations; however, subjective length scales and numerical parameters are required. The proposed nonlinear

solids formulation is engendered with an oscillation-limiting feature where the oscillation control is related to formation of the Riemann problem that is embedded in the smoothed volumetric stress divergence correction. In this way oscillation control is directly related to the approximation of Riemann problem pressure and particle velocity initial conditions and avoids subjective length scales and parameters.

Fourier series analysis shows that the solution spectrum for discontinuous approximations contains an infinite series of high frequency terms that localize to the discontinuity as persistent oscillations. In recognition of this source of the oscillation, the pressure approximation in the corrected pressure gradient is utilized as a mechanism to control this error. In the explicit time integration scheme the solution is projected forward in time according to

$$\ddot{\boldsymbol{u}}_I^{n+1} = (1/m_I)\left(\boldsymbol{f}_I^{ext^{n+1}} - \left(\boldsymbol{f}_I^{d^{n+1}} + \boldsymbol{f}_I^{v^{n+1}}\right)\right) \qquad \text{eq. 175}$$

where m_I is the lumped nodal mass, $\boldsymbol{f}_I^{ext}$is the external force vector, $\boldsymbol{f}_I^{d}$ is the internal force vector due to deviatoric stress, and $\boldsymbol{f}_I^{v}$ is the internal force vector related to the corrected pressure gradient. When the standard linear spatial approximation (second-order spatial accuracy) is used to approximate the integration cell boundary pressures required for the smoothed pressure gradient in eq. 165, oscillatory instabilities naturally arise in the pressure gradient solution at a shock. The numerical solution is consequently polluted through oscillation of the volumetric internal force vector in eq. 175. In order to control this error, the Riemann piecewise constant initial conditions and boundary pressure solution are used as

a natural mechanism for oscillation limiting, similar in approach to a Godunov scheme. The C^{-1} approximation of the Riemann problem pressure and particle velocity initial conditions is naturally non-oscillatory in the sense that they cannot form new extrema when projected onto the integration cell boundaries. Furthermore, since the R-H jump equations are used to determine the boundary pressures based on the non-oscillatory C^{-1} projections, the resulting boundary pressures are also non-oscillatory since the R-H equations provide the fundamental jump solution. As a consequence of embedding these conditions into the smoothed pressure gradient construction, the smoothed pressure gradient itself is non-oscillatory and therefore does not contribute to oscillations through eq. 175. In this formulation the treatment for oscillation control is introduced to the pressure gradient and corresponding internal force vector, $\boldsymbol{f}_I^v$. No special treatment is provided for the deviatoric portion due to the pressure-dominated material behavior in the presence of shocks. Implementation and verification testing has validated that the oscillation control provided through the corrected pressure gradient is sufficiently strong to limit oscillations and no additional treatment is required for the shear term.

Accuracy of the integration cell boundary pressure can be improved through the construction of more accurate Riemann problem initial conditions. However, the issue is that at a shock, the higher order projection of initial conditions onto the integration cell boundary can lead to the formation of new extrema and consequently result in solution oscillation. Therefore, if a higher-order projection is used, special measures are required to prevent oscillation; a slope limiter such as the van Leer limiter [122] for finite difference schemes can

be used for this purpose. The essential idea behind the slope limiter is that higher order distribution of the internal field variable is constrained (or limited) so that new extrema are not formed at the cell boundaries. With proper constraint, a higher-order state variable projection can be used while maintaining oscillation control. For this meshfree formulation, the van Leer limiting constraints have been applied to the pressure and particle velocity projections under the SCNI framework. This was accomplished by modifying the Riemann problem initial conditions in Figure 29a according to a linear approximation of the pressure and particle velocity distribution within each of the integration cells. The cell distributions were then modified to satisfy the van Leer constraint conditions, namely that 1) the projected field/state variable value at the boundary does not exceed the nodal value in the adjacent integration cells, 2) piecewise constant distribution is used if the nodal value is a local extremum with respect to the adjacent cells, and 3) piecewise constant distribution is used if the sign of the smoothed gradient differs from that in the adjacent cells. Implementation was limited in this case to a regular discretization; techniques to apply this approach to an irregular meshfree discretization are recommended for future study. Numerical experimentation showed that this approach can be successfully used to obtain higher-order pressure gradient approximations while maintaining the oscillating-limiting feature of the piecewise constant initial conditions. The net result is the improved sharpness of the shock front solution.

5.4 R-H enriched nodal pressure and volumetric strain

For the temporal integration of eq. 159, the nodal accelerations, velocities and displacements are obtained at each time step using the internal force vector built from the corrected volumetric stress divergence and the uncorrected deviatoric part. This provides a complete description of the kinematic field variables; however, an update of the pressure state variable is also required. This research has shown that it is necessary to perform the nodal pressure update at each step in a way that is consistent with the volumetric stress divergence correction. If a consistent pressure update is not provided, significant error can arise in the solution, particularly in the presence of internal boundaries or reflecting surfaces where the reflected waves are driven by the R-H jump conditions.

To construct the consistent nodal pressure update, the R-H enriched boundary particle velocity computed from eq. 171 and eq. 172 is interpreted as a description of the cell boundary deformation (reference Figure 30). The velocity vector at each boundary is obtained from the reconstruction

$$\dot{\boldsymbol{u}}_{Ik}^{*n+1} = \dot{u}_{Ik}^{*} \boldsymbol{N}_{Ik} \qquad \text{eq. 176}$$

where the repeated index k makes reference to the boundary segment and does not indicate a summation. A strain measure is now required that can be related to the R-H enriched cell boundary deformation. This is obtained through the relationship between velocity gradient, $\dot{u}_i(\boldsymbol{X}, t)_{,j}$, and strain rate, $\dot{\epsilon}_{ij}(\boldsymbol{X}, t)$

$$(1/2)\left(\dot{u}_i(\boldsymbol{X},t)_{,j}+\dot{u}_{\boldsymbol{j}}(\boldsymbol{X},t)_{,\boldsymbol{i}}\right)=(1/2)\frac{\partial}{\partial t}\left(\frac{\partial u_i(\boldsymbol{X},t)}{\partial X_j}+\frac{\partial u_{\boldsymbol{j}}(\boldsymbol{X},t)}{\partial X_i}\right)=\dot{\epsilon}_{ij}(\boldsymbol{X},t) \qquad \text{eq. 177}$$

Accordingly, the R-H enriched nodal strain rate is approximated by

$$\dot{\epsilon}_{ij}(\boldsymbol{X},t)\big|_{\boldsymbol{X}_I}\approx\int_{\Omega_I^X}(1/2)\left(\dot{u}_i(\boldsymbol{X},t)_{,j}+\dot{u}_j(\boldsymbol{X},t)_{,i}\right)\varphi(\boldsymbol{X};\boldsymbol{X}-\boldsymbol{X}_I)\,d\Omega\equiv\tilde{\dot{\epsilon}}_{ijI}(t) \qquad \text{eq. 178}$$

where $\varphi(\boldsymbol{X};\boldsymbol{X}-\boldsymbol{X}_I)$ is the piecewise constant kernel defined in eq. 161. Introducing the piecewise constant kernel and applying the divergence theorem, eq. 178 is transformed to

$$\tilde{\dot{\epsilon}}_{ijI}(t)=(1/2V_I)\int_{\Gamma_I^X}\dot{u}_i(\boldsymbol{X},t)N_j+\dot{u}_j(\boldsymbol{X},t)N_i\,d\Gamma \qquad \text{eq. 179}$$

which is evaluated numerically

$$\tilde{\epsilon}_{ijI}^{n+1}=(1/2V_I)\sum_{k=1}^{s}\left(\dot{u}_{iIk}^{*n+1}N_{jIk}+\dot{u}_{jIk}^{*n+1}N_{iIk}\right)l_{Ik} \qquad \text{eq. 180}$$

where $\dot{\boldsymbol{u}}_{Ik}^{*n+1}$ is given in eq. 176. Using the strain rate measure in eq. 180 a measure of the nodal volumetric strain is obtained

$$\tilde{\epsilon}_{iiI}^{n+1}=\tilde{\epsilon}_{iiI}^{n}+\Delta t\,\tilde{\dot{\epsilon}}_{iiI}^{n+1} \qquad \text{eq. 181}$$

where $\tilde{\epsilon}_{iiI}^{n+1}$ is the R-H enriched volumetric strain. Finally, the Rankine-Hugoniot equation relating pressure and volume [86] is introduced

$$P_I^{n+1}=\frac{\rho_I^0 C_b^2(\eta_I^{n+1}-1)\eta_I^{n+1}}{[\eta_I^{n+1}-A(\eta_I^{n+1}-1)]^2} \qquad \text{eq. 182}$$

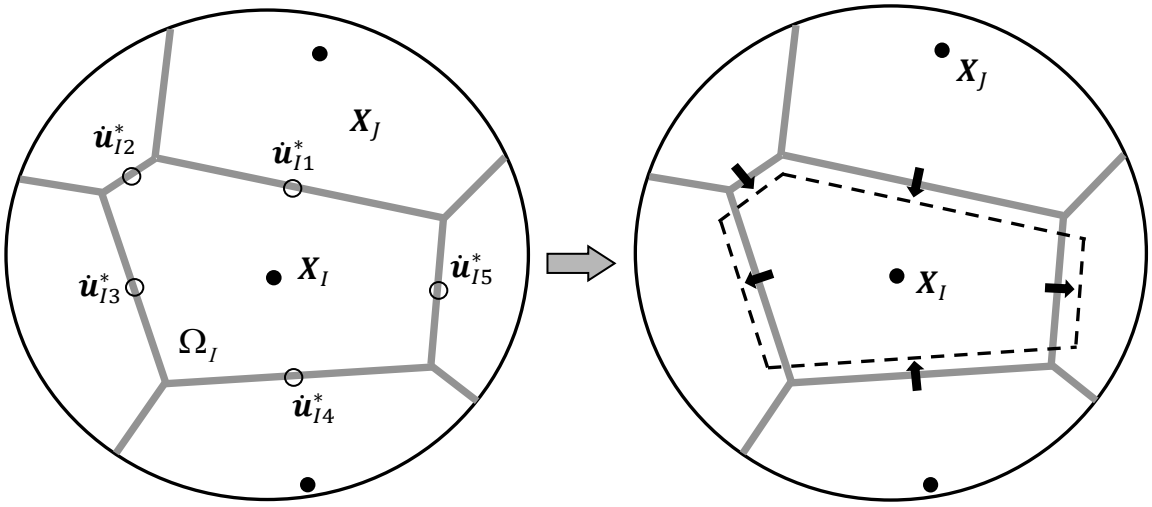

(a) (b)

Figure 30. SCNI integration cell with a) R-H enriched boundary particle velocity at time t^{n+1}, b) boundary motion according to $\dot{\boldsymbol{u}}^*_{Ik}|_{t^{n+1}}$

where

$$\eta_I^{n+1} = \frac{V_I^0}{V_I^0(1+\tilde{\epsilon}_{iiI}^{n+1})} \qquad \text{eq. 183}$$

In eq. 183 η_I^{n+1} is a measure of the volumetric compression at the I^{th} node, which is related to the R-H enriched boundary particle velocity through the R-H enriched nodal strain rate. In eq. 182 P_I^{n+1} is referred to as the R-H enriched nodal pressure update that is consistent with the corrected pressure gradient in eq. 174.

5.5 Natural boundary condition enforcement

To show how surface tractions on the natural boundary are enforced when the volumetric stress divergence correction is used, we begin by considering

$$-\int_{\Omega^X} \delta u_i \rho^0 \ddot{u}_i \, d\Omega + \int_{\Gamma^X} \delta u_i h_i^0 \, d\Gamma + \int_{\Omega^X} \delta u_i \rho^0 b_i \, d\Omega = \int_{\Omega^X} \delta u_{i,j} \sigma_{ij} \, d\Omega \qquad \text{eq. 184}$$

which is obtained from the principle of virtual work. The property that $\delta u_i = 0$ on the essential boundary has not been used, so that the contour integral is written over the entire domain boundary, Γ^X. Decomposing the stress in eq. 184 into volumetric and deviatoric parts gives

$$-\int_{\Omega^X} \delta u_i \rho^0 \ddot{u}_i \, d\Omega + \int_{\Gamma^X} \delta u_i h_i^0 \, d\Gamma + \int_{\Omega^X} \delta u_i \rho^0 b_i \, d\Omega = \int_{\Omega^X} \left(\delta u_{i,j} \sigma_{ij}^d + \delta u_{i,j} \sigma_{ij}^v\right) d\Omega \qquad \text{eq. 185}$$

The domain integral of volumetric stress in eq. 185 is transformed to the stress divergence using integration by parts and the divergence theorem

$$\int_{\Omega^X} \delta u_{i,j} \sigma_{ij}^v d\Omega = \int_{\Omega^X} \left(\delta u_i \sigma_{ij}^v\right)_{,j} d\Omega - \int_{\Omega^X} \delta u_i \sigma_{ij,j}^v \, d\Omega \qquad \text{eq. 186}$$

$$= \int_{\Gamma^X} \delta u_i \sigma_{ij}^v N_j d\Gamma - \int_{\Omega^X} \delta u_i \sigma_{ij,j}^v \, d\Omega \qquad \text{eq. 187}$$

Now substitute eq. 187 into eq. 185 to obtain

$$-\int_{\Omega^X} \delta u_i \rho^0 \ddot{u}_i \, d\Omega + \int_{\Gamma^X} \delta u_i h_i^0 \, d\Gamma + \int_{\Omega^X} \delta u_i \rho^0 b_i \, d\Omega = \int_{\Omega^X} \delta u_{i,j} \sigma_{ij}^d d\Omega + \int_{\Gamma^X} \delta u_i \sigma_{ij}^v N_j d\Gamma - \int_{\Omega^X} \delta u_i \sigma_{ij,j}^v \, d\Omega \qquad \text{eq. 188}$$

which is re-arranged to give

$$-\int_{\Omega^X}\delta u_i\rho^0\ddot{u}_i\,d\Omega+\left\{\int_{\Gamma^X}\delta u_i h_i^0\,d\Gamma-\int_{\Gamma^X}\delta u_i\sigma_{ij}^v N_j d\Gamma\right\}+$$
$$\int_{\Omega^X}\delta u_i\rho^0 b_i\,d\Omega=\int_{\Omega^X}\delta u_{i,j}\sigma_{ij}^d d\Omega-\int_{\Omega^X}\delta u_i\sigma_{ij,j}^v\,d\Omega \qquad \text{eq. 189}$$

The eq. 189 is a modified form of the variational equation in eq. 184 that has separated the internal forces due to shear, $\int_{\Omega^X}\delta u_{i,j}\sigma_{ij}^d d\Omega$, and volumetric stress, $\int_{\Omega^X}\delta u_i\sigma_{ij,j}^v\,d\Omega$. However, in separating the internal force components and transforming to the volumetric stress divergence, an additional surface traction, $\int_{\Gamma^X}\delta u_i\sigma_{ij}^v N_j d\Gamma$, was created that must be addressed. To address this surface traction term through the volumetric stress divergence correction, an approximation for the volumetric stress divergence is defined as

$$\sigma_{ij,j}^v\approx(1/V)\int_{\Omega^X}\sigma_{ij,j}^v\,d\Omega\equiv\widetilde{\mathbb{S}}_i \qquad \text{eq. 190}$$

which is the same as the smoothed volumetric stress divergence in eq. 162. Using the divergence theorem, eq. 190 is transformed to

$$\widetilde{\mathbb{S}}_i=(1/V)\int_{\Gamma^X}\sigma_{ij}^v N_j\,d\Gamma \qquad \text{eq. 191}$$

Now consider that the domain, Ω^X, can be decomposed into a series of conforming sub-domains, $\{\Omega_I^X\}_{I=1}^{np}$. Each sub-domain is bounded by Γ_I^X, which is composed of $\Gamma_I^X=\Gamma_I^{int}\cup\Gamma_I^{ext}$, where Γ_I^{ext} is the portion of Γ_I^X intersecting the boundary $\partial\Omega^X$ and Γ_I^{int} is the portion internal to Ω^X. Letting $\varrho^{int}=\cup\,\Gamma_I^{int}$ and $\varrho^{ext}=\cup\,\Gamma_I^{ext}$, eq. 191 can be written as

$$\widetilde{\mathbb{S}}_i=\widetilde{\mathbb{S}}_i^{int}+\widetilde{\mathbb{S}}_i^{ext}=(1/V)\left[\int_{\varrho^{int}}\sigma_{ij}^v N_j\,d\Gamma+\int_{\varrho^{ext}}\sigma_{ij}^v N_j\,d\Gamma\right] \qquad \text{eq. 192}$$

If the sub-domains are conforming and σ_{ij}^v computed on the internal boundaries, ϱ^{int}, is

consistent, then $\int_{\varrho^{int}} \sigma_{ij}^{v} N_j \, d\Gamma = 0$ so that eq. 192 recovers eq. 191 for $\varrho^{ext} \equiv \Gamma^X$. The virtual work of the volumetric stress divergence approximation is considered by applying an arbitrary perturbation to eq. 190

$$\delta u_i \sigma_{ij,j}^{v} \approx \delta u_i \widetilde{\mathbb{S}}_i = \delta u_i \widetilde{\mathbb{S}}_i^{int} + (1/V) \int_{\varrho^{ext}} \delta u_i \sigma_{ij}^{v} N_j \, d\Gamma \qquad \text{eq. 193}$$

where the decomposition in eq. 192 was used. Integrating eq. 193 over the domain Ω^X obtain

$$\int_{\Omega^X} \delta u_i \sigma_{ij,j}^{v} \, d\Omega \approx \int_{\Omega^X} \delta u_i \widetilde{\mathbb{S}}_i^{int} \, d\Omega + \int_{\Omega^X} \left((1/V) \int_{\varrho^{ext}} \delta u_i \sigma_{ij}^{v} N_j \, d\Gamma \right) d\Omega \qquad \text{eq. 194}$$

Now consider that

$$\int_{\Omega^X} \left((1/V) \int_{\varrho^{ext}} \delta u_i \sigma_{ij}^{v} N_j \, d\Gamma \right) d\Omega = (1/V) \int_{\varrho^{ext}} \delta u_i \sigma_{ij}^{v} N_j \, d\Gamma \int_{\Omega^X} \, d\Omega \qquad \text{eq. 195}$$

$$= \int_{\varrho^{ext}} \delta u_i \sigma_{ij}^{v} N_j \, d\Gamma \qquad \text{eq. 196}$$

because the contour integral solely exists on $\partial\Omega^X$ and therefore is constant with respect to the domain integral over Ω^X. Substituting eq. 196 into eq. 194 gives

$$\int_{\Omega^X} \delta u_i \sigma_{ij,j}^{v} \, d\Omega \approx \int_{\Omega^X} \delta u_i \widetilde{\mathbb{S}}_i^{int} \, d\Omega + \int_{\varrho^{ext}} \delta u_i \sigma_{ij}^{v} N_j \, d\Gamma \qquad \text{eq. 197}$$

which can be used in eq. 189 to obtain

$$-\int_{\Omega^X} \delta u_i \rho^0 \ddot{u}_i \, d\Omega + \left\{ \int_{\Gamma^X} \delta u_i h_i^0 \, d\Gamma - \int_{\Gamma^X} \delta u_i \sigma_{ij}^{v} N_j d\Gamma \right\} + \int_{\Omega^X} \delta u_i \rho^0 b_i \, d\Omega = \int_{\Omega^X} \delta u_{i,j} \sigma_{ij}^{d} d\Omega - \int_{\Omega^X} \delta u_i \widetilde{\mathbb{S}}_i^{int} \, d\Omega - \int_{\Gamma^X} \delta u_i \sigma_{ij}^{v} N_j \, d\Gamma \qquad \text{eq. 198}$$

where $\varrho^{ext} \equiv \Gamma^X$ was used. The key result of eq. 198 is that by introducing the smoothed divergence approximation, the volumetric stress divergence is decomposed into a domain

integral, $\int_{\Omega^X} \delta u_i \widetilde{\mathbb{S}}_i^{int}\, d\Omega$, and a contour integral, $\int_{\Gamma^X} \delta u_i \sigma_{ij}^{v} N_j\, d\Gamma$. The contour integral formed through the smoothed divergence approximation cancels with the extra surface traction term in eq. 189 so that the correct surface traction is approximately recovered. The domain integral from the smoothed divergence approximation remains and is consistent in the sense that the integral is a domain integral and $\widetilde{\mathbb{S}}_i^{int}$ is evaluated only on ϱ^{int}, which is contained within Ω^X. Letting $\widetilde{\mathbb{S}}_i^{int} \equiv \tilde{S}_i$ and multiplying through by -1 in eq. 198 obtain

$$\int_{\Omega^X} \delta u_i \rho^0 \ddot{u}_i\, d\Omega + \int_{\Omega^X} \delta u_{i,j} \sigma_{ij}^{d} d\Omega - \int_{\Omega^X} \delta u_i \tilde{S}_i\, d\Omega - \int_{\Gamma^X} \delta u_i h_i^0\, d\Gamma - \int_{\Omega^X} \delta u_i \rho^0 b_i\, d\Omega = 0 \qquad \text{eq. 199}$$

which is equivalent to the corrected Galerkin approximation in eq. 159 when the test and trial function approximations are introduced.

5.6 Jump equation, description of smooth waves

In the proposed hydrodynamic formulation, the corrected volumetric stress divergence is applied to the full problem domain that may contain strong shocks, weak shocks, elastic discontinuities or smooth waves. As such, it is important to show that the corrected volumetric stress divergence, which derives from the Rankine-Hugoniot jump equation, can be applied to smooth waves as well as shocks. Davison [86] has shown how the pressure-particle velocity Hugoniot in eq. 169 can be used to describe the change in pressure and particle velocity across these different types of waves. Noting that the volumetric stress

divergence correction is used for the pressure-dependent response of the material, consider the following balance equation for linear momentum for a fluid

$$\partial P/\partial X - \rho_R(\partial \dot{u}/\partial t) = 0 \qquad \text{eq. 200}$$

Also consider the general form of the solution to the one-dimensional linear elastic wave equation

$$u(X,t) = f(X - Ct) + f(X + Ct) \qquad \text{eq. 201}$$

where C is the elastic wave speed. For a wave propagating in the positive X direction, eq. 201 simplifies to

$$u(X,t) = u(Z) \qquad \text{eq. 202}$$

where

$$Z = X - Ct \qquad \text{eq. 203}$$

A simple smooth wave that can be described by eq. 202 is shown in Figure 31, where two points are denoted at Z_1 and Z_2, which have particle velocity and pressure states of $\dot{u}_1$, P_1, $\dot{u}_2$, and P_2. Applying the chain rule to eq. 202, the displacement gradient is obtained

$$\frac{\partial u}{\partial X} = \frac{\partial u}{\partial Z} \qquad \text{eq. 204}$$

The particle velocity is also obtained from eq. 202

$$\dot{u} = \frac{\partial u}{\partial t} = -C\frac{\partial u}{\partial Z} \qquad \text{eq. 205}$$

which is used to obtain

$$\frac{\partial \dot{u}}{\partial t} = \frac{\partial}{\partial t}\left(-C\frac{\partial u}{\partial Z}\right) = -C\frac{\partial}{\partial Z}\left(\frac{\partial u}{\partial t}\right) = -C\frac{\partial}{\partial Z}(\dot{u}) = -C\frac{\partial \dot{u}}{\partial Z} \qquad \text{eq. 206}$$

Recognizing that $P \equiv P\big(u(Z)\big)$, the chain rule can be used to define the pressure gradient

$$\frac{\partial P}{\partial X} = \frac{\partial P}{\partial u}\frac{\partial u}{\partial Z}\frac{\partial Z}{\partial X} = \frac{\partial P}{\partial Z} \qquad \text{eq. 207}$$

Now using eq. 206 and eq. 207 into eq. 200 the following is obtained

$$\frac{\partial}{\partial Z}\big(P(Z) + \rho_R C\dot{u}(Z)\big) = 0 \qquad \text{eq. 208}$$

which is integrated to obtain

$$P(Z) + \rho_R C\dot{u}(Z) + c_1 = 0 \qquad \text{eq. 209}$$

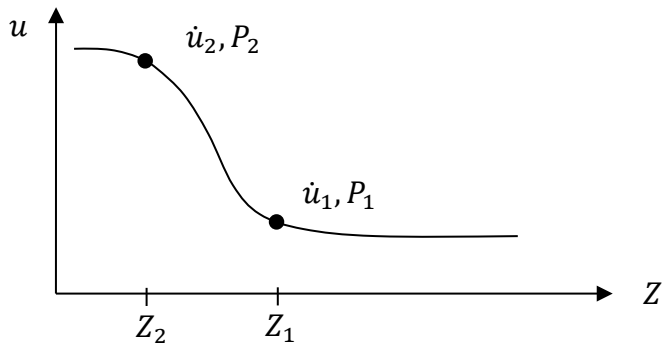

Figure 31. Smooth wave

where c_1 is the integration constant. To determine c_1, eq. 209 is evaluated at the point $Z = Z_1$ to obtain

$$c_1 = -P_1 - \rho_R C \dot{u}_1 \qquad \text{eq. 210}$$

so that eq. 209 is

$$P(Z) + \rho_R C \dot{u}(Z) = P_1 + \rho_R C \dot{u}_1 \qquad \text{eq. 211}$$

Now eq. 211 can be evaluated at the point $Z = Z_2$ to obtain

$$P_2 + \rho_R C \dot{u}_2 = P_1 + \rho_R C \dot{u}_1 \qquad \text{eq. 212}$$

which is re-arranged to give

$$(P_2 - P_1) = \rho_R C (\dot{u}_1 - \dot{u}_2) \qquad \text{eq. 213}$$

The eq. 213 is analogous to eq. 169, but the wave speed is no longer the velocity of the shock discontinuity. Rather, it is the elastic wave speed. This shows that by using the proper wave speed definition, eq. 169 can be used to describe the change in pressure and particle velocity between two points in a smooth wave as well as across a discontinuity.

5.7 Implementation

A flowchart for implementation of the proposed shock modeling enhancements into an explicit meshfree scheme is given in Figure 32. The integration cell topology and RK shape functions are calculated initially and do not require an update, which provides the same

computational efficiency as obtained in a standard SCNI meshfree calculation. During the temporal integration process the SCNI smoothed strains and corresponding stresses are computed, but only the deviatoric portion is assembled into the deviatoric internal force vector. The additional step required for the shock modeling formulation is the solution of the Riemann problem over the integration cell boundaries so that the corrected volumetric stress divergence and consistent update of nodal pressures is obtained. The computational cost associated with this additional step is minimal, since the Riemann problem is cast as a one-dimensional problem aligned with the outward normal of each boundary segment. With the corrected volumetric stress divergence and updated nodal pressures, the nodal accelerations, velocities and displacements are projected forward in time in the same way as a typical explicit central difference formulation.

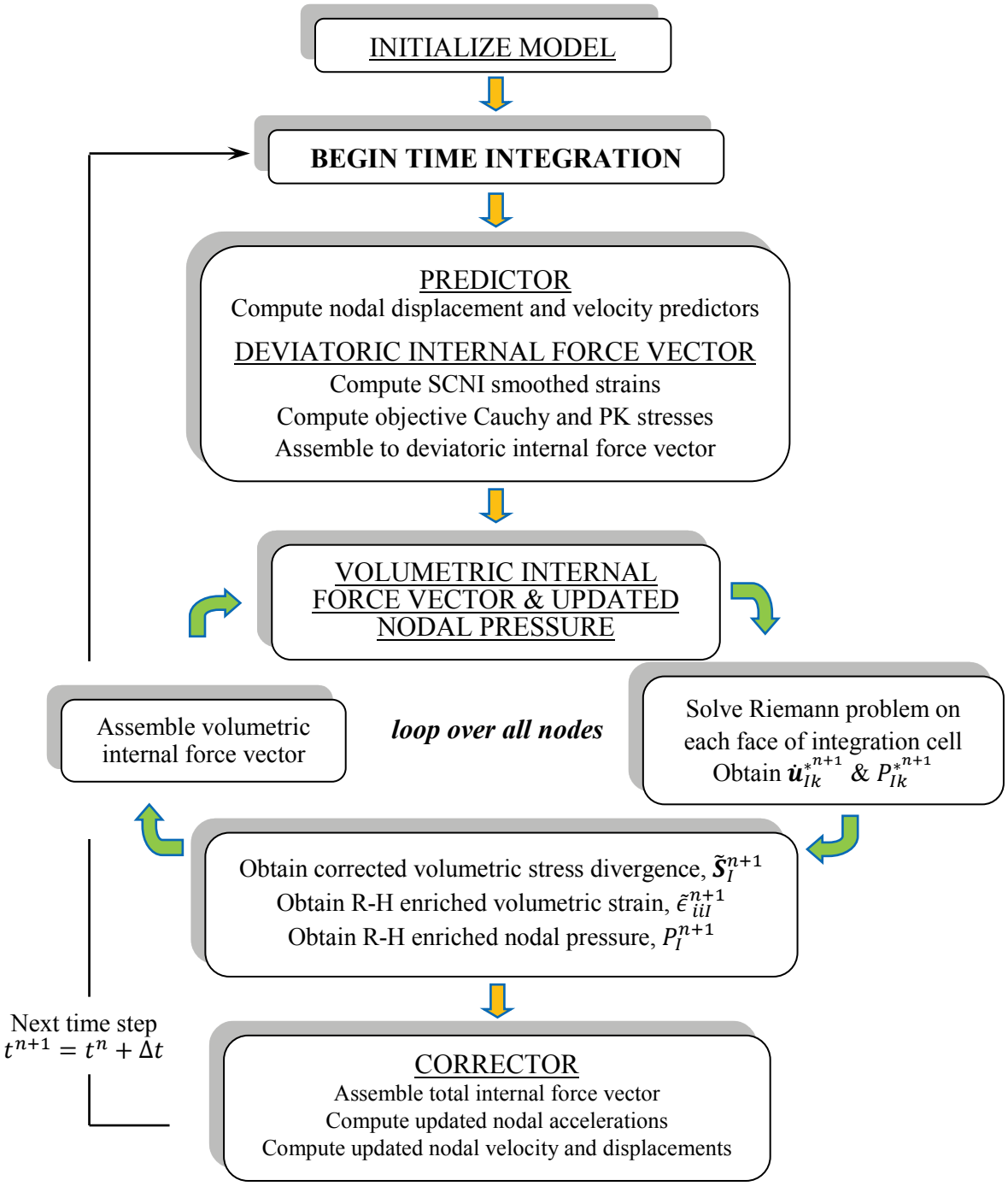

Figure 32. Flowchart, explicit RKPM scheme with shock modeling enhancements

CHAPTER 6 VERIFICATION OF RKPM HYDRODYNAMIC FORMULATION

In this chapter the proposed RKPM hydrodynamic formulation for nonlinear solids is used to solve several benchmark problems for validating the formulation accuracy. The benchmark problems were selected to study performance across a range of shock conditions, including strong shocks due to hypervelocity impact, weak shocks due to low velocity ballistic impact, and elastic shocks due to very low velocity impact. This provides an assessment of the formulation's ability to capture the pressure dominated response of strong shocks and the combined elastic and plastic response of weak shocks. In each case the numerical solutions are compared to analytical solutions or experimental data for quantification of accuracy.

The benchmark problems were selected to simulate flyer plate impact experiments, which are widely used to investigate the high-pressure response of materials when exposed to shock loading. The experiments are typically conducted by firing a projectile sample from a large-bore gun into a stationary target sample. Based on the impact velocity and material properties, shock conditions can vary from weak shocks (characterized by an elastic discontinuity followed by a slower plastic discontinuity) to strong shocks (where the plastic wave velocity is sufficient to overtake the elastic wave and form a single shock front). According to Davison [86], a key experimental feature is the projectile and target geometries,

where the diameter is designed to be several times larger than the thickness. The purpose is to create a plane wave propagating under uniaxial deformation near the center of the specimens, which is where the experimental measurements are made [86]. The diameter of the specimens is large enough to ensure that the experimental measurements are obtained without being influenced by lateral deformation at the edges [86]. In consideration of the uniaxial deformation condition achieved in the experimental setup, the kinematic constraints used in these numerical examples were also based on the assumption of uniaxial deformation. Model problems were constructed as one-dimensional uniaxial strain and two-dimensional plane strain problems, where the two-dimensional problems were constrained with slider boundary conditions to achieve uniaxial deformation for plane wave propagation. A schematic flyer plate experimental setup and corresponding model problem is shown in Figure 33.

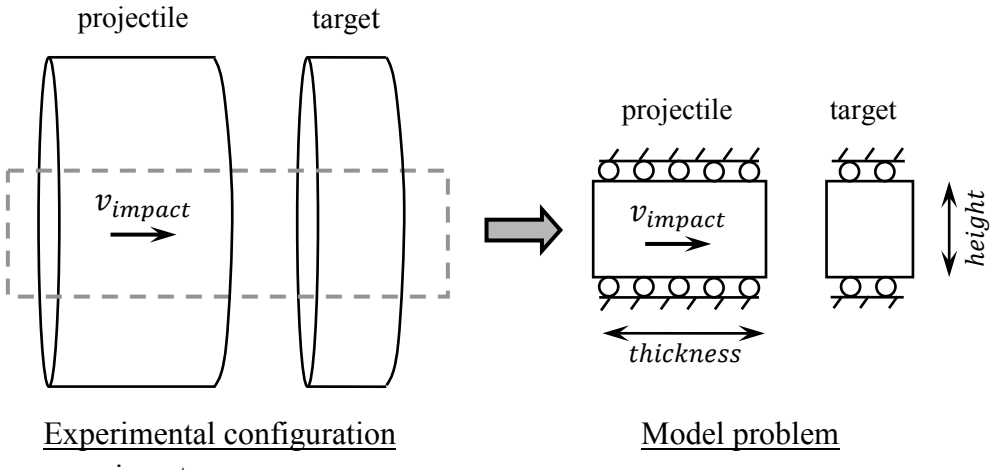

Figure 33. Flyer plate experimental setup and corresponding model problem

The RK approximation in each numerical example was constructed using linear basis and normalized support size of 1.75, where the normalized support is the support size divided by the nodal spacing. The approximation locality was defined according to the power function kernel with a power term $\alpha = 12$. The equation of motion was temporally integrated using an explicit central difference scheme with row summation to form the lumped mass matrix. With linear basis and central difference time integration, the uncorrected RKPM formulation was fully second-order accurate in space and time. The time step for each problem was selected using a Courant number of approximately 0.25. Metallic material was used in all numerical examples, and the material stress-strain response was modeled using a J_2 plasticity constitutive law with objective stress obtained using the Jaumann stress rate. The implementation followed a Total Lagrangian formulation as described in Chapter 5. Deviatoric stress in the undeformed configuration was computed using the first Piola-Kirchoff stress tensor.

The first problem studies the formulation accuracy for hypervelocity impact of an aluminum projectile into an aluminum target plate. Under hypervelocity impact conditions a strong shock is formed that can be compared to an analytical solution. In the second and third example problems a set of flyer plate impact experiments are simulated, and the numerical results are compared to the experimental for validation. The second example follows experiments that were conducted with impact velocities in the ballistic impact regime, so that the numerical results validate the formulation accuracy for weak shock solutions. The third example is similar, but the experimental impact velocities were low

enough so that only elastic waves were generated; this was used to validate the formulation's ability to model elastic discontinuities. In the fourth example a high velocity plate impact is modeled, where the free edges are unconstrained so that the traction free surfaces form rarefaction waves due to lateral deformation at the impact plane. Peak pressure behind the wave is compared to experimental data, and ability of the formulation to capture the plates' lateral deformation and resulting rarefaction wave are evaluated. For all of the example problems the corrected RKPM solutions are compared to the standard uncorrected solution to show the improvements in solution accuracy. All of the example problems were conducted with 6061 T-6 aluminum; material properties are given in Table 1. The properties C_b and A are obtained from flyer plate impact experiments in Marsh [120]. The elastic constants and yield strength were obtained from Lundergan and Herrmann [123].

Table 1. 6061 T-6 aluminum material properties

Property	Value
Density, kg/m^3	2,703
Shear modulus, GPa	28.9
Bulk modulus, GPa	77.5
Tensile yield, MPa	270
C_b, m/s	5350
A	1.34

6.1 Hypervelocity plate impact

In this benchmark problem an aluminum target plate was impacted with an aluminum projectile; impact velocity was 2,000 m/s. The thickness for the model projectile and target was 15 mm and the height of both was 12.5 mm. The model problem was constructed by discretizing the 30 mm × 12.5 mm domain and assigning an initial velocity of 2,000 m/s to the left half. This replicated the contact condition at the moment of impact but avoided the requirement for a contact algorithm. The domain was discretized with 241 nodes in the direction of projectile motion and 101 nodes in the transverse, for a total of 24,341 nodes in the model. Model results using the proposed hydrodynamic formulation are compared to the uncorrected in Figure 34, Figure 35, and Figure 36. The solutions are compared at times of 0.048 μsec, 0.4 μsec, and 1.6 μsec after impact, respectively, and show the progressive propagation of the compression wave away from the impact plane. The peak pressure behind the shock is approximately 19 GPa, which is nearly two orders of magnitude greater than the material's shear strength. This shows how strong shocks cause hydrodynamic behavior in solids. Oscillation in the uncorrected solution is seen immediately after impact in Figure 34. As the solution progresses the uncorrected solution continues to oscillate while the solution from the proposed formulation remains monotone throughout. Furthermore, the jump solution from the proposed formulation remains nearly as sharp as the uncorrected, and could be further sharpened with adaptive refinement at the shock front. In Figure 35 and Figure 36 the uncorrected solution also has a dispersive error that propagates from the domain edges. This dispersive error is due to spurious non-zero energy modes that have been previously

reported by Chen et al. [41]. This error is not observed in the corrected solution, which suggests that the volumetric stress divergence correction provides a control on this error as well. The corrected and uncorrected solutions are compared to the analytical solution at 1.6 μsec in Figure 37a, where the analytical solution was computed according to eq. 169 and eq. 170. The corrected solution is non-oscillatory and closely matches the analytical wave speed and peak pressure. The uncorrected solution exhibits strong oscillatory error, and also shows significant error in the wave speed and shock pressure due to the lack of the essential shock physics in the uncorrected formulation. The corrected solution in Figure 37b was computed using a van Leer limiter [40] to construct the Riemann problem initial conditions; the computed shock front is sharper as a result of increased accuracy in the pressure and particle velocity initial condition approximations.

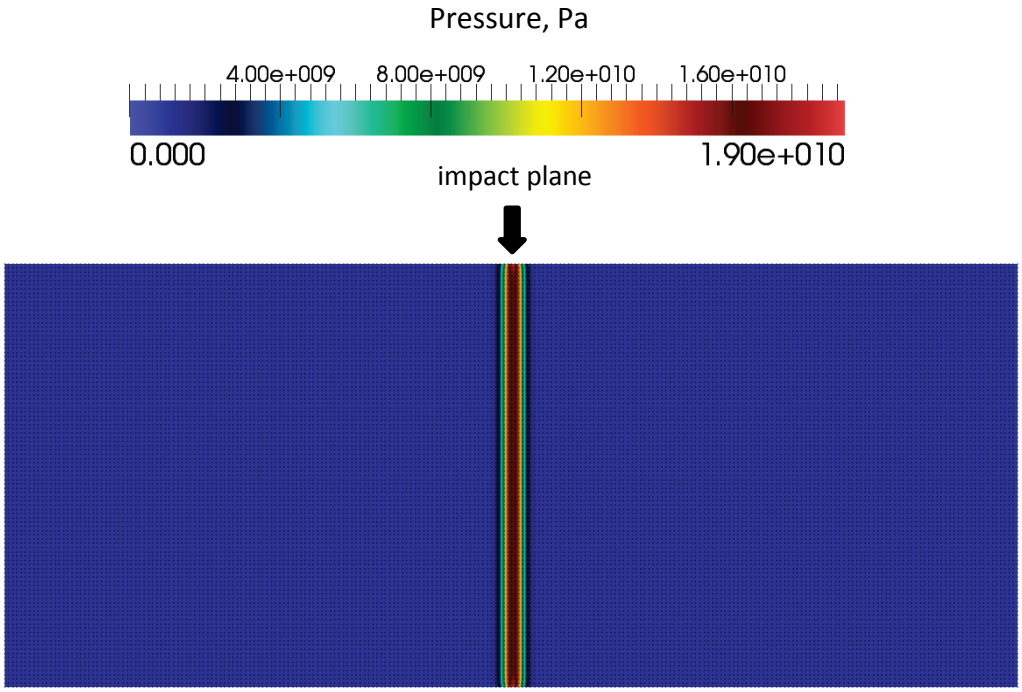

(a)

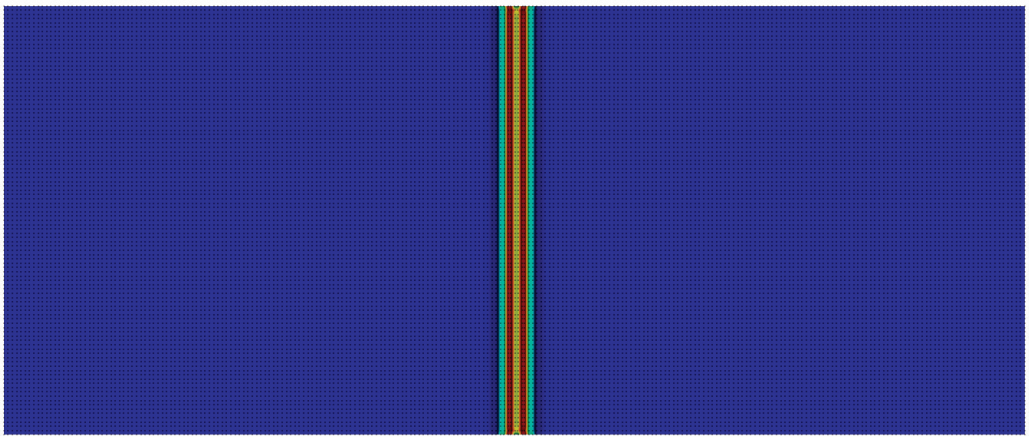

(b)

Figure 34. Hypervelocity impact at 0.048 μsec after impact, solution with a) proposed hydrodynamic formulation, and b) uncorrected formulation

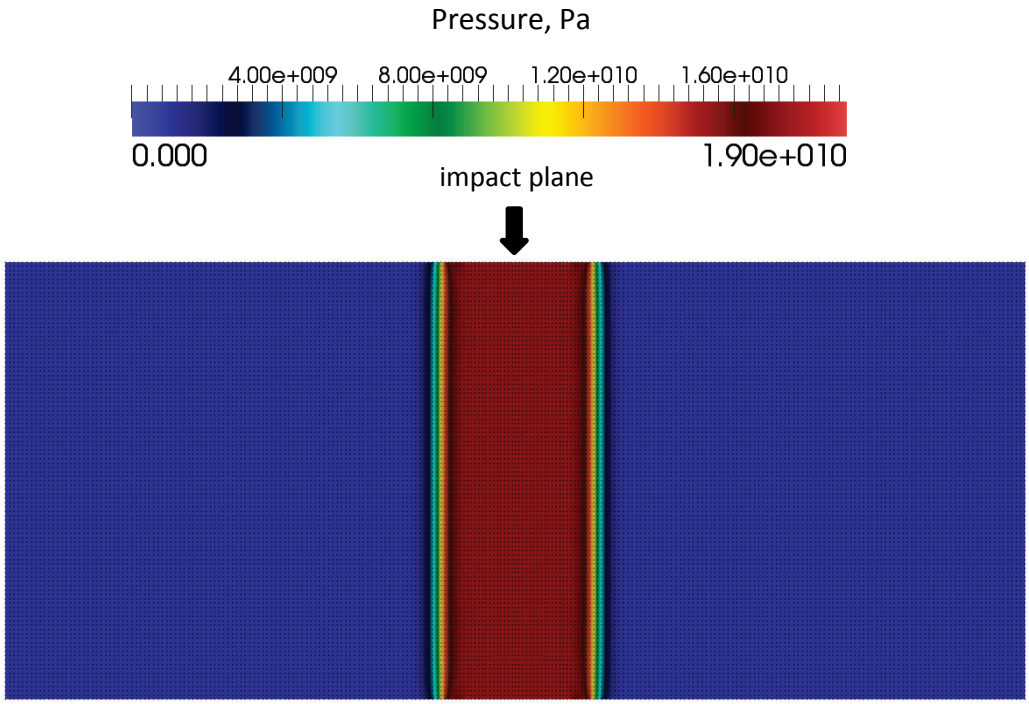

(a)

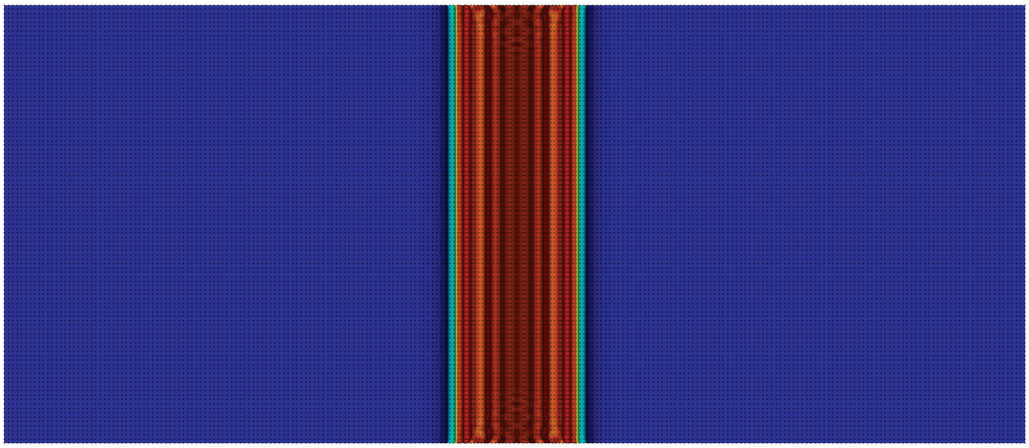

(b)

Figure 35. Hypervelocity impact at 0.400 μsec after impact, solution with a) proposed hydrodynamic formulation, and b) uncorrected formulation

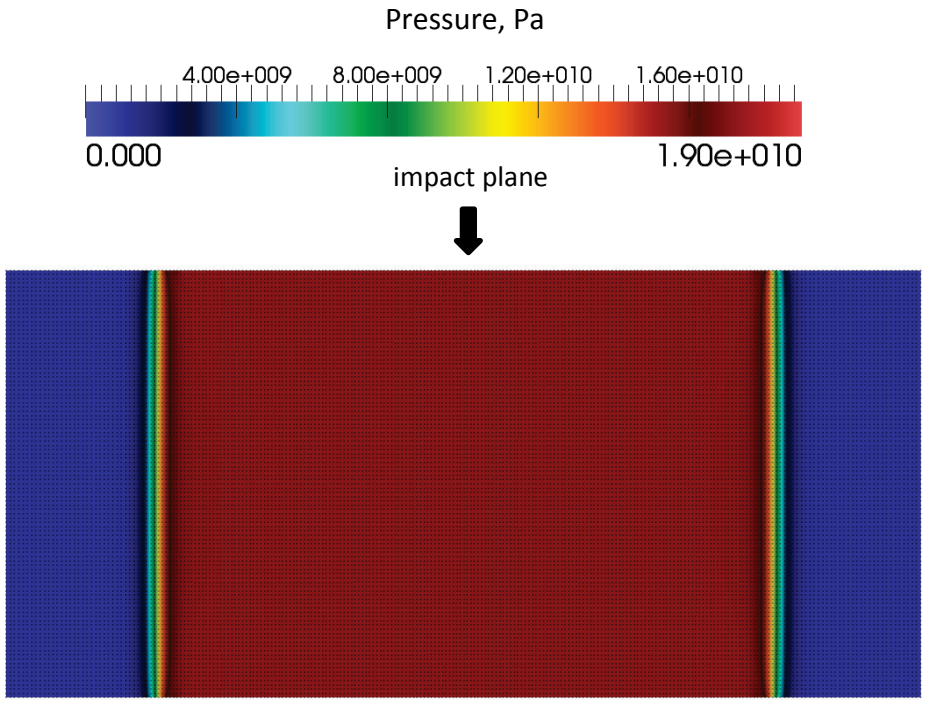

(a)

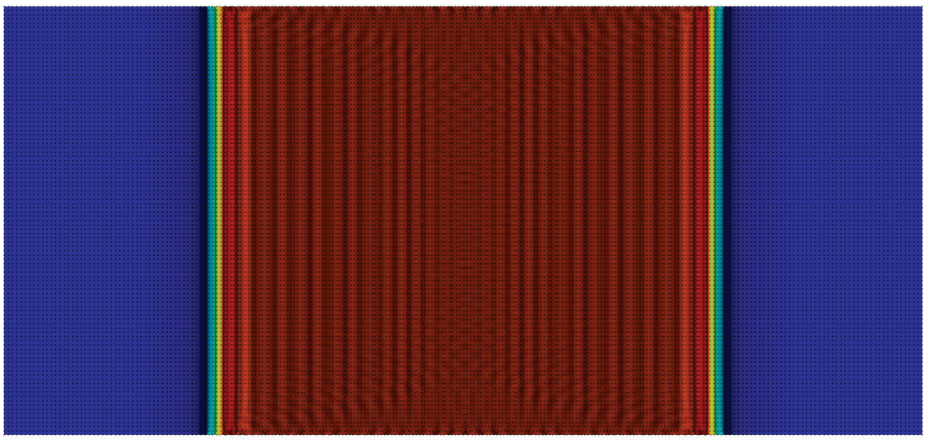

(b)

Figure 36. Hypervelocity impact at 1.6 µsec after impact, solution with a) proposed hydrodynamic formulation, and b) uncorrected formulation

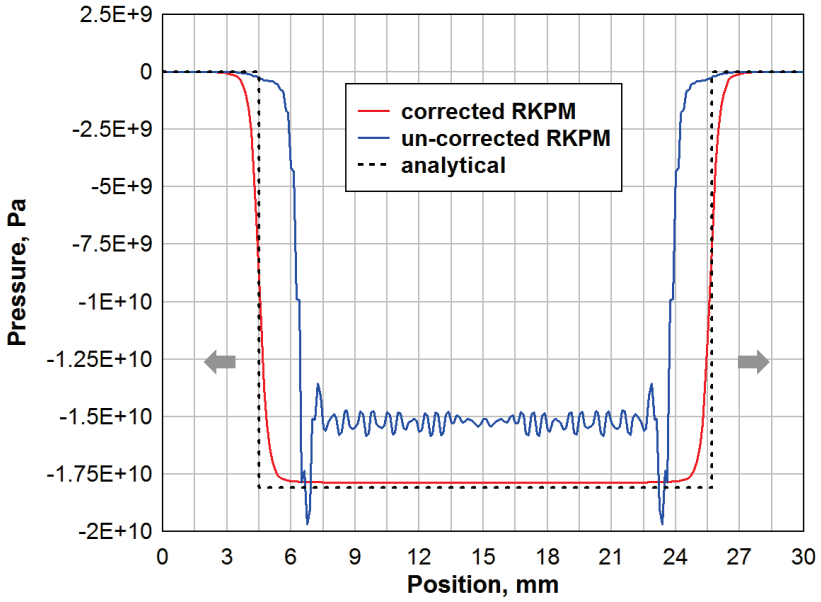

(a)

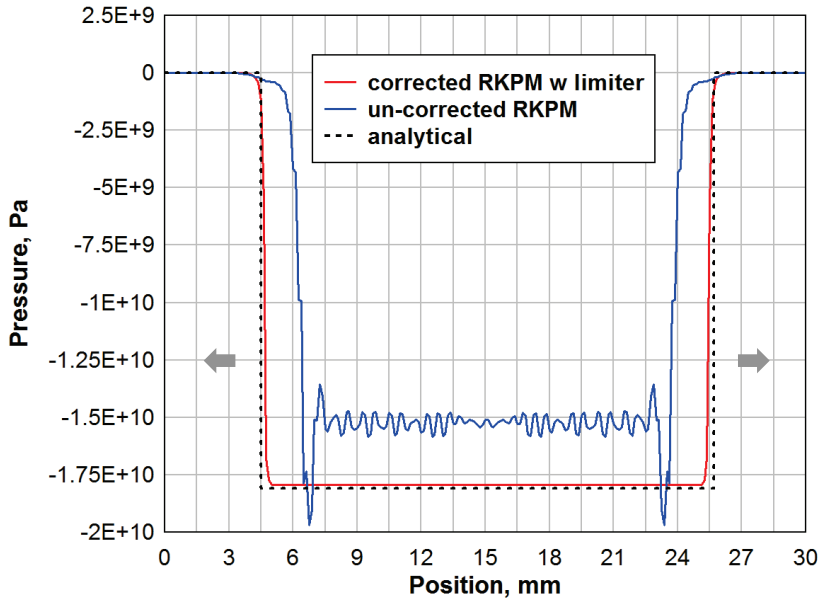

(b)

Figure 37. Hypervelocity impact example, solution comparison at 1.6 μsec using a) piecewise constant Riemann initial conditions, and b) van Leer limiter

6.2 Ballistic velocity impact

For this set of benchmark problems a set of flyer plate impact experiments from Lundergan and Herrmann [123] were modeled. The experiments were conducted at lower impact velocities (< 300 m/s) in the ballistic range to investigate equation of state properties for weak elastic-plastic shocks. These experiments were selected to validate accuracy of the hydrodynamic formulation when weak shocks are present, which can be generated by ballistic impact. The experiments were conducted by firing a 6061 T-6 aluminum impact plate into a target of the same material. Target thicknesses ranged between 12.5 mm and 25 mm. Free surface velocities on the back of the target plates were monitored, and the initial shock velocities (for both the elastic and plastic waves), particle velocities and axial stresses were determined and reported in Lundergan and Herrmann [123]. Three experiments were selected for simulation and are summarized in Table 2. Average values for the shock velocities and elastic axial stress (i.e., yield stress) are also given. The average values are used for comparison to the numerical results in order to reduce the effect of experimental variability in the comparisons.

Table 2. Summary, ballistic velocity impact experiments [123]

Experiment No.	Impact Vel., m/s	Elastic Shock Velocity, m/s	Plastic Shock Velocity, m/s	Elastic Axial Stress, GPa	Plastic Axial Stress, GPa
124	92	6,210	5,560	0.553	0.767
115	150	6,310	5,380	0.720	1.205
108	273	6,220	5,320	0.697	2.097
Average		6,247	5,420	0.657	

To validate formulation accuracy in this ballistic impact range, the initial shock wave propagation in the impact and target plates was computed and compared to the experimental data. The thickness of the model target and impact plates was 15 mm; the model was constructed using a one-dimensional uniaxial strain implementation in accordance with the experimental design for uniaxial plane wave propagation. The domain was discretized with 481 nodes, and the experimental impact velocity was applied over one-half of the domain to replicate the initial conditions at impact. The Riemann problem initial conditions were constructed using the van Leer slope limiter technique [40] in order to increase the fine-scale resolution of the wave structure at the elastic-plastic transition. The computed and experimental axial stress waves at 1.6 μsec after impact are compared in Figure 38 through Figure 40 for impact velocities of 273 m/s, 150 m/s and 92 m/s, respectively. The computed and experimental particle velocities at 1.6 μsec after impact are compared in Figure 41

through Figure 43 for the same impact velocities. Models results with and without the shock modeling correction are given for each of the three impact velocities. In each of the experiments the impact velocity was sufficient to cause the yield strength to be exceeded so that an elastic precursor wave was formed, which was followed by a plastic wave. However, in contrast to the previous hypervelocity impact example, the peak stress did not significantly exceed the yield strength so that a two-step shock was formed. With reduced impact velocity the magnitude of the plastic stress also reduced, so that at an impact velocity of 92 m/s the peak stress only marginally exceeded the yield strength. As a consequence, these problems provided a good test of formulation accuracy for weak shocks. In all three cases the RKPM solution with the shock modeling correction accurately modeled the elastic and plastic wave speeds, the yield stress, and the peak stress behind the plastic wave. For the case with impact velocity of 92 m/s, a refined model with 961 nodes was also used to increase the accuracy in capturing the structure of the small elastic-plastic wave transition. The error in shock wave speed and peak stress was less than 3 percent in all models. In addition to accurately capturing the physics of the weak shock wave formation, the oscillation-limiting mechanism eliminated Gibb's phenomenon oscillations. In comparison, the uncorrected solution showed greater error in the wave speeds and peak stresses, where the error increased with increasing impact velocity. This increased error is expected since the shock wave strength increases with increasing impact velocity, and the shock physics are not accounted for in the uncorrected formulation. The uncorrected solution also oscillated strongly in all cases, with oscillations increasing with increased impact velocity. A final benefit of the proposed shock

modeling correction was observed in the resolution of the shock jump. For both the elastic and plastic jumps, the corrected solution with the van Leer limiter provided a sharper shock discontinuity than the uncorrected and fully second-order accurate solution.

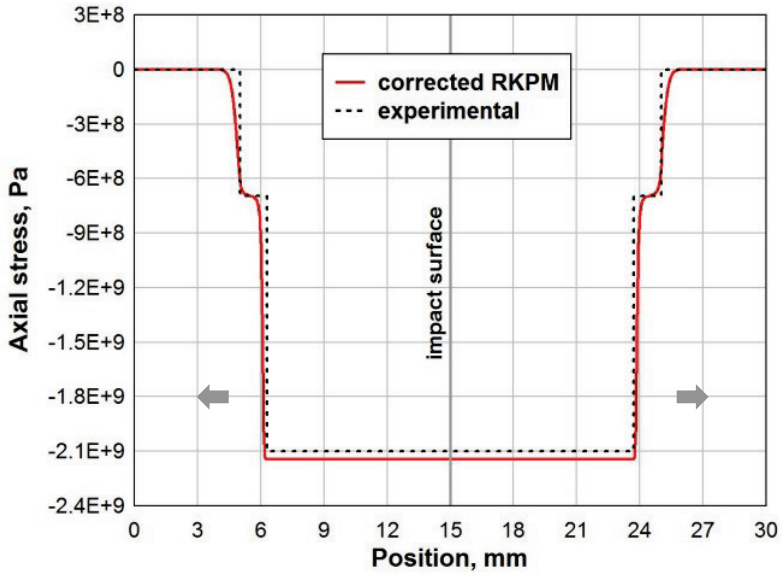

(a)

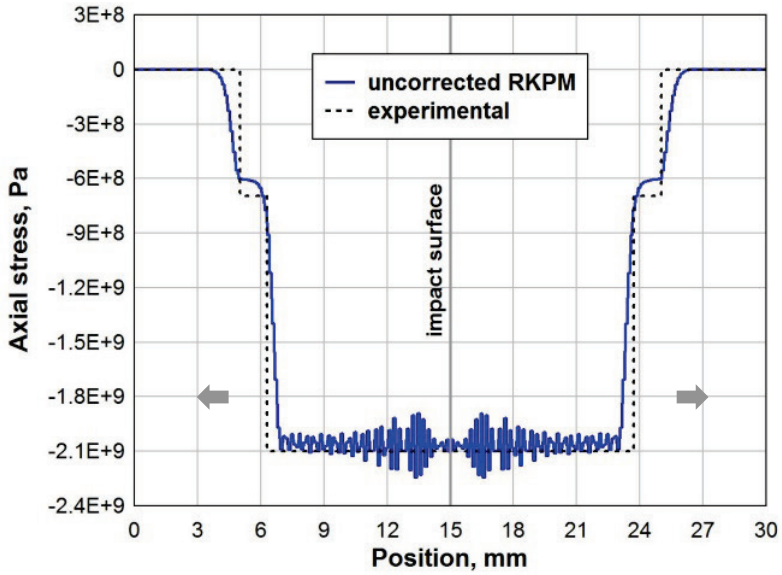

(b)

Figure 38. Ballistic velocity impact, comparison of numerical and experimental axial stress for impact velocity of 273 m/s

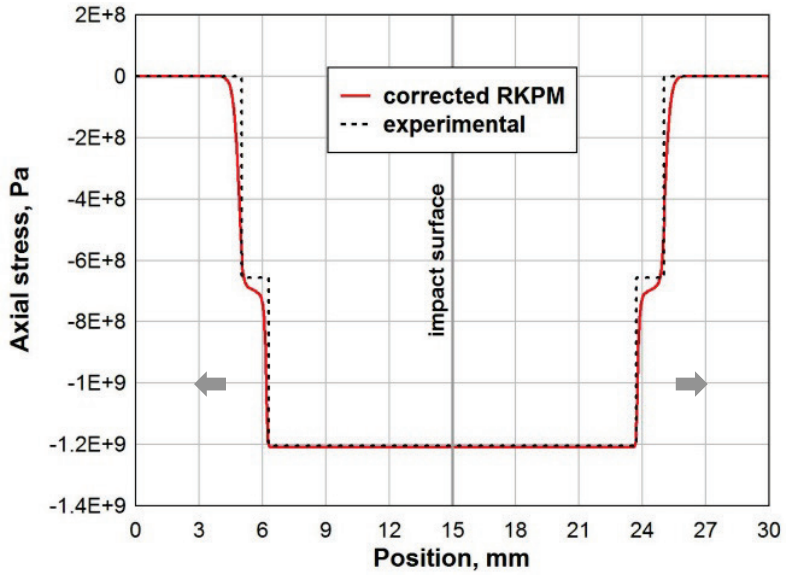

(a)

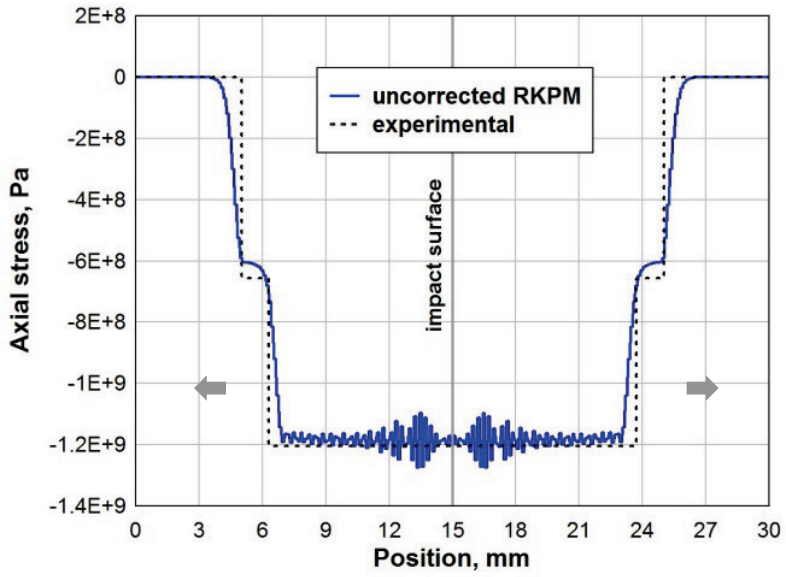

(b)

Figure 39. Ballistic velocity impact, comparison of numerical and experimental axial stress for impact velocity of 150 m/s

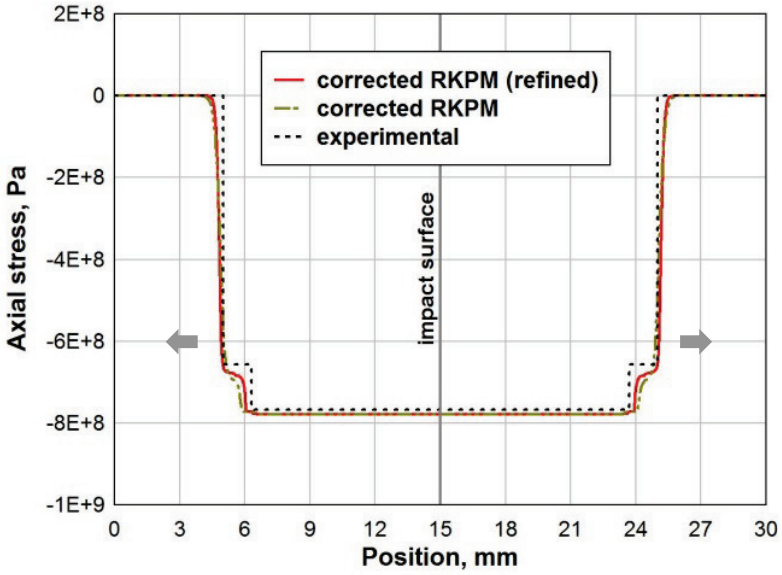

(a)

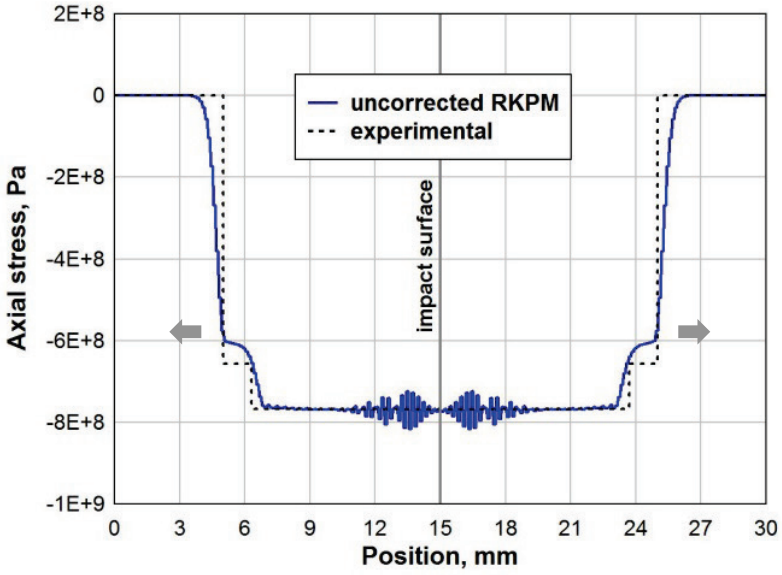

(b)

Figure 40. Ballistic velocity impact, comparison of numerical and experimental axial stress for impact velocity of 92 m/s

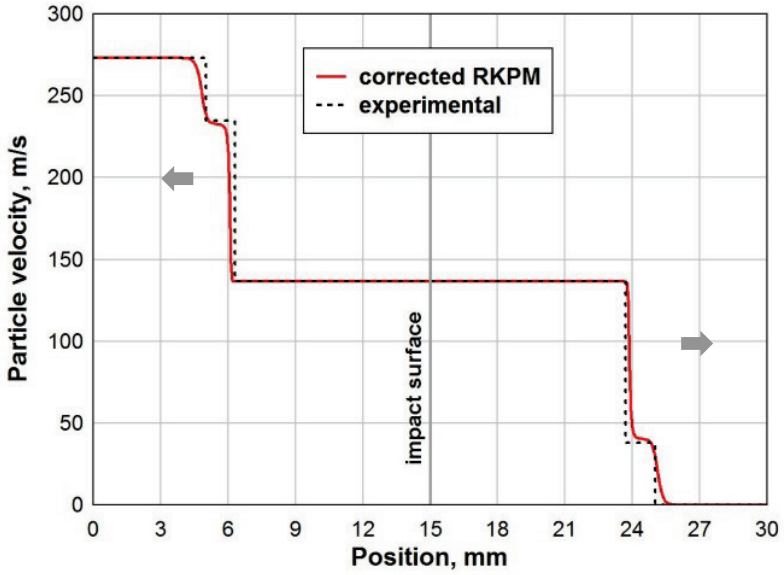

(a)

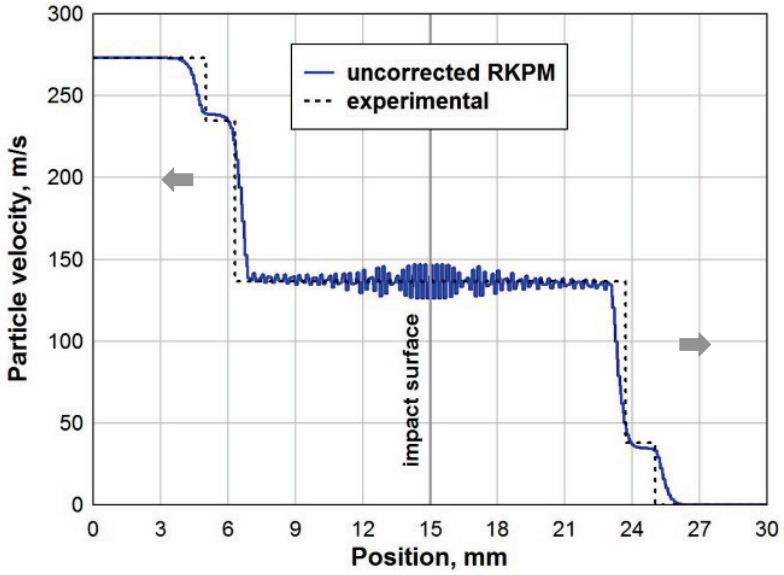

(b)

Figure 41. Ballistic velocity impact, comparison of numerical and experimental particle velocity for impact velocity of 273 m/s

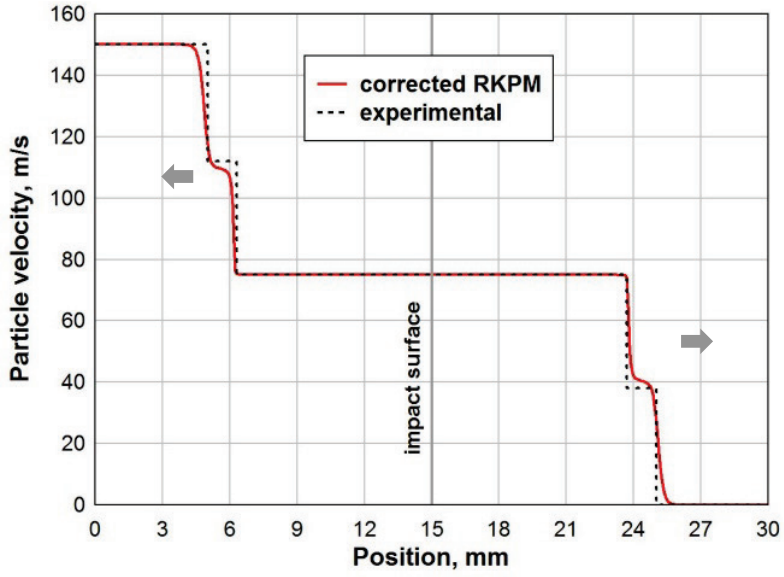

(a)

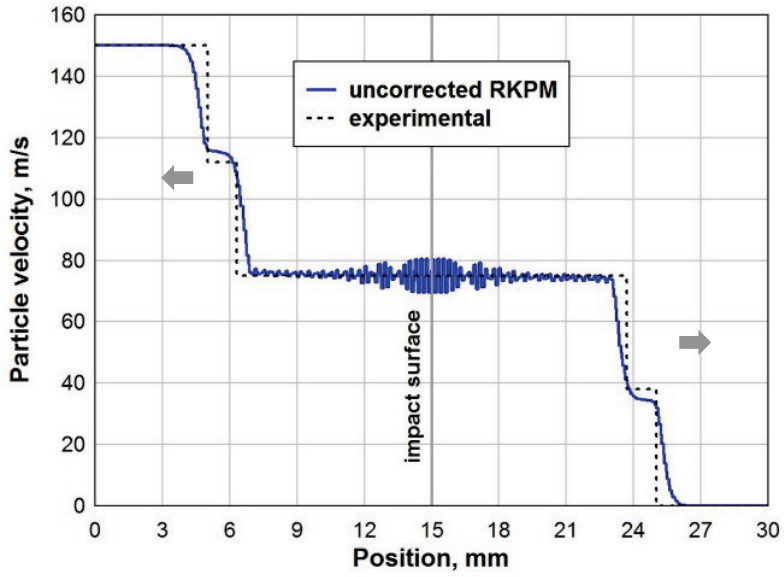

(b)

Figure 42. Ballistic velocity impact, comparison of numerical and experimental particle velocity for impact velocity of 150 m/s

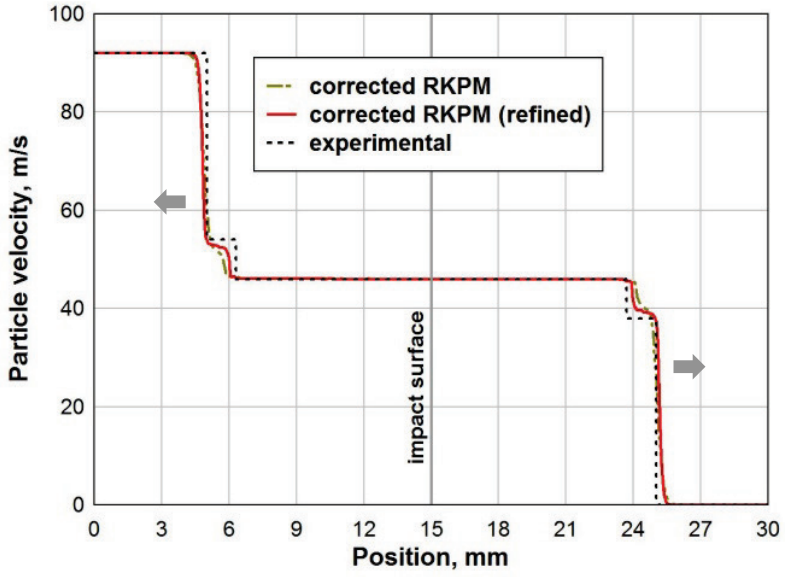

(a)

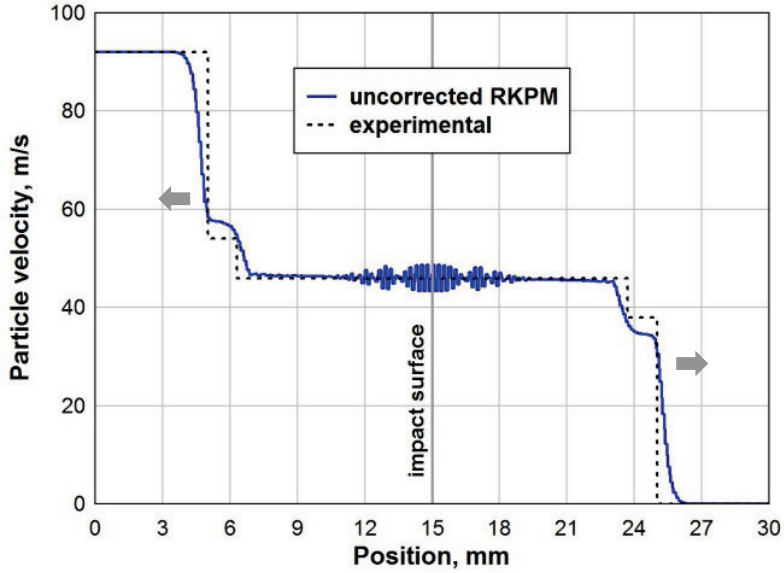

(b)

Figure 43. Ballistic velocity impact, comparison of numerical and experimental particle velocity for impact velocity of 92 m/s

6.3 Elastic impact

In this problem set, another group of flyer plate impact experiments from Lundergan and Herrmann [123] were modeled, where the impact velocities were low enough for the material response to remain in the elastic range. These represent very low velocity impact conditions and were used to verify the proposed formulation accuracy in the presence of an elastic discontinuity. As with the previous example, the experiments were performed by firing a 6061 T-6 aluminum impact plate into a target of the same material. The experimental setup was the same as discussed in the previous verification problem. Two experiments were simulated for the elastic wave case and are summarized in Table 3.

Table 3. Summary, elastic wave impact experiments [123]

Experiment No.	Impact Vel., m/s	Elastic Shock Velocity, m/s	Elastic Axial Stress, GPa
128	29	6,090	0.242
105	53	6,050	0.442

The thickness of the model target and impact plates was 15 mm; the model was constructed using a one-dimensional strain implementation as in the previous example. Each of the experiments was initially modeled using 481 nodes; a refined model using 961 nodes was also used to show solution convergence and the effects of refinement on increased sharpness of the shock front. For these elastic cases it was found that the van Leer limiter

was not strong enough to control the solution oscillation. Consequently, piecewise constant pressure and particle velocity approximations were used in construction of the Riemann problem initial conditions; oscillations were controlled accordingly. The computed and experimental axial stress waves at 1.6 μsec after impact are compared in Figure 44 and Figure 45; models results with and without the shock modeling correction are given for each of the impact velocities. For both experiments, the corrected model provided a close match to the elastic wave speed and peak stress behind the discontinuity. Error in the corrected solution for peak stress and wave velocity was approximately 6 percent and 7 percent, respectively. It is notable that the difference between the experimental and theoretical elastic wave speed (based on the material constants in Table 1) is also approximately 7 percent. Therefore, it is expected that the majority of error is due to variability between the elastic properties used in the model and the exact elastic properties of the experimental material. This is confirmed by comparison to the exact elastic solution for uniaxial wave propagation (also given in the figures), which was computed using the material properties from Table 1. In both of the models, the corrected solution was oscillation free. The uncorrected solution showed similar error in the wave speed and peak stress, which is expected since the elastic solution is not dependent on the strong shock physics. However, the uncorrected solution was also highly oscillatory with a peak stress overshoot of approximately 33 percent. The initial model, with discretization of 481 nodes, provided a reasonably sharp jump, which was sharpened with the model refinement. To further assess the sharpness of the jump solution, the corrected and uncorrected solutions for impact velocity of 29 m/s are compared in Figure

46. The initial model with 481 nodes is compared to the fully second-order accurate solution, and it is seen that the corrected solution is slightly more dissipative due to the reduced accuracy in approximation of the Riemann problem initial conditions. The refined model is also compared to the uncorrected solution and it is seen that the jump sharpness is very nearly the same. This shows that the correction provides significant solution improvement through control of the oscillations, and minimal accuracy is lost through the dissipative effect at the jump. Adaptive *h*-refinement at the jump could be used to further improve the jump sharpness.

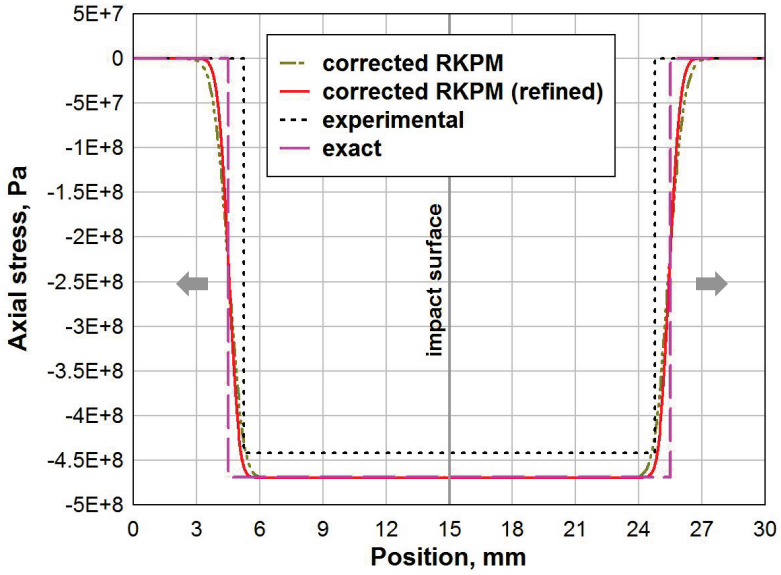

(a)

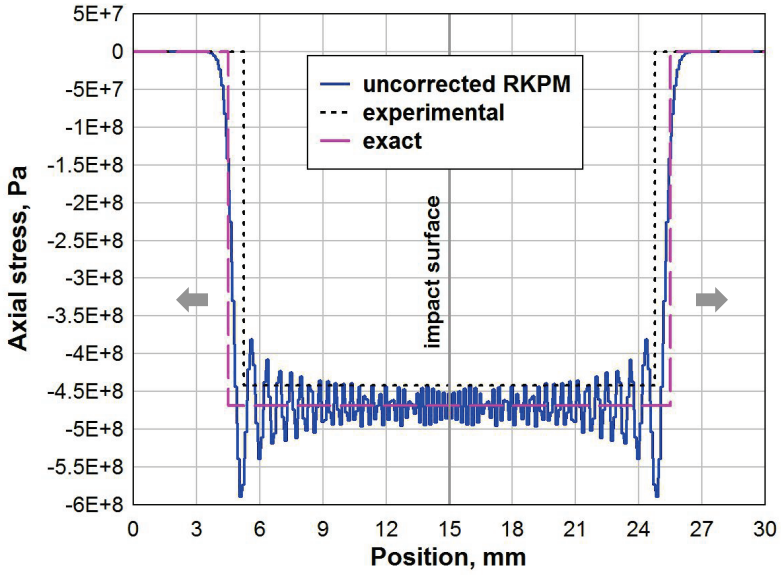

(b)

Figure 44. Elastic impact, comparison of numerical and experimental axial stress for impact velocity of 53 m/s

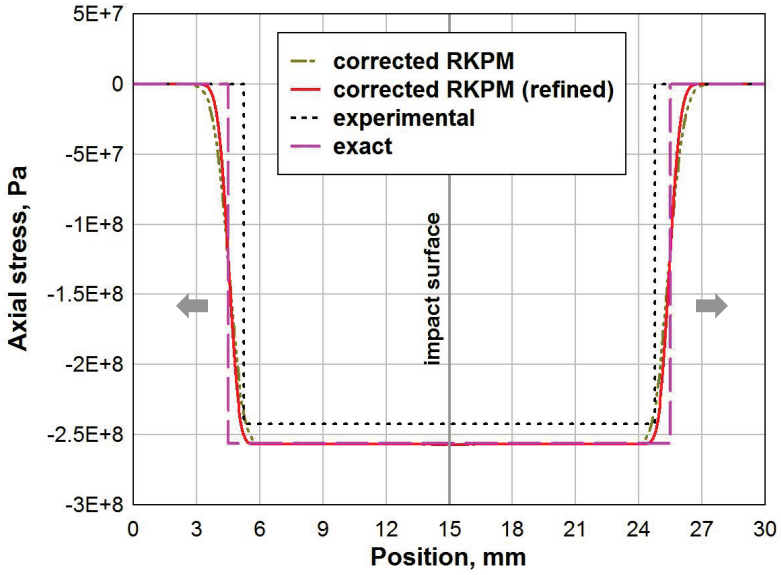

(a)

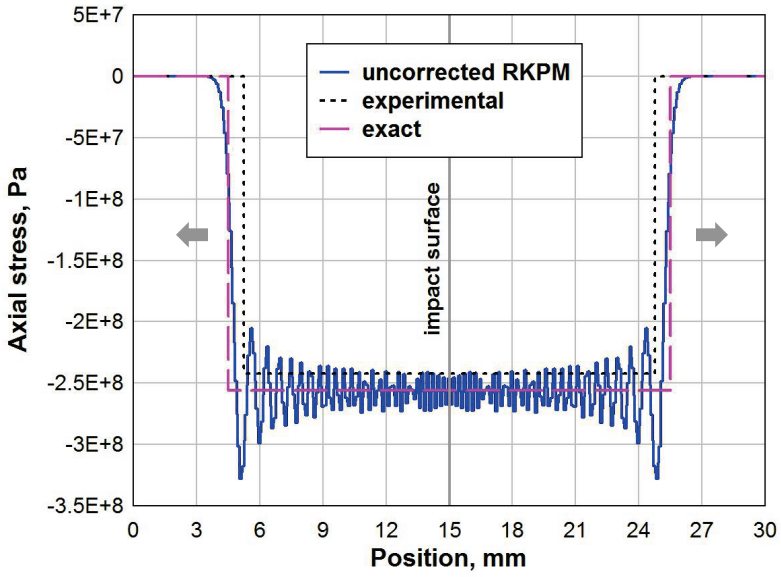

(b)

Figure 45. Elastic impact, comparison of numerical and experimental axial stress for impact velocity of 29 m/s

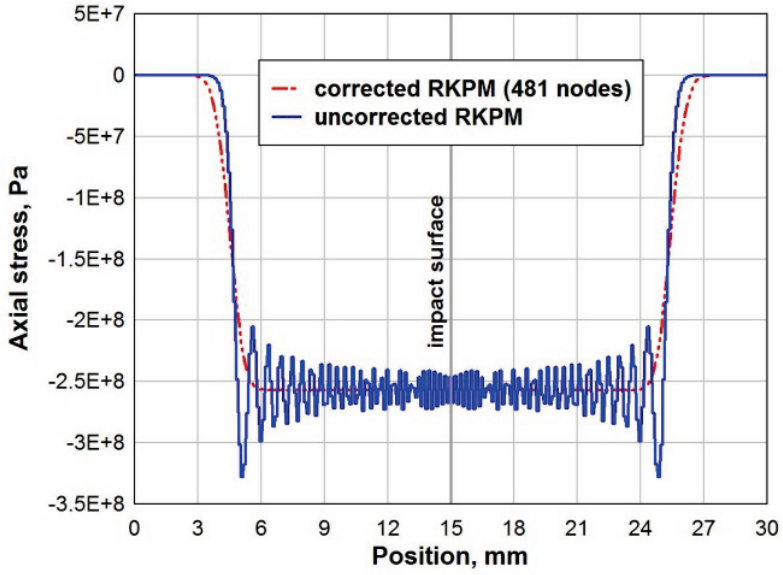

(a)

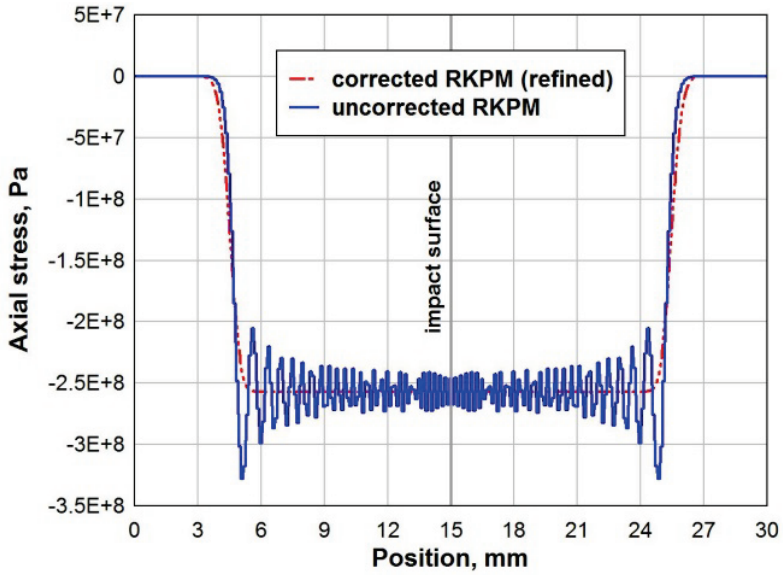

(b)

Figure 46. Comparison of corrected and uncorrected solution dissipation at shock front, a) 481 nodes, and b) 961 nodes.

6.4 High velocity plate impact

In this problem, a 2D plane strain high velocity plate impact problem is considered where the edges are unconstrained to allow lateral deformation at the impact surface. Peak pressure behind the shock wave is compared to the experimental from Marsh [120]. The unconstrained edges result in multi-dimensional wave propagation as the traction free boundary condition generates a rarefaction wave propagating in from the edges. Consequently, this problem assesses the formulation accuracy for multi-dimensional wave propagation and rarefaction formation. The model was constructed as two plates impacting vertically at a velocity of 1,000 m/s; this velocity is typical of a high velocity ballistic impact. Each plate is 8 mm wide by 2 mm thick and was discretized with 161 nodes across the width and 41 nodes through the thickness. All boundaries are unconstrained so that rarefaction waves can form from the traction free edges. Both plates were modeled as 6061 T-6 aluminum with material properties given in Table 1. With an impact velocity of 1,000 m/s, the peak pressure behind the compression shock wave is 8.0 GPa based on data reported in Marsh [120]. Model results for the corrected solution are shown in Figure 47 at 0.04 μsec and 0.24 μsec after impact. The peak pressure behind the compression wave for the corrected solution is 8.0 GPa, which exactly matches the experimental data. The initial compression wave formation is shown in Figure 47a; the formulation correctly enforces the traction free boundary condition as seen at the left and right edges of the impact plane. The wave structure at 0.24 μsec after impact is shown in Figure 47b. The leading compression wave continues to propagate with the initial wave structure while the rarefaction wave grows

from the edges and relieves the pressure in the initially compressed region. This shows why flyer plate experimental data is measured at the center of the material samples and their diameter is much larger than the width; otherwise the measured compression wave would be attenuated by the rarefaction wave. The uncorrected solution at the same time intervals is shown in Figure 48. The uncorrected solution is strongly oscillatory as in previous examples. The corrected and uncorrected peak pressure solutions are compared in Table 4, where the uncorrected peak pressure is 9.0 GPa due to the solution oscillation. This is an approximate 13 percent overshoot of the experimentally determined pressure. Lateral deformation at the impact plane is greater than for the corrected solution, which is a result of the pressure oscillations at the shock front. The uncorrected solution also captures the rarefaction wave propagating from the free surface, but it is polluted due to the oscillations. For the corrected solution, piecewise constant Riemann initial conditions were used. This caused the corrected solution to be slightly more dissipative than the uncorrected, particularly at the corners where the rarefaction wave interacts with the leading compression wave. Use of a technique to improve the initial condition approximation can be used to sharpen the corrected solution.

Table 4. Comparison of shock pressure solutions

Solution	Computed Peak Shock Pressure, GPa	Experimental Shock Pressure, GPa	Error, %
Corrected	8.0	8.0	0
Uncorrected	9.0	8.0	13

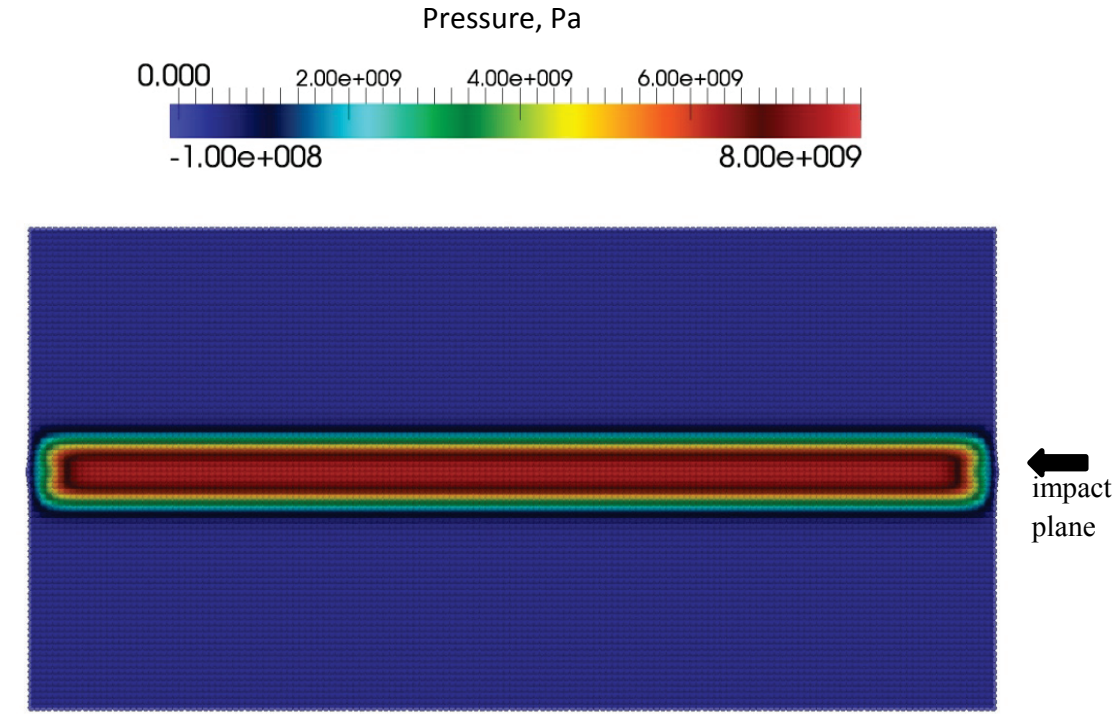

(a)

(b)

Figure 47. High velocity plate impact with edge rarefactions, corrected solution at a) 0.04 μsec and b) 0.24 μsec after impact

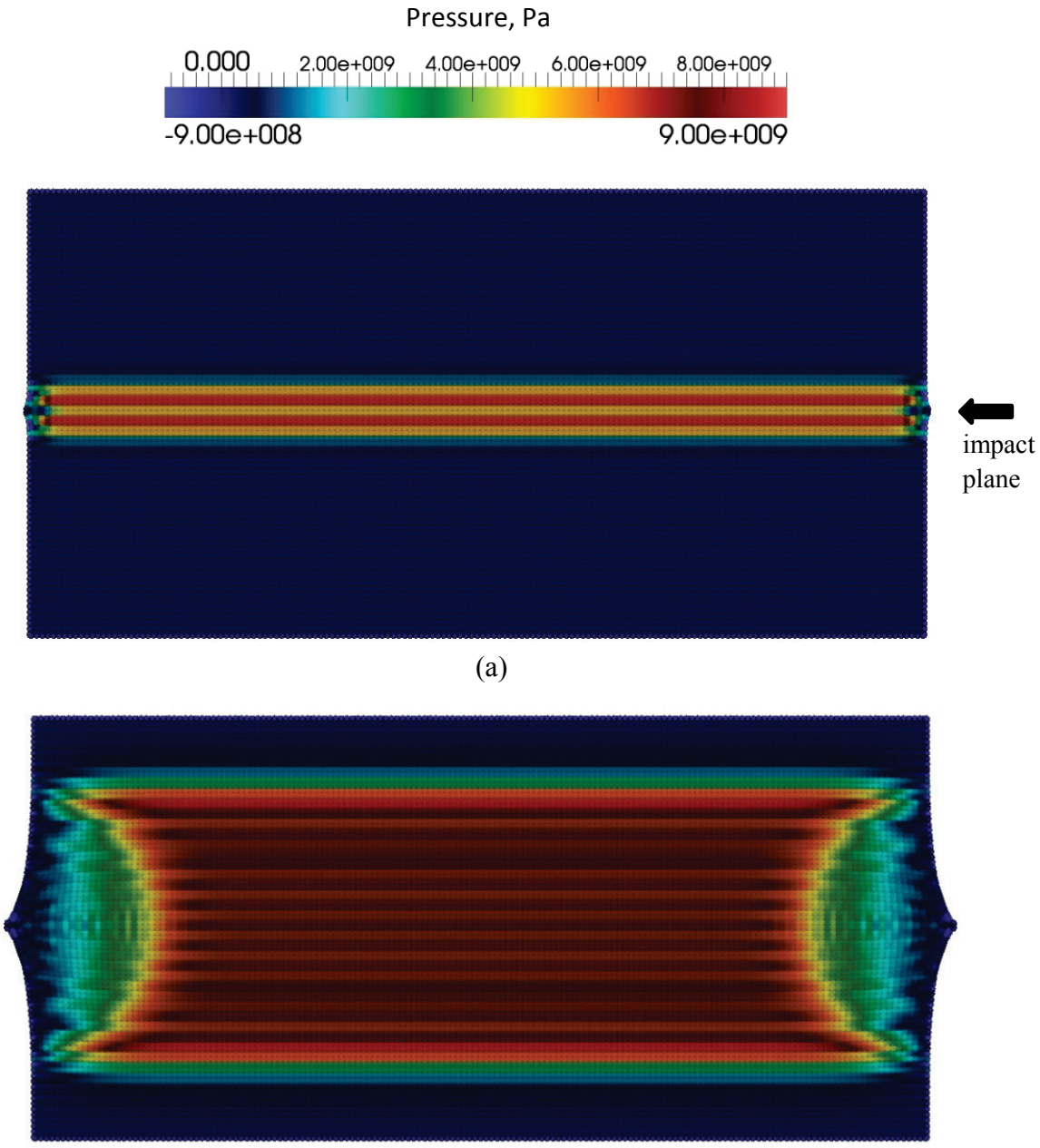

Figure 48. High velocity plate impact with edge rarefactions, uncorrected solution at a) 0.04 μsec and b) 0.24 μsec after impact

CHAPTER 7 CONCLUSIONS AND FUTURE WORK

Many of the current, challenging research and real world problems involve high-rate material response to extreme dynamic loading such as impact and blast, where shock effects play a key role. New meshfree methods are being developed to model this class of problems, and techniques to accurately model the shock-induced hydrodynamic response must be developed in the process. The key issues that must be addressed are appropriate representation of the essential shock physics and control of the oscillatory numerical error that forms at the discontinuity. Neither of these are addressed in a standard numerical formulation for statics or low-rate dynamics, and therefore an enhancement is required to accurately model strong shock effects. Accordingly, the over-arching objective of this research was to develop an approach that addresses both of these issues in a unified manner, so that the RKPM shock modeling accuracy is certified and a strong foundation is developed for future applications.

A powerful attribute of the RK meshfree approximation is the ability to control locality and continuity based on the desired approximation characteristics. Since Gibbs phenomenon occurs as a result of approximation across a discontinuity, the behavior of a new localized power function kernel was investigated for use in problems with discontinuous solutions. Through numerical investigations it was found that the power function kernel provided a

strong localization of the RK approximation, even when enlarged kernel supports were used. The result was reduced oscillatory error in the approximation of a discontinuous solution as compared to approximation results using other smooth kernels such as the cubic B-spline. Another appealing attribute of the power function kernel is that kronecker delta properties are approached with increasing values of the power term, even in the presence of enlarged support size. As a consequence, issues such as imposition of essential boundary conditions and reconstruction of the nodal solutions are simplified when the power function kernel is used.

Towards the development of a shock modeling enrichment, a new approach to model shock-forming scalar conservation laws in the meshfree RKPM framework was first investigated. The essential ingredient is an enrichment of the flux divergence according to a Godunov-type of scheme. The flux divergence enhancement is constructed by forming a smoothed divergence operator on the SCNI integration cell topology and then enriching the divergence operation with a Riemann shock solution. As a consequence of the embedded Riemann problem, the essential physics of the second law of thermodynamics are enforced and the entropy-correct shock solution is obtained. Oscillation control is also tied to the enriched flux divergence through a velocity corrector, which was termed the flux-corrected velocity. The flux corrected velocity is a first-order velocity correction that is embedded with the Riemann-enriched flux divergence and is locally applied at the shock. Localization of the corrector is achieved with an automatic shock detection algorithm so that the solution at the shock front is corrected while regions of smooth solution remain uncorrected and thus

higher order accurate. Numerical examples showed that the uncorrected RKPM solution exhibited large oscillatory errors in the presence of shocks. The corrected RKPM solution on the other hand provided a significant improvement by achieving non-oscillatory behavior at the shock front and accurately capturing both the shock speed and jump solution.

The framework developed for scalar conservation laws was extended to Cauchy's equation of motion to achieve a hydrodynamic formulation for modeling shocks in nonlinear solids. Because the shock response of solids is inherently pressure dominated, in the nonlinear solids formulation a volumetric-deviatoric decomposition of the internal force vector was utilized to construct a shock modeling correction that operates on the pressure part. The correction is formed by enriching the volumetric stress divergence (or equivalently the pressure gradient) with a Rankine-Hugoniot solution to a Riemann problem. The Riemann problem solves for the jump solution of pressure and particle velocity on the SCNI integration cell boundaries, and therefore takes advantage of the existing topologic structure used for weak form integration. The essential shock physics are introduced through the Rankine-Hugoniot enrichment so that the correct nonlinear shock response is obtained. The mechanism for oscillation control is also linked to the Rankine-Hugoniot enrichment through the state and field variable approximations used to define the Riemann problem initial conditions. Through numerical examples, it was shown that resolution of the fine-scale shock structure can be controlled through the accurate treatment of the approximated initial conditions. Other techniques such as adaptive *h*-refinement at the shock front can also be used, where the adaptive refinement is activated by the automatic shock detection algorithm.

An important finding of the research was the requirement for consistency between the nodal pressures and the enriched pressure gradient calculation. This requirement was addressed by forming a Rankine-Hugoniot enriched volumetric strain measure that is also derived from the Riemann solution. The volumetric strain measure is used in conjunction with the Rankine-Hugoniot pressure-volume relationship to obtain updated nodal pressures at each time step.

Accuracy of the nonlinear solids formulation was validated through several benchmark problems, where the numerical solutions were compared to experimental data or an analytical solution. The benchmark problems covered a broad range of shock conditions, ranging from weak elastic and elastic-plastic shocks to strong shocks due to hypervelocity impact. Across this spectrum, the formulation remained accurate and oscillation-free with maximum error of 6 percent, which is primarily attributed to variability in the experimental material properties. This is a significant improvement over the uncorrected solution, which showed oscillation error of over 30 percent and significant error in the shock pressure and wave speed for strong shocks.

The primary objective of constructing a meshfree RKPM hydrodynamic formulation, where the essential shock physics and oscillation control were addressed in a unified way, was achieved for both scalar conservation laws and the equation of nonlinear solids. This is a significant improvement in contrast to the artificial viscosity approach for modeling shocks in solids, that uses arbitrary numerical parameters and subjective length scales. Oscillation control in the present formulation stems from the definition of the Riemann problem initial conditions, so that the oscillation control mechanism is linked to the physics-based

enrichment of the formulation. With regard to implementation into a meshfree framework, because the shock-capturing enrichments are constructed on the SCNI topology the inclusion into a meshfree method is straightforward. Furthermore, the increase in computational cost is minimal, where it was found that computation time is increased approximately 15-20 percent; it is expected that this could be further reduced with more efficient coding structure.

Based on the accomplishments of this research, several areas are recommended as topics of future study for extension of these new meshfree shock modeling capabilities.

1. It was shown that accuracy in capturing the fine-scale shock structure is directly related to the accuracy of the Riemann problem initial conditions. In this work, it was shown how a limiter technique can be integrated into the meshfree framework to increase sharpness of the jump solution. Although the limiter technique was effective, the efficiency of this approach for an irregular, multi-dimensional meshfree discretization is not known. This issue should be investigated to determine how a limiter would be used in this situation. Alternatively, control of the RK approximation locality or continuity to achieve improved approximations of the Riemann problem initial conditions can also be studied.
2. A second issue that should be considered for further research is extension of the formulation to three-dimensional fragmentation problems. The key issue that must be addressed for this extension is translation of the technique from the SCNI framework to the SNNI. Under SNNI the integration cells are no longer conforming, which will require further investigation on how the Riemann problems

are formed and the enriched boundary solution is obtained. This extension will be key for strong dynamics applications, particularly for impact and shock in brittle materials such as concrete where spall and material fracture are common.

3. Finally, a third topic recommended for future study is application of the technique to fluid-structure interaction problems, such as a blast wave impacting a solid structure. The advantage that this formulation may provide for these types of problems is that the Rankine-Hugoniot problem solved on the integration cell boundary is in essence an interface problem. Otherwise stated, the Rankine-Hugoniot problem is already solved for the shock solution at the interface between two materials. Therefore, the contact surface of the blast wave on a structure could be considered as a material interface and the Rankine-Hugoniot problems should naturally capture the shock transmission due to the impedance mismatch. Application of the hydrodynamic formulation solely to blast waves in air may also be of interest, as the development of Lagrangian methods to model blast in air is of current interest to military research groups.

REFERENCES

[1] Y. Zhang, S. S. Babu, C. Prothe, M. Blakely, J. Kwasegroch, M. LaHa and G. Daehn, "Application of high velocity impact welding at varied length scales," *Journal of Material Processing Technology,* vol. 211, pp. 944-952, 2011.

[2] S. A. A. A. Mousavi and S. T. S. Al-Hassani, "Finite element simulation of explosively-driven plate impact with application to explosive welding," *Materials and Design,* vol. 29, pp. 1-19, 2008.

[3] B. J. Clark, D. P. Thambiratnam and N. J. Perera, "Enhancing the impact energy absorption in roll over protective structures," *International Journal of Crashworthiness,* vol. 13, no. 2, pp. 167-183, 2013.

[4] Z. Ahmad and D. P. Thambiratnam, "Application of foam-filled conical tubes in enhancing the crashworthiness performance of vehicle protectve structures," *International Journal of Crashworthiness,* vol. 14, no. 4, pp. 349-363, 2009.

[5] C. Tang, G. Cheng and Y. Chen, "Dislocation method study on rock damage induced by underground mine blasting," *Applied Mechanics and Materials,* pp. 2967-2970, 2013.

[6] P. Sharma, "Improved and accurate blasting techniques with modern precision drilling - key to achieve tehno-economics of high production underground metalliferous mines," *Journal of Mines, Metals and Fuels,* vol. 58, no. 8, pp. 232-236, 2010.

[7] X. Teng and T. Wierzbicki, "Gouging and fracture of engine containment structure under fragment impact," *Journal of Aerospace Engineering,* vol. 21, no. 3, pp. 174-186, 2008.

[8] C. F. Zhao, J. Y. Chen, Y. Wang and S. J. Lu, "Damage mechanism and response of reinforced concrete containment structure under internal blast loading," *Theoretical and Applied Fracture Mechanics,* vol. 61, pp. 12-20, 2012.

[9] High Velocity Impact Dynamics, New York: John Wiley and Sons, 1990.

[10] M. Grujicic, P. S. Glomski, T. He, G. Arakere, W. C. Bell and B. A. Cheesman, "Material modeling and ballistic-resistance analysis of armor-grade composites reinforced with high-performance fibers," *Journal of Materials Engineering and Performance,* vol. 18, no. 9, pp. 1169-1182, 2009.

[11] Z. H. Tan, X. Han, W. Zhang and S. H. Luo, "An investigation on failure mechanisms of ceramic/metal armour subjected to the impact of tungsten projectiles," *International Journal of Impact Engineering,* vol. 37, pp. 1162-1169, 2010.

[12] J. Ahmad, "A novel structure to protect against explosive loads," in *Proceedings of ASCE Structures Congress*, Vancouver, Canada, 2008.

[13] J. Weerheijm, J. Mediavilla and J. C. A. M. van Doormaal, "Explosive loading of multi-storey RC buildings: dynamic response and progressive collapse," *Structural Engineering and Mechanics,* vol. 32, no. 2, pp. 193-212, 2009.

[14] G. R. Johnson and R. A. Stryk, "Eroding interface and improved tetrahedral element algorithms for high velocity impact computations in three dimensions," *International Journal of Impact Engineering,* vol. 5, pp. 411-421, 1987.

[15] T. Belytschko and J. I. Lin, "A three-dimensional impact-penetration algorithm with erosion," *International Journal of Impact Engineering,* vol. 5, pp. 111-127, 1987.

[16] T. Belytschko and T. Black, "Elastic crack growth in finite elements with minimal remeshing," *International Journal for Numerical Methods in Engineering,* vol. 45, pp. 601-620, 1999.

[17] N. Moes, J. Dolbow and T. Belytschko, "A finite element method for crack growth without remeshing," *International Journal for Numerical Methods in Engineering,* vol. 46, pp. 131-150, 1999.

[18] A. W. Cook, M. S. Ulitsky and D. S. Miller, "Hyperviscosity for unstructure ALE

meshes," *International Journal of Computational Fluid Dynamics,* vol. 27, no. 1, pp. 32-50, 2013.

[19] J. Xin and J. E. Flaherty, "Viscous stabilization of discontinuous Galerkin solutions of hyperbolic conservation laws," *Applied Numerical Methods,* vol. 56, pp. 444-458, 2006.

[20] M. Bause and K. Schwegler, "Higher order finite element approximations of systems of convection-diffusion-reaction eqeuations with small diffusion," *Journal of Computational and Applied Mathematics,* vol. 246, pp. 52-64, 2013.

[21] T. E. Tezduyar, S. R. Krishnan and S. Sathe, "Stabilized formulations for incompressible flows with thermal coupling," *International Journal for Numerical Methods in Fluids,* vol. 57, pp. 1189-1209, 2008.

[22] L. Mingquin, W. L. Wei, I. Bin, X. J. Zhao and S. Li, "Numerical simulation of 2D bend-flows with WENO schemes," in *Proceedings of 2011 International Symposium on Water Resources and Environmental Protection*, Xi'an, China, 2011.

[23] T. S. Cheng and K. S. Lee, "Numerical simulatoins of under-expanded supersonic jet and free shear layer using WENO schemes," *International Journal of Heat and Fluid Flow,* vol. 26, pp. 755-770, 2005.

[24] W. K. Liu, S. Jun and Y. F. Zhang, "Reproducing kernel particle methods," *International Journal for Numerical Methods in Fluids,* vol. 20, pp. 1081-1106, 1995.

[25] J. S. Chen, C. Pan, C. T. Wu and W. K. Liu, "Reproducing kernel particle methods for large deformation analysis of nonlinear structures," *Computer Methods in Applied Mechanics and Engineering,* vol. 139, pp. 49-74, 1996.

[26] D. J. Benson, "Computational methods in Lagrangian and Eulerian hydrocodes," *Computer Methods in Applied Mechanics and Engineering,* vol. 99, pp. 235-394, 1992.

[27] J. S. Chen, C. T. Wu, S. Yoon and Y. You, "A stabilized conforming nodal integration for Galerkin meshfree methods," *International Journal for Numerical Methods in Engineering,* vol. 50, pp. 435-466, 2001.

[28] J. S. Chen, S. Yoon and C. T. Wu, "Non-linear version of stabilized conforming nodal integration for Galerkin mesh-free methods," *International Journal for Numerical Methods in Engineering,* vol. 53, pp. 2587-2615, 2002.

[29] R. A. Gingold and J. J. Monaghan, "Smooth particle hydrodynamics: theory and application to non-spherical stars," *Monthly Notices of the Royal Astronomical Society,* vol. 181, pp. 375-389, 1977.

[30] P. Lancaster and K. Salkauskas, "Surfaces generated by moving least squares

methods," *Mathematics of Computation,* vol. 37, pp. 141-158, 1981.

[31] B. Nayroles, G. Touzot and P. Villon, "Generalizing the finite element method: diffuse approximation and diffuse elements," *Computational Mechanics,* vol. 10, pp. 307-318, 1992.

[32] T. Belytschko, Y. Y. Lu and L. Gu, "Element-free Galerkin methods," *International Journal for Numerical Methods in Engineering,* vol. 37, pp. 229-256, 1994.

[33] J. S. Chen and H. P. Wang, "New boundary condition treatments for meshless computation of contact shock problems," *Computer Methods in Applied Mechanics and Engineering,* vol. 187, pp. 441-468, 2000.

[34] J. S. Chen, W. Hu, M. Puso, Y. Wu and X. Zhang, "Strain smoothing for stabilization and regularization of Galerkin meshfree methods," *Lecture Notes in Computational Science and Engineering,* vol. 57, pp. 57-76, 2006.

[35] P. C. Guan, S. W. Chi, J. S. Chen, T. R. Slawson and M. J. Roth, "Semi-Lagrangian reproducing kernel particle method for fragment-impact problems," *International Journal of Impact Engineering,* vol. 38, pp. 1033-1047, 2011.

[36] J. C. Tannehill, D. A. Anderson and R. H. Pletcher, Computational Fluid Mechanics and Heat Transfer, Philadelphia, PA: Taylor and Francis, 1997.

[37] P. D. Lax, Hyperbolic systems of conservation laws and the mathematicla theory of shock waves, Philadelphia, PA: Society for Industrial and Applied Mathematics, 1973.

[38] P. D. Lax and B. Wendroff, "Systems of conservation laws," *Communications on Pure and Applied Mathematics,* vol. 13, pp. 217-237, 1960.

[39] S. K. Godunov, "Finite difference method for numerical computation of discontinuous solutions of the equations of fluid dynamics," *Math. Sbornik, translated US Joint Publ. Rel. Services, JPRS 7226,* vol. 47, pp. 271-306, 1969.

[40] B. v. Leer, "Towards the ultimate conservative difference scheme, V: a second-order sequel to Godunov's method," *Journal of Computational Physics,* vol. 32, pp. 101-136, 1979.

[41] G. D. v. Aldaba, B. van Leer and W. W. Roberts, "A comparative study of computational methods in cosmic gas densities," *Astronomy and Astrophysics,* vol. 108, pp. 76-84, 1982.

[42] P. L. Roe, "Characteristic-based schemes for the Euler equations," *Annual Review of Fluid Mechanics,* vol. 18, p. 337, 1986.

[43] G. Strang, Computatial Science and Engineering, Wellesley, MA: Wellesley-Cambridge Press, 2007.

[44] A. Harten and S. Osher, "Uniformly high-order accurate nonoscillatory schemes, I," *SIAM Journal on Numerical Analysis,* vol. 24, no. 2, pp. 279-309, 1987.

[45] A. Harten, B. Engquist, S. Osher and S. R. Chakravarty, "Uniformly high order accurate essentially non-oscillatory schemes, III," *Journal of Computational Physics,* vol. 131, pp. 3-47, 1997.

[46] X. Liu, S. Osher and T. Chan, "Weighted essentially non-oscillatory schemes," *Journal of Computational Physics,* vol. 115, pp. 200-212, 1994.

[47] C. W. Shu and S. Osher, "Efficient implementation of essentially non-oscillatory shock-capturing schemes," *Journal of Computational Physics,* vol. 77, pp. 439-471, 1988.

[48] C. W. Shu and S. Osher, "Efficient implementation of essentially non-oscillatory shock-capturing schemes, II," *Journal of Computational Physics,* vol. 83, pp. 32-78, 1989.

[49] S. Osher and C. W. Shu, "Recent progress on essentially non-oscillatory shock capturing schemes," in *Lecture Notes in Engineering*, Springer-Verlag, 1989, pp. 316-333.

[50] A. N. Brooks and T. J. R. Hughes, "Streamline upwind/Petrov-Galerkin formulations

for convection dominated flows with particular emphasis on the incompressible Navier-Stokes equations," *Computer Methods in Applied Mechanics and Engineering,* vol. 32, pp. 99-259, 1982.

[51] T. J. R. Hughes and A. N. Brooks, "A theoretical framework for Petrov-Galerkin methods with discontinuous weighting functions: application to the streamline upwind procedure," in *Finite Elements in Fluids, Vol. IV*, London, Wiley, 1982, pp. 46-65.

[52] T. J. R. Hughes and A. Brooks, "A multidimensional upwind scheme with no crosswind diffusion," in *Finite Element Methods for Convection Dominated Flows*, New York, ASME, 1979.

[53] I. Christie, D. F. Griffiths, A. R. Mitchell and O. C. Zienkiewicz, "Finite element methods for second order differential equations with significant first derivatives," *International Journal for Numerical Methods in Engineering,* vol. 10, pp. 1389-1396, 1976.

[54] D. W. Kelly, S. Nakazawa, O. C. Zienkiewicz and J. C. Heinrich, "A note on upwinding and anisotropic balancing dissipation in finite element approximations to convective diffusion problems," *International Journal for Numerical Methods in Engineering,* vol. 15, pp. 1705-1711, 1980.

[55] T. J. R. Hughes and T. E. Tezduyar, "Finite element methods for first-order hyperbolic

systems with particular emphasis on the compressible Euler equations," *Computer Methods in Applied Mechanics and Engineering,* vol. 45, pp. 217-284, 1984.

[56] T. J. R. Hughes, M. Mallet and A. Mizukami, "A new finite element formulation for computational fluid dynamics: II. Beyond SUPG," *Computer Methods in Applied Mechanics and Engineering,* vol. 54, pp. 341-355, 1986.

[57] T. E. Tezduyar and M. Senga, "Stabilization and shock-capturing parameters in SUPG formulation of compressible flows," *Computer Methods in Applied Mechanics and Engineering,* vol. 195, pp. 1621-1632, 2006.

[58] T. E. Tezduyar and Y. J. Park, "Discontinuity-capturing finite element formulation for nonlinear convection-diffusion-reaction equations," *Computer Methods in Applied Mechanics and Engineering,* vol. 59, pp. 307-325, 1986.

[59] J. VonNeumann and R. D. Richtmyer, "A method for the numerical calculation of hydrodynamic shocks," *Journal of Applied Physics,* vol. 21, pp. 232-237, 1950.

[60] M. L. Wilkins, "Use of artificial viscosity in multidimensional fluid dynamics calculations," *Journal of Computational Physics,* vol. 36, pp. 281-303, 1980.

[61] R. D. Richtmyer and K. W. Morton, Difference methods for initial-value problems, New York: Interscience Publishers, 1967.

[62] R. Landshoff, "A numerical method for treating fluid flow in the presence of shocks," Los Alamos Scientific Laboratory Report LA-1930, 1955.

[63] W. F. Noh, "Numerical methods in hydrodynamic calculations," University of California, Lawrence Livermore National Laboratory, Report UCRL-52112, 1976.

[64] W. F. Noh, Methods in Computational Physics, Academic Press, 1964.

[65] J. O. Hallquist, "LS-DYNA Theory Manual," Livermore Software Technology Corporation, Livermore, CA, 2006.

[66] S. H. Lee, H. J. Kim and S. Jun, "Two scale meshfree method for the adaptivity of 3-D stress conentration problems," *Computational Mechanics,* vol. 26, pp. 376-387, 2000.

[67] H. Lu and J. S. Chen, "Adaptive Galerkin particle Method," *Lecture Notes on Computational Science and Engineering,* vol. 26, pp. 251-267, 2002.

[68] Y. You, J. S. Chen and H. Lu, "Filters, reproducing kernel, and adaptive meshfree method," *Computational Mechanics,* vol. 31, pp. 316-326, 2003.

[69] A. Angulo, L. P. Pozo and F. Perazzo, "A posteriori error estimator and an adaptive technique in meshless finite point methods," *Engineering Analysis with Boundary Elements,* vol. 33, pp. 1322-1338, 2009.

[70] G. R. Liu and Z. H. Tu, "An adaptive procedure based on background cells for meshless methods," *Computer Methods in Applied Mechanics and Engineering,* vol. 191, pp. 1923-1943, 2002.

[71] U. Haussler-Combe and C. Korn, "An adaptive approach with the Element-Free-Galerkin method," *Computer Methods in Applied Mechanics and Engineering,* vol. 162, pp. 203-222, 1998.

[72] S. Jun and S. Im, "Multiple-scale meshfree adaptivity for the simulation of adiabatic shear band formation," *Computational Mechanics,* vol. 25, pp. 257-266, 2000.

[73] J. S. Chen and W. Hu, "Reproducing kernel partition of unity: from continuum to quantum," in *Computational Mechanics: Proceedings of the 2007 International Symposium on Computational Mechanics*, 2007.

[74] G. Nianfei, L. Guangyao and L. Shuyao, "3D adaptive RKPM method for contact problems with elastic-plastic dynamic large deformation," *Engineering Analysis with Boundary Elements,* vol. 33, pp. 1211-1222, 2009.

[75] V. P. Nguyen, T. Rabczuk, T. Bordas and M. Duflot, "Meshless methods: A review and computer implementation aspects," *Mathematics and Computers in Simulation,* vol. 2008, pp. 763-813, 2008.

[76] O. C. Zienkiewicz and J. Z. Zhu, "A simple error estimator and adaptive procedure for practical engineering analysis," *International Journal for Numerical Methods in Engineering,* vol. 24, pp. 337-357, 1987.

[77] H. J. Chung and T. Belytschko, "An error estimate in the EFG method," *Computational Mechanics,* vol. 21, pp. 91-100, 1998.

[78] W. K. Liu, S. Jun, D. T. Sihling, Y. Chen and W. Hao, "Multiresolution reproducing kernel particle method for computational fluid dynamics," *International Journal for Numerical Methods in Fluids,* vol. 24, pp. 1391-1415, 1997.

[79] W. K. Liu, Y. Chen, C. T. Chang and T. Belytschko, "Advances in multiple scale kernel particle methods," *Computational Mechanics,* vol. 18, pp. 72-111, 1996.

[80] W. K. Liu, W. Hao, Y. Chen, S. Jun and J. Gosz, "Multiresolution reproducing kernel particle methods," *Computational Mechanics,* vol. 20, pp. 295-309, 1997.

[81] S. Li and W. K. Liu, "Moving least-square reproducing kernel method Part II: Fourier analysis," *Computer Methods in Applied Mechanics and Engineering,* vol. 139, pp. 159-153, 1996.

[82] W. K. Liu and Y. Chen, "Wavelet and multiple scale reproducing kernel methods," *International Journal for Numerical Methods in Fluids,* vol. 21, pp. 901-931, 1995.

[83] C. K. Lee and Y. Y. Shuai, "An automatic refinement procedure for the reproducing kernel particle method. Part I: Stress recovery and a posteriori error estimation," *Computational Mechanics,* vol. 40, pp. 399-413, 2007.

[84] C. K. Lee and Y. Y. Shuai, "An automatic refinement procedure for the reproducing kernel particle method. Part II: Adaptive refinement," *Computational Mechanics,* vol. 40, pp. 415-427, 2007.

[85] Z. Ma, H. Chen and C. Zhou, "A study on point moving adaptivity in gridless method," *Computer Methods in Applied Mechanics and Engineering,* vol. 197, pp. 1926-1937, 2008.

[86] L. Davison, Fundamentals of Shock Propagation in Solids, Berlin: Springer-Verlag, 2008.

[87] P. W. Cooper, Explosives Engineering, New York: Wiley-VCH, 1996.

[88] D. Grady, "Shock equation of state properties of concrete," in *Proceedings of the Fourth International Conference on Structures Under Shock and Impact*, Udine, Italy, 1996.

[89] C. A. Hall, L. C. Chhabildas and W. D. Reinhart, "Shock Hugoniot properties and release in concrete with different aggregate sizes from 3 to 23 GPa," *International*

Journal of Impact Engineering, vol. 23, pp. 341-351, 1999.

[90] L. Rohr, H. Nahme and K. Thoma, "Material characterization and constitutive modeling of ductile high strength steel for a wide range of strain rates," *International Journal of Impact Engineering,* vol. 31, pp. 401-433, 2005.

[91] M. D. Adley, A. O. Frank, K. T. Danielson, S. A. Akers and J. L. O'Daniel, "The Advanced Fundamental Concrete (AFC) Model, Technical Report ERDC/GSL TR-10-51," U.S. Army Engineer Research and Development Center, Vicksburg, MS, 2010.

[92] L. E. Schwer and L. J. Malvar, "Simplified concrete modeling with *MAT_CONCRETE DAMAGE_REL3," in *JRI LS-DYNA User Week*, 2005.

[93] T. J. Holmquist, G. R. Johnson and W. H. Cook, "A computational constitutive model for concrete subjected to large strains, high strain rates, and high pressures," in *14th International Symposium on Ballistics*, Quebec, Canada, 1993.

[94] N. Gebbeken, S. Greulich and A. Pietzsch, "Hugoniot properties for concrete determined by full-scale detonation experiments and flyer-plate impact tests," *International Journal of Impact Engineering,* vol. 32, pp. 2017-2031, 2006.

[95] K. Tsembelis and D. D. Radford, "The properties of concrete materials subjected to impact and shock loading," in *Transactions, SMiRT*, Toronto, 2007.

[96] H. P. Rossaminth and K. Uenishi, "The mechanics of spall fracture in rock and concrete," *Fragblast,* vol. 10, pp. 111-162, 2006.

[97] J. Weerheijm and J. C. A. M. Van Doormaal, "Tensile failure of concrete at high loading rates: New test data on strength and fracture energy from instrumented spalling tests," *International Journal of Impact Engineering,* vol. 34, pp. 609-626, 2007.

[98] W. D. Reinhart, L. C. Chhabildas, M. E. Kipp and L. T. Wilson, "Spall strength measurements of concrete for varying size aggregate size," in *Proceedings of 15th U.S. Army Symposium on Solid Mechanics*, Mytrle Beach, SC, 1999.

[99] M. Ohtsu, F. Uddin, W. Tong and K. Murakami, "Dynamics of spall failure in fiber reinforced concrete due to blasting," *Construction and Building Materials,* vol. 21, pp. 511-518, 2007.

[100] A. Jeffrey and T. Tanuiti, "Nonlinear wave propagation: Application to physics and magnetohydrodynamics," in *Mathematics in Science and Engineering*, New York, Academic Press, 1964.

[101] P. Lax, "Hyperbolic systems of conservation equations, II," *Communcations in Pure and Applied Mathematics,* vol. 10, pp. 537-566, 1957.

[102] O. Oleinik, "Discontinuous solutions of nonlinear differential equations," *Uspeki Mat.*

Nauk. (American Math. Soc. Translat. Ser. 2, 26, 95-172), vol. 12, pp. 3-73, 1957.

[103] R. J. Leveque, Numerical Methods for Conservation Laws, Birkhaueser, Basel, 1992.

[104] S. Osher and S. Chakravarthy, "High resolution schemes and the entropy condition," *SIAM Journal on Numerical Analysis,* vol. 21, no. 5, pp. 955-984, 1984.

[105] P. L. Roe, "The use of the Riemann problem in finite-difference schemes," *Lecture Notes in Physics,* vol. 141, pp. 354-359, 1980.

[106] P. L. Roe, "Approximate Riemann solvers, parameter vecors and difference schemes," *Journal of Computational Physics,* vol. 43, pp. 357-372, 1981.

[107] S. Osher, "Riemann solvers, the entropy condition and difference approximations," *SIAM Journal on Numerical Analysis,* vol. 21, no. 5, pp. 955-984, 1984.

[108] B. v. Leer, "On the relation between the upwind difference schemes of Godunov, Engquist-Osher, and Roe," *SIAM Journal on Scientific and Statistical Computing,* vol. 5, pp. 1-20, 1984.

[109] J. Chessa and T. Belytschko, "Arbitrary discontinuities in space-time finite elements by level sets and XFEM," *International Journal for Numerical Methods in Engineering,* vol. 61, pp. 2595-2614, 2004.

[110] A. Jeffrey and H. H. Dai, Handbook of Mathematical Formulas and Integrals, Academic Press, 2008.

[111] A. Harten, "High-resolution schemes for hyperbolic conservation laws," *Journal of Computational Physics,* vol. 50, pp. 235-269, 1983.

[112] A. Harten and J. Hyman, "Self-adjusting grid methods for one-dimensional hyperbolic conservation laws," *Journal of Computational Physics,* vol. 50, pp. 235-269, 1983.

[113] B. Engquist and S. Osher, "One-sided difference approximations for nonlinear conservation laws," *Mathematics of Computation,* vol. 36, pp. 321-352, 1981.

[114] J. S. Chen, C. Pan, C. Roque and H. Wang, "A Lagrangian reproducing kernel particle method for metal forming analysis," *Computational Mechanics,* vol. 22, pp. 289-307, 1998.

[115] J. S. Chen, Y. Wu, P. Guan, H. Teng, J. Gaidos, K. Hofstetter and M. Alsaleh, "A semi-Lagrangian reproducing kernel formulation for modeling earth moving operations," *Mechanics of Materials,* vol. 41, pp. 670-683, 2009.

[116] T. Rabczuk and T. Belytschko, "A three-dimensional large deformation meshfree method for arbitrary evolving cracks," *Computer Methods in Applied Mechanics and Engineering,* vol. 196, pp. 2777-2799, 2007.

[117] E. F. Toro, Riemann Solvers and Numerical Methods for Fluid Dynamics, 3rd ed., Berlin: Springer-Verlag, 2009.

[118] B. W. Levy, K. G. Powell and B. van Leer, "Use of a rotated Riemann solver for the two-dimensional Euler equations," *Journal of Computational Physics,* vol. 106, pp. 201-214, 1993.

[119] D. S. Chandrasekharaiah and L. Debnath, Continuum Mechanics, San Diego, CA: Academic Press, 1994.

[120] S. A. Marsh, "LASL Shock Hugoniot Data," University of California Press, Berkley, CA, 1980.

[121] J. K. Dukowicz, "A general, non-iterative Riemann solver for Godunov's method," *Journal of Computational Physics,* vol. 61, pp. 119-137, 1985.

[122] B. v. Leer, "Towards the ultimate conservative difference scheme IV. A new approach to numerical convection," *Journal of Computational Physics,* vol. 23, pp. 276-299, 1977.

[123] C. D. Lundergan and W. Herrmann, "Equation of state of 6061-T6 aluminum at low pressures," *Journal of Applied Physics,* vol. 34, no. 7, pp. 2046-2052, 1963.